

February 2021

Piezoelectrically-Transduced ZnO-on-Diamond Resonators with Enhanced Signal-to-Noise Ratio and Power-handling Capability for Sensing and Wireless Communication Applications

Xu Han

University of South Florida

Follow this and additional works at: <https://scholarcommons.usf.edu/etd>

 Part of the [Electrical and Computer Engineering Commons](#)

Scholar Commons Citation

Han, Xu, "Piezoelectrically-Transduced ZnO-on-Diamond Resonators with Enhanced Signal-to-Noise Ratio and Power-handling Capability for Sensing and Wireless Communication Applications" (2021). *Graduate Theses and Dissertations*.

<https://scholarcommons.usf.edu/etd/8784>

This Dissertation is brought to you for free and open access by the Graduate School at Scholar Commons. It has been accepted for inclusion in Graduate Theses and Dissertations by an authorized administrator of Scholar Commons. For more information, please contact scholarcommons@usf.edu.

Piezoelectrically-Transduced ZnO-on-Diamond Resonators with Enhanced Signal-to-Noise
Ratio and Power-handling Capability for Sensing and Wireless Communication Applications

by

Xu Han

A dissertation submitted in partial fulfillment
of the requirements for the degree of
Doctor of Philosophy
Department of Electrical Engineering
College of Engineering
University of South Florida

Major Professor: Jing Wang, Ph.D.
Arash Takshi, Ph.D.
Sylvia Thomas, Ph.D.
Rasim Guldiken, Ph.D.
Jiangfeng Zhou, Ph.D.

Date of Approval:
January 24, 2021

Keywords: Feedthrough, Microelectromechanical Systems, Notch, Finite Element Methods,
Microfabrication, Piezoelectric, Quality Factor, Tether, Phononic Crystal

Copyright © 2021, Xu Han

Dedication

To my wife & son, my parents, my advisors, my friends

Acknowledgments

First, I would like to express my sincerest gratitude to my advisor and my lifelong friend, Professor Dr. Jing Wang, for the priceless guidance me through my Ph.D. journey over the last six years. I want to say thank you to Dr. Jing Wang for unconditionally supporting me with academic knowledge, research instructions, professional career advice. I would also like to thank the rest of the professors on my dissertation committee: Dr. Sylvia Thomas, Dr. Arash Takshi, Dr. Rasim Guldiken, and Dr. Jiangfeng Zhou, for their questions and constructive recommendations for my research work. Meanwhile, I would like to thank the current and former members that I have worked with within the RF MEMS Transducers Group at the University of South Florida. Special thanks to my office mates and close friends: Dr. Di Lan, Dr. Adrian Avila, for the unlimited technical support. Also, to my peers Tinghung Liu, Adnan Zaman, and Abdulrahman Alsolami, it is a pleasure to work with all of you in the past years. It is an unforgettable memory that will be forever cherished.

I am also truly grateful to all the staff employees at Nanotechnology Research and Education Center (NREC) for meticulous care to the facility, training, and technical supports on all kinds of tools. My special appreciation goes to Richard Everly for numerous help and conversations, and Robert Tufts for the excellent management, and Sclafani Louis-Jeune for kindness and assistance.

Last but not least, I would like to state my genuine appreciation to my family. Countless thanks to my parents Xiangfang Ding and Wei Han, I would not have become what I am today

without your unconditional understanding and support. Most importantly, I would like to express my deepest gratitude to my wife, Ling Huang, and my son Ethan Han. It has been such a memorable journey during my Ph.D. years with joy and bitterness, and you are the reason that I always need to work harder. We have been running and walking through this marathon, and now we finally see the finish line, and we are all ready to step into the next chapter of our life and face challenges.

Table of Contents

List of Tables	iii
List of Figures	iv
Abstract	ix
Chapter 1: Introduction	1
1.1 Overview	1
1.2 Review of MEMS-based Sensor	2
1.3 Current State-of-the-art MEMS Acoustic Resonators	4
1.3.1 Surface Acoustic Wave Resonators	6
1.3.2 Bulk Acoustic Wave Resonators	8
1.3.3 Contour Mode Resonators	10
1.4 Drawbacks of the Current State-of-the-art Resonator Technologies and Issues	12
1.5 Dissertation Organization	13
1.6 Contributions	14
Chapter 2: Background of Piezoelectric Effect and Material Characterizations	16
2.1 Piezoelectric Effect	16
2.2 Mathematical Explanations of Piezoelectric Effect	17
2.3 Piezoelectric Material Selections	19
2.4 Zinc Oxide Characterizations	22
2.4.1 Gas Ratio (Ar:O ₂)	26
2.4.2 Influences of Process Temperatures and Post-annealings	27
2.4.3 Other Characterization Results	28
2.4.4 Conclusions of ZnO Characterizations	30
Chapter 3: Fundamental Parameters and Circuit Models of Piezoelectric Resonators	31
3.1 Fundamental Parameters of Resonators	31
3.1.1 Resonance Frequencies	31
3.1.2 The Electromechanical Coupling Coefficient, k^2	32
3.1.3 The Quality Factor, Q	33
3.1.4 Figure of Merit	34
3.2 Electrical Circuit Representation of a Piezoelectric MEMS Resonator	34
3.3 Butterworth-Van Dyke (BVD) Circuit Model	37
Chapter 4: Operation Modes and Finite Element Simulation Studies of Piezoelectrically-transduced Resonators	42

4.1 Operation Modes Studies of Piezoelectrically-transduced Resonators	42
4.2 Finite Element Method on Piezoelectrically-transduced Acoustic Resonators	47
4.2.1 3-D Model Setup for Piezoelectrically-transduced Acoustic Resonators	47
4.2.2 FEM Studies of Piezoelectric Thickness	48
4.2.3 FEM Studies of Crystalline Orientations of Piezoelectric Material	49
4.2.4 FEM Studies of Aperture Size	51
4.2.5 FEM Studies of Finger-to-gap Ratio.....	53
Chapter 5: Fabrication Process and Measurement Results	55
5.1 Fabrication Process of ZnO Piezoelectric Resonator on Silicon Wafers.....	56
5.2 Fabrication Process of ZnO Piezoelectric Resonator on Diamond-on-Silicon Wafers	58
5.3 Measurement Results Analysis of Different Design Configurations of Piezoelectrically-transduced ZnO Thin-film MEMS Acoustic Resonators.....	61
5.3.1 Aperture Size	61
5.3.2 Finger-to-gap Ratio (FGR) of Contour Mode Acoustic Resonators.....	64
5.3.3 Bottom Electrode Configurations	65
5.3.4 Design Techniques of Tethers	67
5.4 Design Techniques for Quality Factor Improvements and Measurement Results.....	70
5.4.1 Approach #1: Using Diamond Substrates.....	72
5.4.2 Approach #2: Phononic Crystal Tethers	73
5.4.3 Other Q Improvement Approaches	77
5.5 Temperature Linearity of Temperatures	78
5.6 Power-Handling Capability	82
Chapter 6: Signal-to-Noise Ratio Improvement and Portable Mass Sensing Unit.....	89
6.1 Notched Thin-Film Piezoelectric Interdigital Transducer for Enhanced Signal-to-Noise Ratio and Feedthrough Suppression	89
6.2 Feedthrough Noise Cancellation by Electrically Cascading Resonators	96
6.3 De-ionized Water Droplet Test and Portable Mass Sensing Unit.....	99
Chapter 7: Conclusions and Future Works	101
7.1 Conclusions.....	101
7.2 Future Works	104
References.....	107
Appendices.....	114
Appendix A: Copyright Permissions	115
Appendix B: Detailed Fabrication Process for Piezoelectric ZnO Resonators.....	120
Appendix C: XRD Omega-axis Rocking Curve Measurement Instructions	126
About the Author	End Page

List of Tables

Table 1.1 A Summary of State-of-the-art Mass Sensing Technologies.....	3
Table 2.1 Properties of the Most Commonly Used Piezoelectric Materials.....	21
Table 2.2 ZnO Characteristics under Different Sputtering Conditions with the Bulk Acoustic Configurations (FBAR)	29
Table 3.1 Mapping between Electrical and Mechanical Variable Used in Figure 3.2	35
Table 4.1 A Summary of Resonance Frequency Calculations for Different Vibration Modes	47
Table 5.1 A Comparison of Resonance Responses with Different Finger-to-gap Ratios	88

List of Figures

Figure 1.1 Structure of a traditional piezoelectric microcantilever and its typical application as bio-chemical sensors.....	2
Figure 1.2 (a) SEM micrograph of the stem self-aligned, radial-contour-mode disk resonator; (b) frequency characteristics for a 1.51 GHz, radial-contour mode, disk resonator measured in both vacuum and air.....	5
Figure 1.3 (a) Schematic view of a typical SAW resonator; (b) top-down view of metal electrodes	6
Figure 1.4 (a) Basic cross-section structure view of I.H.P.SAW; (b) calculated surface concentration ratio of SAW energy	8
Figure 1.5 Cross-sectional schematic views of the two types of bulk acoustic wave (BAW) resonators with two different types of acoustic isolation methods	9
Figure 1.6 Schematic illustration of a two-port contour mode resonator	11
Figure 2.1 Illustration of piezoelectric effect in a crystal lattice	16
Figure 2.2 Photograph of the PVD sputtering equipment: AJA Orion 5.....	23
Figure 2.3 Measured 2-theta ($2-\Theta$) XRD rocking curves of ZnO thin films of two different thicknesses showing drastically different (002) peak amplitude and consistent half maximum (FWHM) value	25
Figure 2.4 2-theta rocking curves for sampled deposited under varied gas ratios.....	26
Figure 2.5 Measured 2-theta rocking curves for samples deposited at room temperature and 300 °C before and after RTP annealing	28
Figure 3.1 A demonstration of frequency response and fundamental parameters of a resonator.....	31
Figure 3.2 (a) The spring-mass system of a resonator; (b) the equivalent electrical model of a piezoelectric resonator	35
Figure 3.3 Scheme of Butterworth-Van Dyke (BVD) circuit model.....	37

Figure 3.4 Estimated Butterworth-Van Dyke (BVD) circuit models at different frequency range.....	40
Figure 4.1 Vibration modes of piezoelectrically-transduced acoustic resonators: (a) longitudinal (“33” mode); (b) extensional (“31” mode); (c) thickness-transversal (“31” shear mode); and (d) lateral-shear (“15” mode)	42
Figure 4.2 Longitudinal mode rectangular plate resonator	43
Figure 4.3 A microscope-view of a piezoelectrically-transduced disk resonator	45
Figure 4.4 FEM nodal analysis using COMSOL Multiphysics® of a circular membrane vibrating in the first four contour modes	45
Figure 4.5 Multiple-order of displacements of Lamb wave modes from FEM nodal analysis using COMSOL Multiphysics	46
Figure 4.6 (a) The microscope image of a ZnO thin-film piezoelectric rectangular resonator that has a body dimension of 320 μm x 80 μm , 5 IDT fingers, a finger pitch size of 16 μm ; (b) 3-D meshed model for FEM simulation of the fabricated resonator design in (a)	48
Figure 4.7 The FEM simulated frequency responses of the resonators as a parametric study of the piezoelectric material's thickness (ToPZ) ranging from 0.2 μm to 0.8 μm	49
Figure 4.8 The FEM simulated frequency responses of the resonator’s crystal orientation of the piezoelectric layer (ToPZ) ranging from 0 degree (c-axis aligned perpendicular to the surface) to 40 degrees	51
Figure 4.9 The FEM simulated frequency responses of the resonators with aperture size (AP) ranging from 100 μm to 400 μm	52
Figure 4.10a The FEM simulated frequency responses of the resonators with different finger-to-gap ratios.....	53
Figure 4.10b The FEM simulated frequency responses of the resonators, which have the same pitch size of 16 μm along with the distance in between IDT electrode fingers (Gf) ranging from 6 μm to 10 μm	54
Figure 5.1 Simplified four-mask fabrication process flow of ZnO thin-film piezoelectric MEMS acoustic resonators	57
Figure 5.2 Four-masks fabrication process of ZnO piezoelectric resonator on diamond-on-silicon wafers.....	60

Figure 5.3 A comparison of the frequency response of the two resonators which are identically designed except for the aperture size	62
Figure 5.4 A comparison of the frequency response of the two resonators which are identically designed except for the aperture size	63
Figure 5.5 A comparison of the frequency response of four resonators based on a silicon wafer	65
Figure 5.6 Equivalent static capacitances in the BVD circuit models for the two-port contour-mode resonators under different bottom electrodes conditions: (a) grounded-bottom electrodes; (b) floating bottom electrodes.....	66
Figure 5.7 The measured frequency response of the two-port contour-mode resonators with different bottom electrode configurations: (a) grounded bottom electrodes (labeled in red); (b) floating bottom electrodes (labeled in blue); (c) grounded IDT bottom electrodes (labeled in green).....	67
Figure 5.8 The measured frequency responses of the two-port contour-mode resonators with the tether width of 10 μm (labeled in blue), 7 μm (labeled in red), and 5 μm (labeled in green).....	68
Figure 5.9 The measured frequency responses of the two-port contour-mode resonators with the tether length of 7 μm (labeled in green), 5 μm (labeled in blue), and 3 μm (labeled in red).....	68
Figure 5.10 The measured frequency responses of the two-port contour-mode resonators with different number of tethers: 2 tethers (labeled in green), 6 tethers (labeled in blue), and 10 tethers (labeled in red).....	69
Figure 5.11 (a) A cross-sectional-view SEM photograph of a ZnO thin-film piezoelectric disk resonator on a diamond-coated silicon wafer; (b) a zoom-in view of the resonator structural body layers.....	72
Figure 5.12 (a) A photograph of the ZnO thin-film piezoelectric disk resonators with different radius; (b) a comparison of frequency responses of the piezoelectric disk resonators on different substrates (blue: on a diamond-coated wafer; red: on a silicon wafer)	73
Figure 5.13 (a) A mask view example of a ZnO thin-film piezoelectric contour-mode resonators with 4 cross-shaped phononic crystals on the tethers; (b) a comparison of the frequency response of the resonators with different numbers of cross-shaped phononic crystals on the tethers.....	74

Figure 5.14 The zoomed-in views of the frequency response at two peaks circled in Figure 5.13 (b).....	75
Figure 5.15 (a) A mask view example of a ZnO thin-film piezoelectric contour-mode resonators with 4 diamond-shaped phononic crystals on the tethers; (b) a comparison of the frequency responses of the resonators with different numbers of diamond-shaped phononic crystals on the tethers	75
Figure 5.16 (a) A mask view example of a ZnO thin-film piezoelectric contour-mode resonators with 4 triangle-shaped phononic crystals on the tethers; (b) A mask view example of a ZnO thin-film piezoelectric contour-mode resonators with four triangle-shaped phononic crystals on the tethers pointing in the opposite direction; (c) a comparison of frequency responses of the resonators with different numbers of triangle-shaped phononic crystals on the tethers	76
Figure 5.17 A comparison of the frequency response of the resonators with six phononic crystals in different shapes on the tethers (labeled in purple, blue, and red), against the original tether (labeled in green)	77
Figure 5.18 Temperature compensation techniques used in piezoelectric acoustic resonators: (a) thin film overlay; (b) thermal expansion constraint	80
Figure 5.19 (a) Measured frequency response of the resonator built on a silicon wafer over a temperature range from 20 to 100°C; (b) measured resonance frequencies over temperature.	81
Figure 5.20 (a) Measured frequency response of the resonator built on a diamond-coated wafer over a temperature range from 20 to 100°C; (b) measured resonance frequencies over temperature	82
Figure 5.21 The two-port DUT device test scheme is strategically designed to enable the de-embedding process	85
Figure 5.22 The comparisons of the measured frequency responses between the small-signal inputs and the high-power large signal inputs with proposed de-embedding data process: (a) the resonator’s frequency responses on a silicon wafer; (b) the resonator’s frequency response on a diamond-coat silicon wafer	86
Figure 5.23 The comparisons of the two-port frequency responses wafer under high-power input of a silicon device: (a) the measured results without the de-embedding data processing; (b) the measured results with the de-embedding data processing.	87

Figure 5.24 The comparisons of the two-port frequency responses wafer under high-power input of a device on a diamond-coated wafer: (a) the measured results without the de-embedding data processing; (a) the measured results with the de-embedding data processing	87
Figure 6.1 The FEM results depict the change of feedthrough noise levels due to the partial substitution of the ZnO piezoelectric transducer layer by air notches in between the IDT electrodes	91
Figure 6.2 The change of electrical fields and displacement pattern due to the partial substitution of the ZnO piezoelectric transducer layer by air notches in between the IDT electrodes	92
Figure 6.3 Measured frequency response of an $80\mu\text{m} \times 320\mu\text{m}$ MEMS resonator with two tethers (green) and the same resonator with etched notches/air cavities between each adjacent IDT electrode (red) as well as the equivalent circuit models that have been taken into account of both the feedthrough (noise) and the motional current (signal).....	93
Figure 6.4 A zoom-in view of the circled area in Figure 6.13: the measured frequency responses of the first width-extension mode within a narrower frequency span with and without the notched air cavity features for the same resonator design	94
Figure 6.5 The frequency response with/without the etched notches of the resonator with 10 tethers	95
Figure 6.6 The mask views of the cascaded two-port rectangular resonator(s): (a) $\times 1$; (b) $\times 2$; (3) $\times 3$	97
Figure 6.7 A comparison of the measured frequency responses between the single two-port resonator (green curve) and the cascading resonators ($\times 2$, red curve; $\times 3$, blue curve)	97
Figure 6.8 A comparison of the measured frequency responses between the single two-port resonator (green curve) and the cascading resonators ($\times 2$, red curve; $\times 3$, blue curve)	99
Figure 6.9 A comparison of the measured frequency responses of the two-port piezoelectric MEMS resonator during the droplet testing	100

Abstract

Microelectromechanical system (MEMS) resonators emerged a few decades ago, and now they have been well developed and commercially utilized as a core part in many radio frequency (RF) communication hardware as well as micro-sensing and detections for many different latest applications. Since MEMS-based devices are made small thanks to the microfabrication technology's improvement, the cost can be drastically reduced when mass-produced on wafer batches, and the devices still maintain a decent performance with negligible power consumption. This perfectly fits into the requirements of the newest internet-of-thing (IoT) and headset applications. Our previous research mainly focuses on designing and fabricating MEMS resonators based on piezoelectric thin film while lacking systemic study and understanding the acoustic behavior in design variants. This research addresses the mentioned concern and further improves many resonators' performance, such as higher quality factors, lower static capacitance, and higher power handling. In the meantime, diamond technology has been reviewed and adopted in this research, delivering high-performance MEMS acoustic resonators fabricated on Diamond-on-Silicon (DOS) wafers. The measured unloaded quality factor is as high as 7,370 near 200 MHz, which can be an excellent candidate for sensing and detection purposes. It is the first time thicker macrocrystalline diamond films (10-20 μm) are implemented into MEMS acoustic resonators design and fabrications. Meanwhile, tether (also known as anchor) designs have been thoroughly studied, including various dimensions and quantities. Different-shaped phononic crystals have been exploited to improve the resonators' quality factors and suppress spurious mode at lower frequencies.

An innovative post-process technique has been introduced, aiming to create notched air gaps in between interdigital transducer (IDT) electrodes of a MEMS resonator. By substituting lossy Zinc Oxide (ZnO) by air, the static capacitance can be reduced, leading to a lower feedthrough noise level by 10 dB or more while having less impact on insertion loss. By using this strategy, the signal-to-noise ratio (SNR) at the resonance can be enhanced, which is favorable for sensing and detection capabilities. The capacitance ratio is defined as the ratio of static capacitance over the motional capacitance. Due to a smaller static capacitance, the capacitance ratio is lower, resulting in a higher electromechanical coupling coefficient. In the meantime, it is observed several spurious modes can be effectively suppressed or fully eliminated due to the modified distribution of electric field and displacement/strain field in the piezoelectric transducer layer adjacent to IDT electrodes thanks to the newly introduced air notches. The mentioned post-fabrication technique adds another degree of freedom in vertical coordinate in MEMS resonators design variants. Moreover, the SNRs can be further improved by cascading multiple contour-mode resonators so that the static capacitance can be canceled. Last but not least, a droplet test has been conducted to sense different levels of mass. To make the testing unit portable, a 3-D printed evaluation board has been carried out to avoid the need for probing.

Chapter 1: Introduction

1.1 Overview

Micro-electrical-mechanical systems (MEMS) electronic devices, benefited from the rapidly developed micromachining technologies, have been studied and massively commercialized in the last recent decades. For instance, MEMS resonators, as the fundamental elements of filters and oscillators, are commonly replacing the traditional bulky off-chip quartz resonators for the fact they are delivering a decently competitive performance, but with a much smaller size and lower cost per unit. Radio frequency micro-electro-mechanical systems (RF MEMS), benefited from rapid-growing micromachining technologies, have been massively studied and successfully commercialized in recent decades.

With its rapid development, RF MEMS technology is now becoming a viable solution to batch-produce high-performance RF passive components, such as tunable filters, switches, capacitors, varactor, inductors, and high-quality factor (Q) resonators for the next generation of wireless communication systems. Although MEMS devices offer multiple unique advantages, there are still some technical difficulties to dig into. For example, its power handling issue can be a significant concern in the next-generation 5G wireless communication systems because of its high complexity and multi-duty at higher frequency bands. Also, it is anticipated that the parasitic effects at higher frequencies could significantly impact future transceivers. In addition to the wireless applications, it is also widely convinced that MEMS resonators are substantially capable of various sensing platforms and purposes. The main reason is that MEMS resonators exhibit

incredibly high sensitivity due to their miniaturized volume and mass by several orders compared to the traditional quartz crystal counterparts. Also, its small size and negligible power consumption make MEMS technology perfectly suitable for implantable bio-chemical sensing [1][3][4], gas identifications [2], wearable IoT applications. Nowadays, there are plenty of commercially available MEMS-resonator-based sensing and detection systems that have been successfully deployed across a range of industries with a wide variety of applications, including medical diagnosis and monitoring [3][4], food science [5], and oil analysis [6].

1.2 Review of MEMS-based Sensor

One of the commonly sensing and detecting methodologies is achieved by measuring the signal change due to a weight change when the transducer's equilibrium state is altered. The raw data can often be a frequency shift, for instance, and by post-processed with read-out circuits and other electronics, which are often integrated with CMOS, then the captured data can be analyzed and interpreted using analytical techniques. The MEMS portion can be a bimorph cantilever, as shown in figure 1 below.

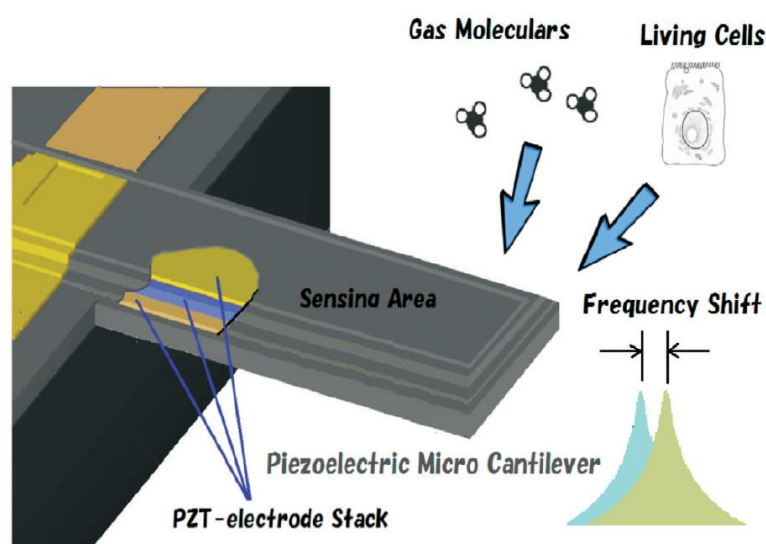


Figure 1.1 Structure of a traditional piezoelectric microcantilever and its typical application as bio-chemical sensors. Courtesy of Lu et al. [4]. See permissions in Appendix A.

The limitations of MEMS cantilever do appear to be significant when the high resonance frequencies and mass resolutions are demanded for specific applications. In fact, more types of resonators can be deployed for sensing and detection. Here the table below demonstrates a summary of different resonator mechanisms in comparisons of frequency, sensitivity, and resolution. As to sensors' performance, the sensitivity is usually referred to as the constant proportionality between output and input for a linear transducer, whereas the resolution is defined as the smallest quantity of change that can be captured.

Table 1.1 A Summary of State-of-the-art Mass Sensing Technologies [7]-[13].

Device	Resonant Frequency (MHz)	Localized Mass Sensitivity (kHz pg ⁻¹)	Mass Resolution (fg)
QCM [7,8]	5		100
FBAR [9]	~2300		9
SAW [10]	200	0.0009	3000
MEMS Microcantilever [11]	~0.350	0.878	
NEMS Nanocantilever [12]	13	5100	0.039
Capacitive Disk [13]	132	31.5	0.130

Although MEMS-resonator-based sensors exhibit outstanding performance under many scenarios, they also face difficulties in resolution and sensitivity in the specific testing environment. For example, it is more challenging to maintain the quality factor and signal-to-noise ratio (SNR) needed for a particular limited of detection when the MEMS devices have to be operated in a humid or liquid environment, as compared to operation under ambient conditions [14][15]. That is because the insertion loss and damping loss are significant increased in the liquid. To address this issue, the most straightforward way is simply to make MEMS resonators with sufficiently high

quality factors and SNR so that the damping loss can still be compensated in the liquid environment. In the later chapters, a number of innovative design techniques will be discussed to improve quality factors and signal-to-noise ratios of piezoelectric MEMS resonators.

1.3 Current State-of-the-art MEMS Acoustic Resonators

Benefited from the rapid development of micromachining technologies, micromachined acoustic resonators and acoustic Radio Frequency (RF) filters have been successfully studied and massively commercialize with the explosive growth of “smart” cellular devices, which are widely able to support 4G or Long Term Evolution (LTE), or nowadays 5G communications that aim to handle faster data rates with the ability to serve more users in an extremely crowded spectrum are deemed critical. In the wireless communication system, timing and filtering, relying on oscillators and RF/IF filters are the most essential elements that determine the overall performance of today’s highly integrated wireless RF front-end receiver systems. Because of micromachined resonators featuring higher bandwidth, much smaller size, and lower cost, micro-acoustic filters and oscillators are gradually replacing the bulk off-chip quartz resonators and became one of the key enabling devices of modern RF and microwave electronics spanning many different industry fields.

Speaking of micro-resonators, there are two main categories dividing them into piezoelectric resonators and capacitive resonators, based on the transduction mechanisms or types of waves launched. Figure 1.5 demonstrates an example of capacitively transduced MEMS resonators studied by Wang et al. [16] back in 2004. The particular presented radial-contour mode MEMS disk resonator features resonant frequencies up to 1.51 GHz supported by the uniquely developed self-aligned fabrication technique [16]. This frequency was the first time a MEMS resonator is reported in the gigahertz regime back then. In the meantime, the reported quality factors are also exaptational high, with Q’s of 11,555 in vacuum and 10,100 in the air [16]. Other

consecutive work exploited extension vibrated wine-glass mode disk resonator operating at 74 MHz extremely high Qs of 98,000 in vacuum and 8,600 in the air [17].

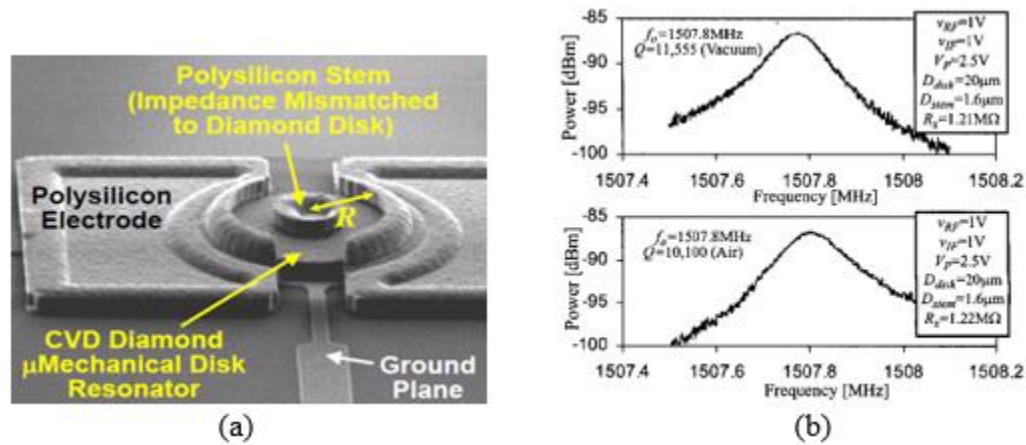


Figure 1.2 (a) SEM micrograph of the stem self-aligned, radial-contour-mode disk resonator; (b) frequency characteristics for a 1.51 GHz, radial-contour mode, disk resonator measured in both vacuum and air. Courtesy of Wang et al. [16] [17]. See permissions in Appendix A.

Unlike the capacitive resonators' needing external larger drive voltage, piezoelectric resonators can generate different acoustic waves simply by having opposite electrical potentials at different locations of electrodes that contact the piezoelectric material. Recently researches show that piezoelectric micro-resonators can now achieve high quality factors almost on par with the best of the capacitive counterparts while, in the meantime, offering a much greater electromechanical coupling coefficient (k_t^2). Meanwhile, capacitive resonators are prone to experience very high insertion loss (>80 dB) and large motional impedance (> 1 M Ω) [16][17], which also make them nearly impossible to be used in RF communication electronics, which mostly match to 50-ohm system. In this dissertation, all the work and results are concentrated on thin-film piezoelectric MEMS acoustic resonators.

It is worthy to clarify that the current-state-of-art micro-acoustic technology has not been equal to MEMS acoustic technology yet due to the overall electronics' size still in the millimeter

range. For example, commercial RF filters or duplexers are still in a dimension of several millimeters. However, their fabrications are heavily dependent on the generosity of micromachining technology.

1.3.1 Surface Acoustic Wave Resonators

Surface acoustic wave resonators are generally operated by launching acoustic waves propagating on the surface of a material with the piezoelectric effect, converting energy back and forth between the electrical and mechanical realms. To fully understand the piezoelectric effect, more discussion will be served in the later chapters. Nowadays, most commercialized SAW micro-resonators utilize lithium niobite (LiNbO_3) or lithium tantalite (LiTaO_3) as the functional layer where the piezoelectric effect occurs.

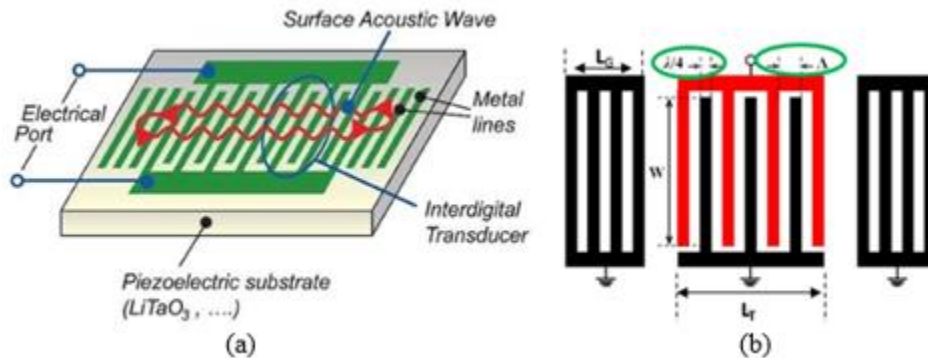


Figure 1.3 (a) Schematic view of a typical SAW resonator; (b) top-down view of metal electrodes.

As demonstrated in Figure 1.3, by sinusoidally varying the voltage, interdigital transducer (IDT) metal electrodes are used to launch or receive acoustic waves on the surface of the piezoelectric substrate. The generated surface acoustic waves are reflected by employing grating fingers at both sides of IDTs to confine the energy leakage. The resonant frequency of a one-port SAW resonator is determined by the ratio of the acoustic velocity of the generated wave over the distance between the center of adjacent interdigit transducers, which is usually referred to as the pitch size. These pitch sizes are commonly designed near to $\frac{1}{2}$ wavelength of the generated

acoustic wave. There are other quantities also specified in wavelengths, such as aperture (W), transducer length (L_T), and grating length (L_G). These design parameters can broadly define the insertion loss and sharpness of the resonance peak. As seen in the above figure, it is evident that SAW resonators' fabrication and potential mask steps can be relatively simplified because they theoretically only require one pattern IDT layers on the existing piezoelectric substrate layer.

SAW technology delivers a decent performance in RF filtering applications within the past decades. A vast majority of research surrounding surface acoustic waves has been done in the 19th and 20th centuries. Since then, SAW technology has played a significant role in the RF filtering market until bulk acoustic wave (BAW) technology is revealed and taken from high-performance filtering applications. Even now, SAW resonators and filters are still clearly the first choice for many companies in low-band RF applications because of the solid performance at a lower cost.

The biggest drawback of SAW resonators is their lack of ability to achieve higher frequencies above 2.5 GHz while still maintaining good quality factors. This is intrinsically limited by slow the acoustic velocity merely on the surface, and the loss mechanism becomes dominated and more challenging to control when operation frequencies are higher. Another constraint for SAW to high-frequency ranges is that the designed resonance frequency can only be done by reducing the electrode width and height, which are heavily committed to the lithography equipment capability. The use of a more sophisticated lithography system such as ArF one (laser wavelength: 193 nm) enables much narrower electrodes. However, narrower and thinner electrodes result in a significant increase in the ohmic resistance, which causes substantial performance deterioration [18]. Most recent years, there is another breakthrough technology called “incredible high-performance SAW” (I.H.P SAW) developed and reported by Murata Inc. [19], which truly excels in the 3-5 GHz range for SAWs. Such technology incorporates a new multi-

layered structure (LiNbO_3 or LiTaO_3 / SiO_2 / AlN / Si) substrate, as shown in Figure 1.3(a), which aims to significantly improve the energy confinement capability at higher frequencies by creating acoustic mismatch at vicinities of different layers. In this way, undesired propagation loss can be effectively reduced, and therefore the quality factor can be drastically improved. As seen in Figure 1.3 (b), the measured quality factors show 6000 at 0.9 GHz to 1900 at 3.5 GHz, which are over three times higher than those of conventional 42YX-LT SAW resonators [19].

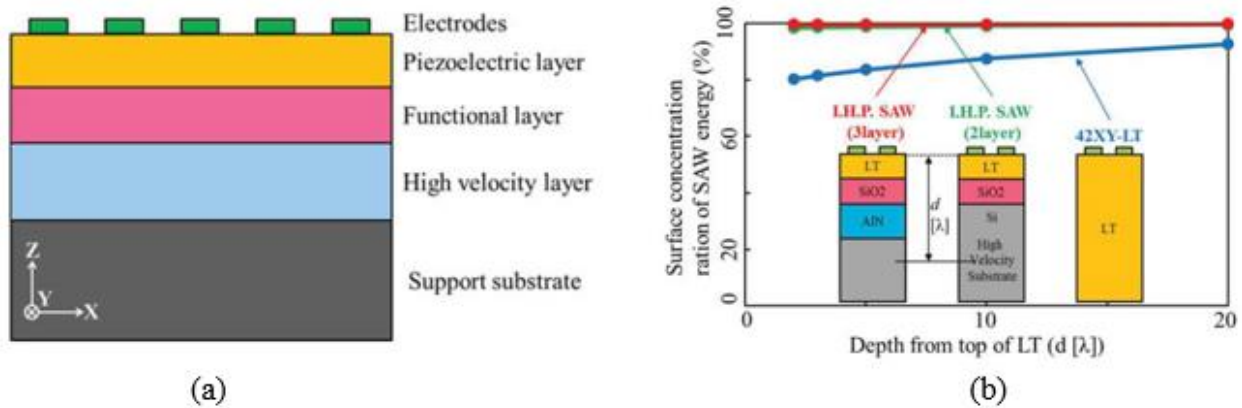


Figure 1.4 (a) Basic cross-section structure view of I.H.P.SAW; (b) calculated surface concentration ratio of SAW energy. Courtesy of Takai et al. [19]. See permission in Appendix A.

Despite the fact that this newly innovated I.H.P SAW address persisting problems that conventional SAW experience, considering the extremely complex bonding procedures and the high cost if massively produced, it would be hardly viable high-frequency applications in the RF filter market.

1.3.2 Bulk Acoustic Wave Resonators

Bulk acoustic wave (BAW) resonators employ acoustic waves propagating through the whole bulk of a certain material. The most typical mode utilized is the thickness-shear mode. Unlike SAW's need for very fine patterned inter-digital transducer electrodes, a basic thin-film BAW resonator can be built by simply having a piezoelectric thin film sandwiched by two metal electrodes. These two electrodes on the top and bottom of the piezoelectric layer generate and

detect acoustic waves as a differential electrical potential applied. The resonance frequency is primarily determined by the thickness of the piezoelectric layer and the selection of the electrode's material.

In today's market, film bulk acoustic resonator (FBAR) and solidly mounted resonator (SMR) are the two main proven BAW device configurations adopted widely. The key difference is the technologies to confine the acoustic energy. Figure 1.4 (a) and (b) illustrated the cross-sectional schematic views of FBAR and SMR, respectively. It is known that acoustic waves can barely travel through the air because the acoustic velocity of air is nearly zero. FBARs take advantage of the truth by creating air cavities underneath the bottom electrode, so acoustic energy can be very efficiently reflected at the electrode/air interface at both sides of the piezoelectric layer due to acoustic mismatches, therefore forming a high-Q resonator.

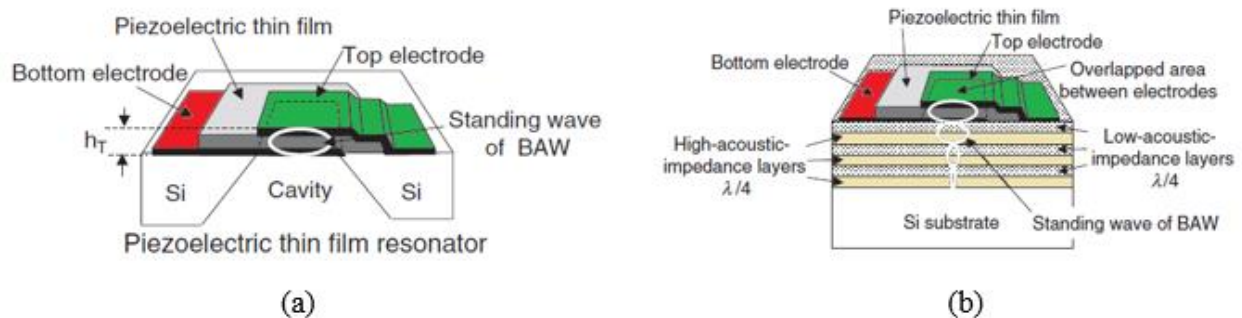


Figure 1.5 Cross-sectional schematic views of the two types of bulk acoustic wave (BAW) resonators with two different types of acoustic isolation methods. (a) Film bulk acoustic resonator (FBAR) sits on top of the air cavity; (b) solidly mounted resonator (SMR) employs Bragg's reflector.

Similar to FBAR, SMR also benefits from the acoustic mismatch to trap acoustic energy inside the device layers. Instead of the air cavity architecture underneath the bottom electrodes, SMR exploits a Bragg reflector stack composed of multi-layered materials with high/low acoustic impedance at about quarter-wavelength thick, as seen in Figure 1.4 (b). With this approach,

acoustic energy down-toward can be adequately reflected at the boundary of each pair of high/low-impedance Bragg reflectors.

Compared to SAW, BAW technology does not require advanced lithography equipment to support its high-frequency range applications. The operation frequencies can be controlled by adjusting the piezoelectric material's thickness. The thinner the piezoelectric layer, the higher frequencies are. That is why BAW is the favorable choice for high-frequency high-performance RF filtering applications. Furthermore, BAW technology also has other advantages over SAW, including better power-handling capability, insertion loss, and temperature performance. Although BAW has superior performance over SAW at high frequencies, a large amount of trimmings work is necessary to achieve the right frequency and k_t^2 from the piezoelectric layer done via chemical-mechanical-polishing (CMP). Hence, BAW is far more complicated as to the mask steps or fabrication complexity.

To face the new challenges in the next-generation 5G era, so far, BAW technology should be the best candidate unless other revolutionary improvements are made. For example, new piezoelectric material, new acoustic modes should be further investigated and researched.

1.3.3 Contour Mode Resonators

Contour mode resonator (CMR), also known as Lamb wave resonator (LWR), is a newly emerging class of piezoelectric resonators brought by Piazza et al. back in 2006 [20]. The typical acoustic waves associating such type of resonator are usually referred to as lamb wave, which can be simply understood as a type of surface acoustic wave that also has x- (lateral) and z-direction (vertical) displacement in that the propagating substrate is so thin, such as thin-film ZnO or thin-film AlN.

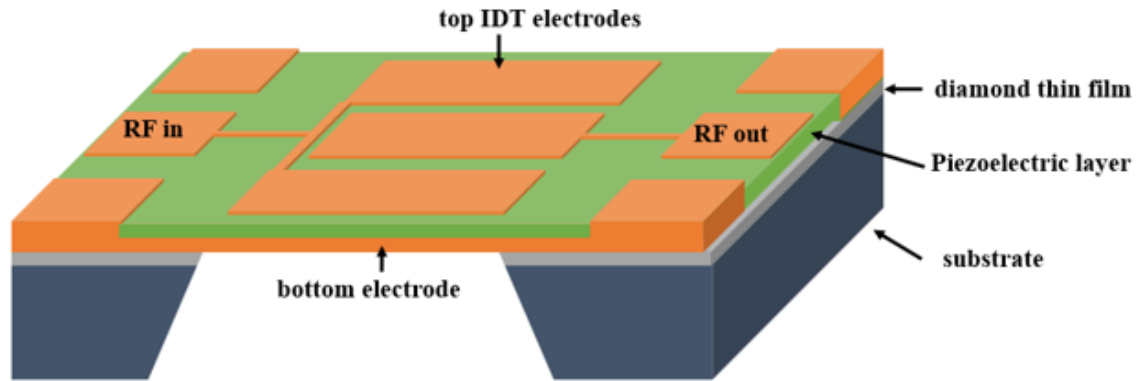


Figure 1.6 Schematic illustration of a two-port contour mode resonator.

As to the geometry, as demonstrated in Figure 1.5, conventional CMRs can be seen as a combination of SAW and BAW resonators, consisting of IDT metal electrodes on the top of the piezoelectric thin film, which sits on the bottom electrodes. Unlike SAW resonators' needing a quite number of gratings to reflect acoustic energy, the resonator body is suspended in the air and well defined in x- and y- directions through dry etching. Therefore, the CMRs are surrounded in all directions by air, which is a natural reflector.

The resonance frequency is usually determined by the lateral dimensions defined by lithography that is similar to SAW, rather than the thickness of the piezoelectric transducer layer, but the acoustic velocity of generated lamb wave can be a lot faster than the surface Raleigh waves and achievable operation frequency can be higher than a conventional SAW resonator. In addition to that, CMRs can not only enable multi-frequency outputs based on the inter-digit-transducer (IDT) with strategically designed pitch size in a fashion like SAW devices but also able to achieve higher frequencies up to 10 GHz by miniaturization of the suspended resonator body similar to an FBAR device [20]. This makes it also an excellent candidate for tunable RF electronics, which may be the next-generation mobile commination integrations trend.

1.4 Drawbacks of the Current State-of-the-art Resonator Technologies and Issues

As mentioned earlier, the MEMS resonators based on capacitive transductions have been thoroughly studied. This type of resonator can generally feature extremely high Qs and achievable operation frequencies, thus still making them stand out in frequency-Q product regards. However, the complexity of fabrications and extremely high insertion loss are the main issues that keep the capacitively-transduced MEMS resonators off the list of potential applications because their motional impedances are too high to be implemented into a 50-ohm system. SAW and BAW are the two successfully commercialized micro-acoustic technologies in today's RF filtering applications. Each of them has pros and cons. The main issues existing in SAW resonators are their struggle to perform once the operation frequencies go above 2.5 GHz, recalling that the resonance frequency depends on the thickness and photolithographic variations in IDT and grating metal.

Additionally, SAW resonators' quality factors are typically between 300 to 500, which can cause problems reflected in slow roll-off rate and worse insertion loss at the edges of passbands. Also, because of the IDT electrode arrangement, SAW resonators are more sensitive to the rise of operating power and temperature if no compensation techniques are applied. BAW technology is now considered a high-performance solution that addresses many concerns that SAWs have, but yet to be perfect. As discussed earlier, the resonance frequency of a BAW resonator is dependent on the thickness of the piezoelectric layer and metal electrodes. If the layers are reduced, a higher-frequency resonator is always possible, but there is a threshold when the piezoelectric thin film is too to provide enough attributes. Also, because the piezoelectric thin films are formed by sputtering depositions, it is more challenging to attain as good k_t^2 as SAWs may get from the

single-crystal piezoelectric substrates. Hence, the achievable bandwidth is usually less than for BAW.

Previous research on CMR primarily concentrated on round-shaped resonators within the own group, utilizing wine-glass mode and radial-contour mode. While the insertion loss of such type is typically above 40 dB, and the capacitive feedthrough levels are close to the ambient noise floor. As to the rectangular-shaped CMR, we have adopted macrocrystalline diamond thin film underneath the bottom electrodes to enhance Q's performance aspects, temperature linearity, but in lack of systematic study in a few other concerns, such as k_t^2 , power handling, capacitive feedthrough control.

1.5 Dissertation Organization

This dissertation is organized into six chapters. The first chapter summarizes the current-state-of-the-art micro-acoustic resonator technologies and their applications, followed by the drawbacks and limitations of the previous research. This dissertation's motivation is to address those concerns and improve performance through different design and fabrication techniques.

Chapter 2 starts with the fundamentals of piezoelectricity as the background for material characterization. Zinc Oxide (ZnO) is chosen as the piezoelectric material to be studied and to be used as the piezoelectric layer for the presented MEMS resonators. Material characterization results are concluded to compare different sputtering conditions. In Chapter 3, fundamental parameters of MEMS resonators and their equivalent models are discussed, which were in specific investigated using Butterworth-Van Dyke (BVD) circuit models. Chapter 4 present the sources of design variations from the Finite Element Method (FEM) simulations. Chapter 5 reviews the detailed fabrication processes for piezoelectrically-transduced ZnO MEMS contour-mode resonators, which are built on four-inch Silicon wafers and diamond-coated Silicon wafers,

respectfully. Measurement results are presented, and a series of comparisons are discussed in terms of various performance parameters, such as Q, temperature dependency, power handling, and so forth. Chapter 6 discusses different approaches to improve the SNR ratio, followed by the droplet test. Finally, Chapter 7 concludes the insights and achievements of this work while also listing the viable directions for potential research to carry on.

1.6 Contributions

This dissertation work embraces a successful demonstration of a systematic study of piezoelectrically-transduced ZnO-on-diamond MEMS resonators. By employing the diamond thin film as the primary structural material of released resonators, the proposed MEMS resonators' power-handling capability will be dramatically improved with potentially top-notch performance. In addition to that, characterizations of sputtered ZnO piezoelectric thin film transducer have been conducted using different combinations of sputtering conditions, such as O₂ to Ar gas ratios, operation temperature as well as the impacts of post-annealing. Metrology analysis has been done to find the optimized deposition recipe to improve electromechanical coupling coefficient and dielectric properties.

To predict design variations, FEM simulations have been done to explore a parametric study on a number of design parameters, such as IDT finger-to-gap, aperture, and so forth. Later, resonators are designed, fabricated, and measured to successfully validated the simulation results' trends. A variation of phonon crystal structures on tethers has included in this work, with changes in quantity and shapes in the triangle, cross, and diamond geometry, serving as band gaps to suppress spurious modes. To further improve quality factors, many design techniques have been exploited. For example, different resonators' structural body shapes have been examined to increase Qs further.

An innovative design strategy has been discussed by introducing etched air cavities in the piezoelectric thin film between each pair of the IDT electrode fingers for lowering the capacitive feedthrough level while improving the signal-to-noise (SNR) by 3-5 dB. The parasitic capacitance calculation will be completed to fully support the extraction of the simulated capacitance results from FEM analysis. The cascading resonators can further boost SNR by canceling the static capacitance. To implement the fabricated device into sensing applications, a water droplet test has been performed and showed a promising outcome for the proposed sensing applications in a humid environment.

Chapter 2: Background of Piezoelectric Effect and Material Characterizations

2.1 Piezoelectric Effect

The piezoelectric effect was first discovered by French physicists Pierre and Jacques Curie in 1880, describing an interchange phenomenon between mechanical and electrical energy. The piezoelectric material is generally in crystalline in nature, with a regularly repeating lattice of unit cells. They can be found in a generic form of crystals such as quartz or synthetic ceramic via chemical vapor deposition (CVD), such as aluminum nitride (AlN) or Lithium Niobate (LiNbO₃). A simple illustration of the piezoelectric effect can be explained in Figure 2.1.

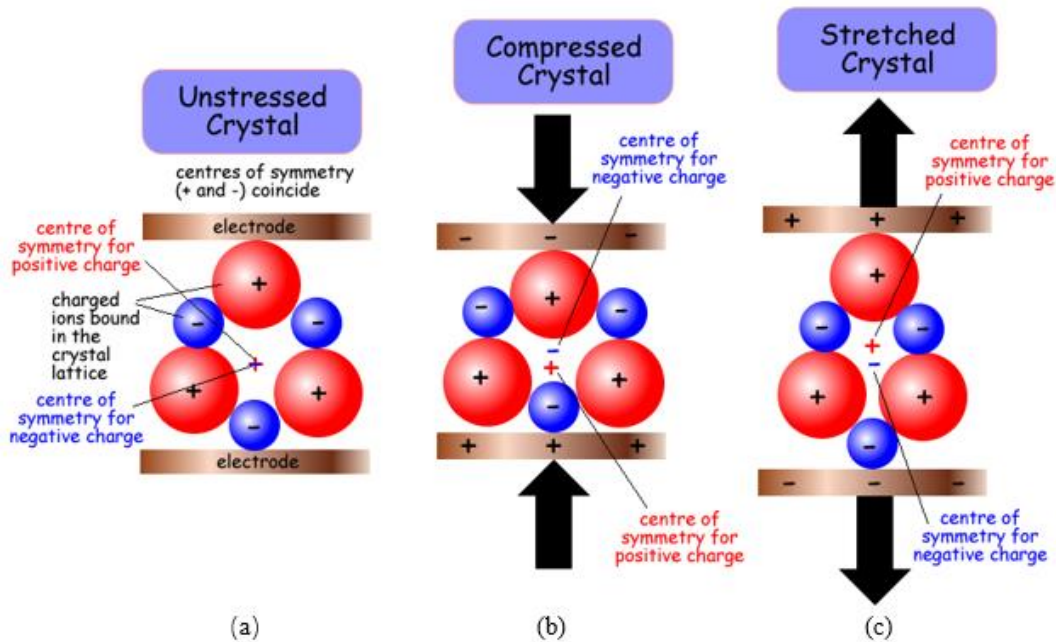


Figure 2.1 Illustration of piezoelectric effect in a crystal lattice. (a) Centers of symmetry of both positive and negative ions coincide in an unstressed crystal with balanced net charge; (b) in a compressed crystal, the centers of symmetry of charges move apart, leading to a rise to the net charge on the electrodes; (c) in a stretched crystal, the centers of symmetry of charges move apart, leading to a surge to net charge and polarized electrodes.

As shown in Figure 2.1 (a), when no external mechanical force is applied to a crystal lattice, a molecule with three negative ions and three positive ions is electrically neutral. The center of symmetry of both of the two ions coincide [21]. No electric charge effect is generated in this unstressed state, resulting in no electrical potential difference across the top and bottom side of electrodes. However, in Figure 2.1 (b) and (c), when mechanically deformed along particular axes due to an external force, the unit cells become polarized as the centers of symmetry of the charges move apart. At this compressed or stretched state, unit cells' net charges are no longer balanced, and an electrical potential can be found across the two electrodes.

Conversely, the application of an electric field along specific orientations can also cause the lattice to deform in response. Relating the piezoelectric effect to acoustic technology, if an alternating voltage is applied to the piezoelectric material, certain mechanical vibrations (acoustic waves) can be formed based on the applied voltage frequency. The resonance occurs when such a piezoelectric response reaches its maximum when the alternating voltage frequency matches the natural frequency of vibration of the material.

2.2 Mathematical Explanations of Piezoelectric Effect

As discussed in the last section, when a piezoelectric material is mechanically compressed or stretched, it becomes electrically polarized, producing a fixed electric charge on the material's surface. If electrodes are attached to the material's surfaces, the generated electric charge can be collected and used [22]. The mathematical presentation of the piezoelectric effect is based on the linear theory of piezoelectricity, with the equations of linear elasticity are coupled to the charge equation of electrostatics through the piezoelectric constants of the material [23], which are vector quantities, just like other anisotropic physical properties (e.g., permittivity, elasticity, and piezoelectric constant) are tensor quantities. The following equations that describe the

piezoelectric effect presented by the interaction between electrical and mechanical domain where mechanical stress (T), mechanical strain (S), an electrical field I , and electrical displacement (D) are given as:

$$S_p = s_{pq}^E T_q + d_{pk} E_k \quad (2.1)$$

$$D_i = d_{iq} T_q + \varepsilon_{ik}^T E_k \quad (2.2)$$

where S_p is the mechanical strain in the p direction, s_{pq}^E is elastic compliance under constant electric field, T_q is mechanical stress in the q direction, d_{kp} is piezoelectric constant, E_k is the electric field in the k direction, ε_{ik}^T is dielectric constant tensor under constant stress, and D_i is electric displacement in the I direction. The two subscript index defines the axis of the electrical excitation the mechanical actuation orientation, respectively. It is observed the amount of charge generated is directly proportional to the amount of external mechanical stress applied onto the piezoelectric material.

Four more alternate forms are listed below for a more detailed explanation to extend the piezoelectric effect concept in terms of stress, charge, and voltage.

The stress-charge form is expressed as:

$$T_{6 \times 1} = c_{6 \times 6}^E \cdot S_{6 \times 1} + e_{6 \times 3} \cdot E_{3 \times 1} \quad (2.3)$$

$$D_{3 \times 1} = e_{3 \times 6} \cdot S_{6 \times 1} + \varepsilon_{3 \times 3}^S \cdot E_{3 \times 1}$$

The strain-charge form is expressed as:

$$S_{6 \times 1} = s_{6 \times 6}^E \cdot T_{6 \times 1} + d_{6 \times 3} \cdot E_{3 \times 1} \quad (2.4)$$

$$D_{3 \times 1} = d_{3 \times 6} \cdot T_{6 \times 1} + \varepsilon_{3 \times 3}^T \cdot E_{3 \times 1}$$

The strain-voltage form is expressed as:

$$S_{6 \times 1} = s_{6 \times 6}^D \cdot T_{6 \times 1} + g_{6 \times 3} \cdot D_{3 \times 1} \quad (2.5)$$

$$E_{3 \times 1} = -g_{3 \times 6} \cdot T_{6 \times 1} + \beta_{3 \times 3}^T \cdot D_{3 \times 1}$$

The stress-voltage form is expressed as:

$$T_{6 \times 1} = c_{6 \times 6}^D \cdot S_{6 \times 1} - h_{6 \times 3} \cdot D_{3 \times 1} \quad (2.6)$$

$$E_{3 \times 1} = -h_{3 \times 6} \cdot S_{6 \times 1} - \beta_{3 \times 3}^S \cdot D_{3 \times 1}$$

where c is the stiffness matrix and e is the piezoelectric constant matrix. B is the inverse matrix of permittivity, and d , g , and h are the alternate forms of piezoelectric constants.

Another fundamental property of piezoelectric material frequently mentioned in MEMS technology is called electromechanical couple coefficient k_t^2 , defined as the ability of a material to interconvert electrical and mechanical energy [23], expressed as:

$$k_t^2 = \frac{\text{Converted Energy}}{\text{Input Energy}} \quad (2.7)$$

It is noted that both the converted energy and the input energy in the above equation can be mechanical or electrical. A higher k_t^2 stands for a more substantial piezoelectric effect. From an engineering perspective, the electromechanical coupling coefficient is one of the most critical parameters. A lot of characterization work has been invested in getting a higher k_t^2 by means of optimizing production conditions. In RF filtering applications, k_t^2 is proportional to the achievable bandwidth of filters, and a resonator's k_t^2 can be directly measured by looking into the series and parallel resonance. A more detailed explanation is covered in the later chapters.

2.3 Piezoelectric Material Selections

As mentioned in the previous sections, piezoelectric material can be generally categorized into piezoelectric crystals (piezo-crystals) and piezoelectric ceramics (piezo-ceramics). Piezo-crystals are the material in which the piezoelectric effect naturally occur, such as quartz, topaz, or even cane sugar. While in the most recent year, a few polymers have been studied and developed as a new emerging piezoelectric material that exhibits non-toxic and biocompatible properties that traditional piezo-ceramics do not hold. Typical examples of polymers are Polyvinylidene Fluoride

(PVDF) and Polyvinylidene Chloride (PVDC). These polymers are exceptional for bio-electronics, but their piezoelectric effect is too low to be used in many other applications.

Among these piezo-crystals, quartz is the most well-known and the first piezoelectric material used in various electronic devices. For example, in the past half-century, quartz crystal has widely cooperated in the microwave and RF oscillator and filter applications due to its excellent mechanical robustness, superbly high frequency-Q product, chemical stability, and low thermal coefficient expansion. However, by today's standard in RF mobile electronics, quartz crystal no longer has the advantages mainly because of its bulky size and small electromechanical couple coefficients, which tremendously limits the bandwidth. Compared to quartz, LiNbO_3 and LiTaO_3 also important piezo-crystals providing a much stronger piezoelectric effect and tunability of orientation cuts. Today, these two piezo-crystals are primarily commercialized in SAW filters and duplexers and extensively used for optical purposes.

Piezo-ceramics are now the mainstream piezoelectric material widely used in RF acoustic electronics and many MEMS applications. Typical examples of piezo-ceramics are aluminum nitride (AlN), zinc oxide (ZnO), barium titanate (BaTiO_3), and lead-zirconate-titanate (PZT). Among these piezo-ceramics, both BaTiO_3 and PZT exhibit excellent piezoelectric strain coefficients (d_{31} or d_{33}), which are one order of magnitude higher than those of AlN and ZnO. However, they also have their core weaknesses. For example, the thermal expansion coefficient of BaTiO_3 is so high that it makes its supported devices very unstable to the temperature change. Similarly, the high dielectric loss at high frequencies and the incompatibility to CMOS technologies limit the use of PZT to low-frequency MEMS device applications such as MEMS microphones, micro-piezo printer heads.

The remaining two piezo-ceramics: AlN and ZnO, offer well-balanced attributes satisfying electronics designers and researchers, such as CMOS compatibility, sufficient piezoelectric, and RF performance. More importantly, AlN and ZnO thin films can be deposited and characterized supported by the sputtering technology. If comparing AlN and ZnO, AlN has a few advantages over the other. For instance, its acoustic velocity and temperature coefficient of frequency is much better than that of ZnO. Meanwhile, AlN's deposition process makes it more favorable since its operating temperature is lower and does not contain contaminating elements such as zinc, which can be harmful to other semiconductor devices. Table 2.1 summarizes the properties of these materials mentioned above.

Table 2.1 Properties of the Most Commonly Used Piezoelectric Materials [24-29].

Material Properties	Symbol	Unit	AlN	PZT	ZnO
Elastic Modulus	E	Gpa	330	53	123
Density	ρ	kg /m ³	3260	7600	5676
Acoustic Velocity	v	m/s	10400	3300	4655
Poisson Ratio	σ		0.24	0.25-0.31	0.18-0.36
Piezoelectric Strain Coefficient	d_{31}	pC /N	-2	-123	-5
Piezoelectric Strain Coefficient	d_{33}	pC /N	5	289	12.4
Piezoelectric Strain Coefficient	d_{15}	pC /N	3.6	495	-8.3
Relative Permittivity	ϵ_r		8-10	400-1900	9-11
Thermal Expansion (300K)	α_t	10 ⁻⁶ /°C	4.15	2	2.92
Thermal Conductivity	k	W/mk	280	1.9	60
TCF	τ_f	ppm/°C	-25	NA	-60

As compared to ZnO, AlN holds a higher Young's modulus, a higher acoustic velocity, a higher thermal conductivity, and a low temperature coefficient of frequency (TCF), which made AlN a highly attractive piezoelectric transducer material. AlN films have been deposited with appropriate coupling coefficients, but it was not until the late 1990s that high-volume production-worthy AlN deposition techniques started to be offered by foundries, mostly thanks to the emerging film bulk acoustic wave (FBAR) technologies.

2.4 Zinc Oxide Characterizations

Although the physical vapor deposition process has been brought into the world over a century ago, the term "physical vapor deposition (PVD)" actually was first mentioned and engineered in the 1960s. At that time, the evolution of vacuum coating processes started to flourish, carrying out through the development of well-known technologies, such as sputtering, vacuum, plasma technology, magnetic fields, gas chemistry, thermal evaporation, bows, and power sources control [31]. PVD is one of the thin-film deposition process techniques that can coat the target material on a substrate atom by atom. The deposition rate varies from material to material, with the thin-film thicknesses as thin as some atomic layers to films with several microns. The property of the deposited material can be primarily affected by the setup of the process and the substrate's conditions. Sputtering is the most critical PVD process that the deposition process is made in a vacuum, gaseous, plasma, or electrolytic environment.

As mentioned in the previous sections, despite AlN is the trending piezoelectric material that has many advantages over others in MEMS acoustic applications, thin-film ZnO is chosen to be the piezoelectric layer for the MEMS resonators in this dissertation because of the other facility limitations such as Deep Reactive Ion Etch tools not supporting chlorine gas system, which is

required for AlN dry etch. Moreover, AlN's lithography may sometimes cause problems as AlN becomes vulnerable to some tetramethylammonium-hydroxide-based developers.

The thin-film deposition techniques of ZnO have been investigated and developed since the 1970s, with a wide variety of approaches not limited to RF or DC sputtering [30][31], ion plating, and chemical vapor deposition (CVD) [32][33]. So far, sputtering is a physical vapor deposition (PVD) method for depositing thin films with piezoelectric properties. So far, three sputtering techniques are commonly used in the industry, such as foundries, including RF diode sputtering, RF magnetron sputtering, and pulsed DC magnetron sputtering [34]. In this dissertation, ZnO thin films are processed through RF magnetron sputter using AJA Orion 5 sputtering tool in Figure 2.2.



Figure 2.2 Photograph of the PVD sputtering equipment: AJA Orion 5.

The optimization of the RF sputtered c-axis-aligned ZnO piezoelectric thin film was investigated with an improved transverse piezoelectric coefficient (d_{31}) that is deemed to be critical, especially in terms of the insertion loss and motional impedance, for the presented contour-

mode piezoelectric resonators because the mechanical vibrations employ in-plane displacements through an orthogonally applied electric field in the piezoelectric thin-film layer.

To ensure a low-level of gaseous contamination in the sputtering process, the base pressure of the vacuum chamber has to be kept at a lower level as possible. For the ZnO deposition process specifically, the base pressure is opted to maintain around the middle range 10^{-7} torr. Also, target pre-conditioning is required to make sure purity. The preliminary results indicate a strong correlation between improved c-axis oriented crystalline properties and the RF magnetron sputtering process conditions, including roughness and composition of the seed layer underneath, deposition/annealing temperature, single gun versus dual gun sputtering process, and so forth.

ZnO piezoelectric thin film can be characterized via a nondestructive and quantitative approach by leveraging the XRD rocking curves, which reveal broadening of the diffraction peaks. By this technique, multiple spots over an entire wafer with deposited ZnO film can be measured to study the properties such as the coupling coefficient and spatial variation (uniformity). For this, typically, full wave-half maximum (FWHM) values are used. Three factors that can cause an increment of the FWHM of a rocking curve are strains, including limited layer thickness and mosaicity (misorientation of crystallites). The degree of crystal orientation alignment plays a dominant role. Highly oriented ZnO thin film with (002) orientation shows a strong correlation with the FWHM of its x-ray diffraction scan rendered as its rocking curve. As ZnO film thickness increases, the XRD rocking curve's width reduces, and its (002) peak increases, thus leading to a lower rocking curve FWHM value for thicker ZnO films. It was found in the preliminary results that the rocking curve FWHM width of the (002) peak gets smaller from run to run, and the intensity of the (002) peak gets more substantial, which indicates the ZnO c-axis orientation improves with thickness.

Figure 2.3 presents the XRD 2-theta rocking curve spectra for ZnO thin films deposited at USF by RF magnetron sputtering on silicon wafers with a thickness of 80 nm (blue) and 250nm (red), respectively. Both samples were deposited under an ambient of 50% O₂ and 50% Ar with a substrate temperature of 300 °C and RF power of 80W. These samples were also annealed by rapid thermal processing (RTP) at 600 °C for 10 minutes. As the ZnO thin film gets thicker, the (0 0 2) becomes noticeably more potent. Although the XRD (002) peak intensity gets stronger, the full width at half maximum (FWHM) value was not significantly impacted by the thickness increment.

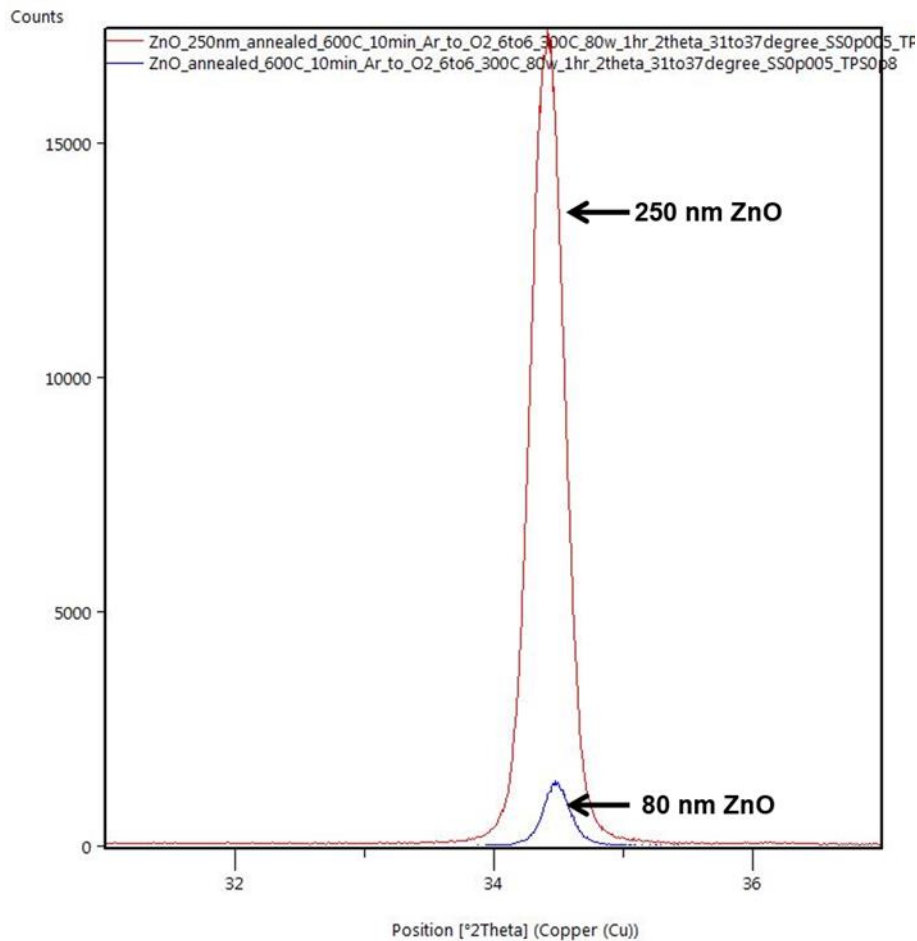


Figure 2.3 Measured 2-theta ($2-\Theta$) XRD rocking curves of ZnO thin films of two different thicknesses showing drastically different (002) peak amplitude and consistent half maximum (FWHM) value.

2.4.1 Gas Ratio (Ar:O₂)

During the perform PVD sputtering process, Argon and oxygen were the two gases involved. Theoretically, only Argon is needed for the ZnO deposition since the ZnO target was used for non-reactive sputtering. However, researchers report that it is beneficial to add oxygen gas to promote the material property by compensating for the potential depletion of oxygen elements. This is referred to as an “oxygen-rich” environment. When the ionized gases hit the ZnO target, the zinc and oxygen atoms are dissociated from the target and recombined on the sample substrate. Still, there is the situation that irregular combo when a zinc atom fails to combine with an oxygen atom to form ZnO layer, leaving an excessive amount of Zinc atom grown on the substrate. As a result, the dielectric properties and the piezoelectric effect may be abnormal.

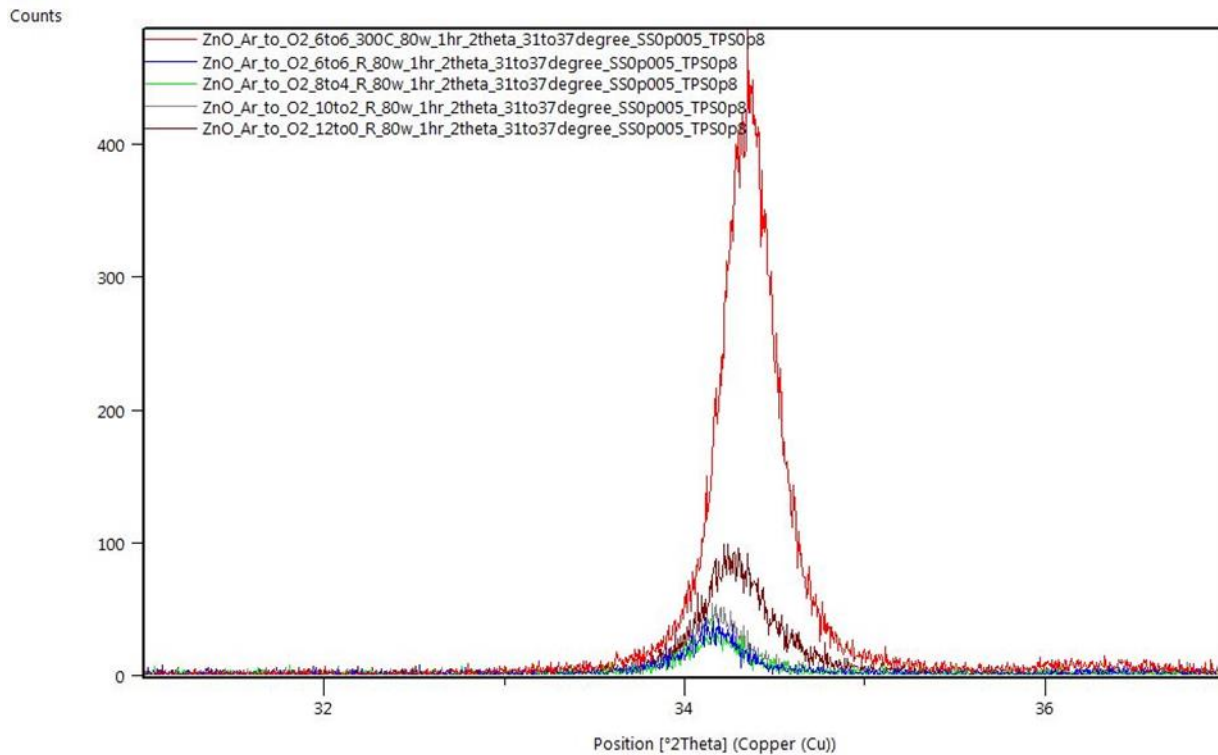


Figure 2.4 2-theta rocking curves for sampled deposited under varied gas ratios. One specimen is prepared at 300 °C while all the rest samples were deposited at room temperature.

As seen in Figure 2.4 above, XRD spectra measurements have been performed for ZnO thin films deposited on silicon wafers under a gradually varied O₂ percentage. The O₂ and Ar gas ratio were adjusted while the rocking curves for samples deposited under 50% (blue), 33% (green), 16.7% (grey), and 0% (brown) O₂ gas ratio in an O₂ and Ar gas environment were evaluated. For consistency, most of the ZnO thin film samples were deposited at room temperature by the RF magnetron sputtering for 1 hour at 80W, except for the one specimen (red) prepared at 300 °C. As the O₂ percentage decreases, there is a significant change in (0 0 2) peak intensity, as shown by the 2-theta rocking curves in Fig. 6. In particular, the (0 0 2) peak intensities are almost the same for the 50% (blue) and 33% (green) specimens. At 16.7% O₂ gas ratio, the (0 0 2) peak intensity exhibits a relatively small improvement, while the (0 0 2) peak intensity improves a lot as compared to that of the 0% O₂ sample. When the O₂ to Ar gas ratio decreases, the sputtering rate increases, and the thickness of the ZnO thin film directly impacts the (0 0 2) peak intensity. For comparison, two ZnO samples were deposited with the 50% O₂ to Ar gas ratio, one at room temperature (blue) and another at 300°C (red). In this case, the (0 0 2) peak intensity improves significantly as an indicator of better-aligned c-axis columnar grains and slight thickness increment.

2.4.2 Influences of Process Temperatures and Post-annealings

Figure 2.5 shows the XRD 2-theta rocking curves for ZnO samples sputter deposited on silicon wafers before and after annealed by RTP at 600 °C for 10 minutes deposited under different process (substrate) temperatures. All four samples were deposited with a 50% O₂-to-Ar gas ratio for 1 hour at 80W of RF power. The thin film samples can be separated into two groups. In the first group, two ZnO films were both deposited with a process temperature of 300 °C (red and green), one before RTP (green) and another after RTP (red). The intensity of (0 0 2) peak increases

due to the RTP annealing. Two samples were prepared in the second group with the substrate kept at room temperature, one before RTP (grey) and another after RTP (blue). The RTP annealed samples (red and blue) show significant improvement, which can be ascribed to releasing residual stress and improved crystal orientation alignment between the deposited columnar grains.

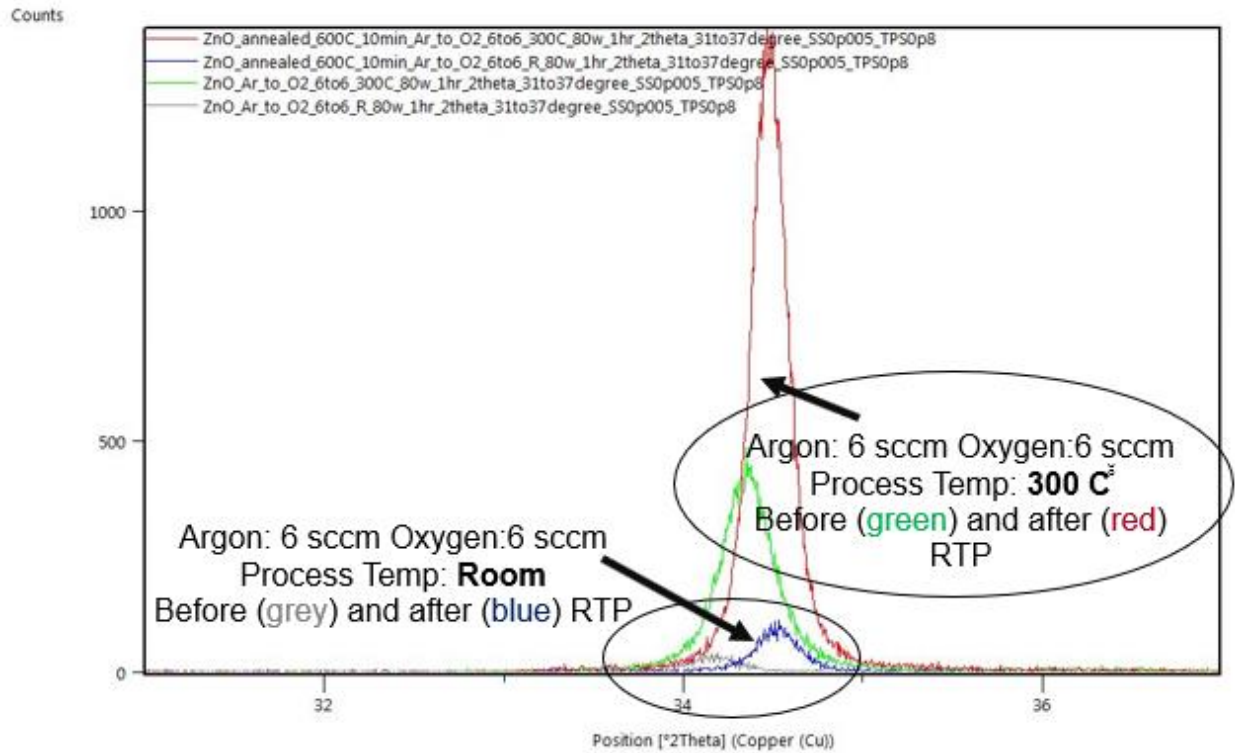


Figure 2.5 Measured 2-theta rocking curves for samples deposited at room temperature and 300 °C before and after RTP annealing.

2.4.3 Other Characterization Results

The previous characterization approaches using the XRD to indirectly predict the crystalline orientations of the sputtered ZnO thin films. However, there is still no straight evidence on how the different process conditions influence piezoelectric performance, evaluated by reading the k^2t . To address this concern, in this section, ZnO thin films are RF sputter deposited on the bottom electrodes using a different gas ratio to investigate the impacts of the process conditions on the electromechanical coupling coefficient (k^2t), sheet resistance, and deposition rate. In order

to measure the k^2t , ZnO thin film samples are pattern in a sandwich-like configuration (bottom electrode/ZnO/top electrode) to realize the simplest film bulk acoustic resonator (FBAR) device. Then the frequency response of the thickness mode for each sample is measured by a network analyzer to calculate kt^2 with a previously written program based on a reference datasheet of FBAR. Meanwhile, the sheet resistances are measured with a four-point probe, and the deposition rates are optically calculated with an ellipsometry tool from Filmetrics.

Table 2.2 ZnO Characteristics under Different Sputtering Conditions with the Bulk Acoustic Configurations (FBAR).

Bottom Electrode	ZnO Thickness	Sputter Condition	Top Electrode	k^2t	Deposition Rate (nm/hr)	Sheet Resistance (Ω /sq)
30nm Cr + 500nm Pt	500 nm ZnO	80W 300C Ar:12 O ₂ :0	30nm Cr + 170nm Pt	<1 %	112	189k
30nm Cr + 500nm Pt	500 nm ZnO	80W 300C Ar:10 O ₂ :2	30nm Cr + 170nm Pt	2-3%	86	187k
30nm Cr + 500nm Pt	500 nm ZnO	80W 300C Ar:8 O ₂ :4	30nm Cr + 170nm Pt	3-4%	84	170k
20nm Ti + 150nm Pt	500 nm ZnO	80W 300C Ar:6 O ₂ :6	30nm Cr + 170 nm Ru	5-6%	82	160k

As shown in Table 2.2, the k^2t factors for these samples were characterized that ranges from below 1% to 5-6% by increasing the oxygen to argon gas ratio, which hypothetically resulted in better c-axis oriented and more densely packed grains. However, the ZnO thin film deposition rate decreases from 112 nm/hr to 82 nm/hr due to the increasing oxygen (flow) concentration. According to the literature, with the increment of the oxygen content, the number of Ar ions decreases in the sputtering ambient, therefore lowering the sputter deposition rate. Also, oxygen chemisorbs on the target and forms a surface layer of adsorbed oxygen. This layer inhibits the

sputtering of the atoms. It was also observed that the sheet resistance of deposited ZnO thin film decreases as more oxygen comes into play during an RF sputtering process.

2.4.4 Conclusions of ZnO Characterizations

The thicknesses of ZnO thin film samples have a significant influence on the peak intensity of XRD scanned results since the x-ray beam will penetrate through the thin film at a certain depth. Moreover, the process temperature during sputtering ZnO also makes a sensational impact on the crystalline orientation and density of ZnO thin film, which can be reflected by measured XRD spectra. It is desirable to have ZnO sputtered under 300 °C with an “oxygen-rich” environment (6 sccm of Argon gas and 6 sccm of Oxygen gas) because the inclusion of oxygen will improve the electromechanical coupling coefficient of ZnO. Finally, an RTP post-annealing will boost the ZnO thin films' quality by relaxation of internal stress and densifying the c-axis aligned columnar grains.

Chapter 3: Fundamental Parameters and Circuit Models of Piezoelectric Resonators

3.1 Fundamental Parameters of Resonators

3.1.1 Resonance Frequencies

“Center frequencies” and “operation frequencies” are commonly mentioned in electronics devices, and a lot of people use these terms to identify the device’s specs, but it is not accurate enough when it is down to the resonator level. In fact, there are typically two resonance frequencies of a resonator, namely the “series resonance frequency, f_s and the “parallel resonance frequency, f_p , and sometimes they are also simply named as the “resonance frequency” and the “anti-resonance frequency,” respectively. In this dissertation, to be clear, f_s and f_p are used.

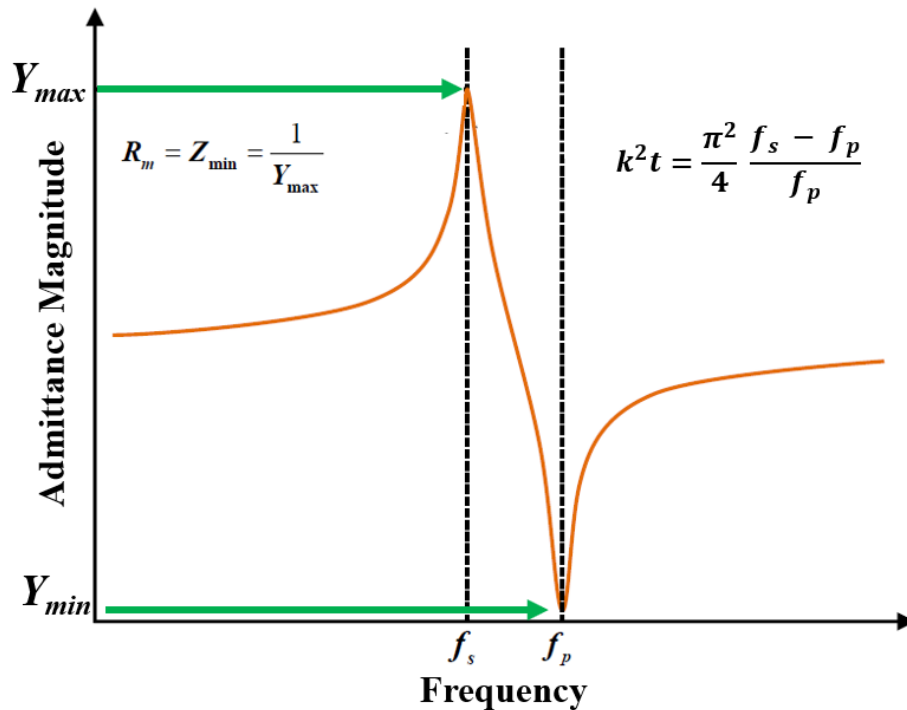


Figure 3.1 A demonstration of frequency response and fundamental parameters of a resonator.

Both the series resonance and the parallel resonance are vitally important performance parameters, which each of them contributes different specifications and purposes. As seen in Figure 3.1, the series resonance occurs when the impedance's magnitude reaches the minimum or the admittance' magnitude reaches the maximum. At this point, the resonator behaves almost like a perfect short circuit:

$$f_s = f(Z_{min}, \text{ or } Y_{max}). \quad (3.1)$$

In contrast, the parallel resonance occurs when the impedance' magnitude reaches the maximum, or the admittance' magnitude reaches the minimum. At this point, the resonator behaves almost like a perfect open circuit:

$$f_s = f(Z_{max}, \text{ or } Y_{min}). \quad (3.2)$$

Typically, the admittance of a resonator is many orders of magnitude higher at the series resonance frequency than at the parallel frequency.

3.1.2 The Electromechanical Coupling Coefficient, k^2

As discussed in the previous chapters, the k^2 of a piezoelectric material stands for efficient energy conversion between the mechanically and electrically. Each of the piezoelectrical material exhibits its own value, which can be flatulated based on the deposition techniques and conditions. For a resonator, the k^2 can represent the energy conversion efficiency at a device level. The resonator's coupling coefficient (k^2) is a vitally important filter design because a higher k^2 enables a wider achievable bandwidth of filters. By looking into the frequency response of a resonator, the k^2 can be evaluated by calculating the distance between the series resonance and the parallel resonance peaks:

$$k_t^2 = \frac{\pi^2 f_p - f_s}{4 f_p} \quad (3.3)$$

3.1.3 The Quality Factor, Q

The quality factor measures how well a resonator is able to sustain the energy within the device, defined as the ratio of the energy stored divided by the energy dissipated per cycle. The energy dissipation can be caused by several loss mechanisms, such as air damping loss, Akhiezer loss, tether loss, diffraction, dielectric loss, and so forth. In the frequency response of a resonator, a higher Q is represented as a sharper resonator peak. It is also noted that both the series resonance and the parallel resonance have their own Q , but more attention is paid to the former because the impedance is much smaller than the other one. A high Q is usually reflected in filter and oscillator designs as fast roll-off rate, lower phase noise, and better frequency stability.

The ways to measure the Q have been well discussed [35][36], and there are a lot of different methods with the results agreed to a small range. For example, the quality factor can be measured by checking the “3-dB” bandwidth:

$$Q = \frac{\Delta f_{3dB}}{f_s} \quad (3.4)$$

Such a method may be problematic when two more peaks are closely squeezed together, and the Q can be measure only at the resonance. Considering the fact that the quality factor is frequency-dependent, the above method is only practical if $Q(f)$ is demanded. To address this issue, one of the methods the frequency-dependent Q (boded- Q) is to calculate the reflection delay:

$$Q(f) = 2\pi f \cdot \tau(f) \cdot \frac{mag(S11)}{1 - mag(S11)^2} \quad (3.5)$$

where both the magnitude of S11 and the delay, $\tau(f)$, as a function of frequency, can be directly read off a Vector Network Analyzer.

3.1.4 Figure of Merit

Depending on the applications, the figure of merit (FOM) of a resonator can be defined differently. For example, the FOM of a resonator for the oscillator design is defined as the product of the series resonance frequency and the Q , expressed as:

$$FOM(oscillator) = f_s \cdot Q(f_s), \quad (3.6)$$

and the FOM of a resonator for the filter design is the product of electromechanical coupling coefficient and the series resonance Q , expressed as:

$$FOM(filter) = k^2 t \cdot Q(f_s), \quad (3.7)$$

because $k^2 t$ is directly proportional to the relative bandwidth of a filter.

3.2 Electrical Circuit Representation of a Piezoelectric MEMS Resonator

The basic principle of operation of a resonator can be translated into a spring-mass-damper model, as shown in Figure 3.2 (a), which by its name, consists of a spring, a mass, and a damper. This mechanical model is universal to any resonating devices containing energy conversions, such as a simple L-C circuit and EM waveguide cavities. As to a piezoelectric MEMS resonator in particular, despite the model describing the resonator's mechanical behavior, the equivalent electrical model is more advanced because it includes the resonator's mechanical and electrical behavior domain.

Figure 3.2 (b) illustrates the electrical circuit model of a typical piezoelectric MEMS resonator. To initiate the vibration, a small input electrical current must be applied to a resonator's electrodes, where the input current is converted into a mechanical force by the piezoelectric effect. This force causes the resonator to vibrate and to generate an electrical signal at the output. An

inductor, capacitor, and resistor in the electrical domain correspond to the inertia, compliance, and damping in a mechanical system, respectively. The transformer represents the energy conversion between the electrical and mechanical domains, which occurs due to the piezoelectric effect.

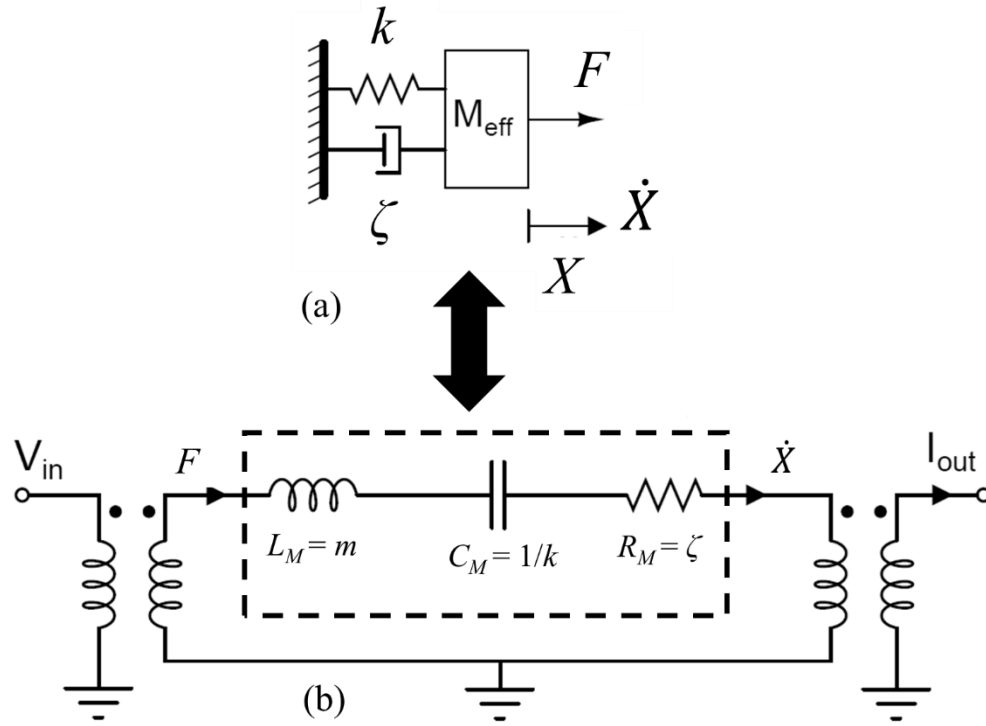


Figure 3.2 (a) The spring-mass system of a resonator; (b) the equivalent electrical model of a piezoelectric resonator.

Table 3.1 Mapping between Electrical and Mechanical Variable Used in Figure 3.2.

Mechanical Variable	Electrical Analogue
Force, F	Voltage, V
Velocity, \dot{X}	Current, I
Displacement, X	Charge, q
Mass, m	Inductance, L_M
Compliance, $1/k$	Capacitance, C_M
Damping, ζ	Resistance, R_M

Table 3.1 explains the analogy parameters' relationship between the mechanical and electrical domain in the two mentioned models. In Figure 3.2 (b), an electrical voltage (U) at the

input terminal is converted to a force (F) through a transduction factor η_{in} and a velocity (\dot{X}) at other output terminal is transduced to a current (I) through a transduction factor η_{out} .

$$F(t) = \eta_{in}U(t) \quad (3.8)$$

$$I(t) = \eta_{out}\dot{X}(t) \quad (3.9)$$

If adding a harmonic motion at angular frequency $\omega_0 = 2\pi f_0$, and ignoring any phase information, Equation (3.8) and Equation (3.9) can be written as:

$$F = \eta_{in}U \quad (3.10)$$

$$I = \eta_{out}\omega_0 X \quad (3.11)$$

where X becomes the displacement. At the series resonance frequency, the imaginary part of the impedance is canceled by the reactive components L_M and C_M , resulting in the resonator's impedance is purely resistive. Therefore, the motional resistance R_M of the resonator is given as:

$$R_M = \frac{U}{I} = \frac{F}{\eta_{in}\eta_{out}\omega_0 X} \quad (3.12)$$

Similarly, in the mass-spring-damping model, the motional resistance can be extracted by dividing the damping factor by the transduction factor, expressed as:

$$R_M = \frac{\zeta}{\eta_{in}\eta_{out}} \quad (3.13)$$

The remaining two other components L_M and C_M used for energy storage, can also be obtained:

$$L_M = \frac{m}{\eta_{in}\eta_{out}} \quad (3.14)$$

$$C_M = \frac{k}{\eta_{in}\eta_{out}} \quad (3.15)$$

3.3 Butterworth-Van Dyke (BVD) Circuit Model

The Butterworth-Van Dyke (BVD) model is a classic circuit model commonly used originally for quartz crystal filter designers. The model provides a simplified circuit equivalent model reviewed in the last section and the transcendental functions that completely characterize any resonators used as filter elements. It is very versatile for parameter extraction and design studies in various resonators with different transduction mechanisms. Currently, the BVD model is still the best method to model the frequency response of piezoelectrically transduced acoustic resonators[37][38]. Engineers rely on the BVD model in almost all filter designs based on FBARs and SAW resonators with long transducer length.

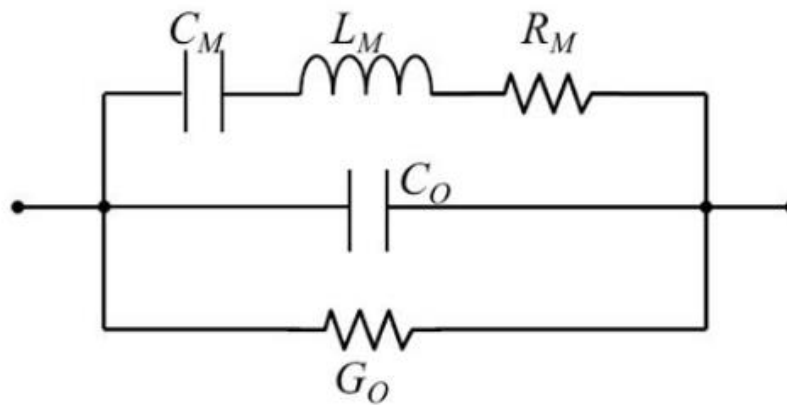


Figure 3.3 Scheme of Butterworth-Van Dyke (BVD) circuit model.

As depicted in Figure 3.3, the Butterworth-Van Dyke (BVD) model is a five-element circuit model that consists of a mechanical branch including a motional inductance (L_m), a motional capacitance (C_m) and, a motional resistance (R_m) connected in series which corresponding to the mass, compliance, and dimpling in the mechanical domain of the resonator. There are also two branches containing a static capacitance (C_0) and a static conductance (G_0) in parallel with the motional arm. For piezoelectric acoustic resonators, the motional terms C_m and L_m represent the acoustic energy storage, and the static capacitance C_0 describes the static capacitance formed by

the capacitance between the interdigit-transducer (IDT) electrodes and the capacitance between the top and bottom electrodes. The motional resistance R_m and the static conductance G_0 reflect the energy loss mechanisms and therefore determine the quality factor and, hence, series resonance and the parallel resonance. The series resonance frequency occurs when the reactance of L_m cancels out the reactance of C_m , resulting in:

$$f_s = \frac{\omega_s}{2\pi} = \frac{1}{2\pi} \frac{1}{\sqrt{L_m C_m}} \quad (3.16)$$

whereas the parallel resonance frequency (f_p) occurs when the susceptance of the motional arm (L_m and C_m) cancels out the susceptance of the static capacitance C_0 , with f_p expressed as:

$$f_p = \frac{\omega_p}{2\pi} = \frac{1}{2\pi} \frac{1}{\sqrt{\frac{L_m C_m C_0}{C_m + C_0}}} \quad (3.17)$$

The impedance (Z) in the BVD equivalent circuit model is expressed as:

$$Z(s) = \frac{s^2 + \left(\frac{R_m}{L_m}\right)s + \omega_s^2}{1 + sR_m C_0 + \frac{C_0}{C_m} + s^2 L_m C_0} \quad (3.18)$$

Recalled that the quality factors are primarily set by the motional resistance and the static conductance, the Q_s and the Q_p are expressed in:

$$Q_s = \frac{\omega_s L_m}{R_m} = \frac{1}{\omega_s C_m R_m} \quad (3.19)$$

and

$$Q_p = \frac{G_0}{\omega_p C_m} \quad (3.20)$$

where ω_s and ω_p are the angular series resonance frequency and the angular parallel resonance frequency, respectively.

The electromechanical coupling coefficient (k^2t) can also be calculated from the BVD circuit model by measuring the distance between the series resonance and the parallel resonance, expressed as:

$$k^2t = \frac{\omega_p^2 - \omega_s^2}{\omega_p^2} \quad (3.21)$$

By employing the mechanical energy (U_M) and electrical energy (U_E) of the resonator body, k^2t can be expressed [37] as:

$$k^2t = \frac{U_M}{U_E + U_M} = \frac{\frac{1}{2}C_m V^2}{\frac{1}{2}C_0 V^2 + \frac{1}{2}C_m V^2} = \frac{C_m}{C_0 + C_m} \approx \frac{C_m}{C_0} \quad (3.22)$$

If the capacitance ratio r is defined as in:

$$r = \frac{C_0}{C_m} \quad (3.23)$$

the electromechanical coupling coefficient k^2t can directly be related to r , expressed as [38]:

$$k^2t = \left(\frac{\pi^2}{8}\right) \cdot \left(\frac{1}{r}\right) \cdot \left(1 - \frac{1}{r}\right) \quad (3.24)$$

As seen in Equation 3.38, the k^2t is inversely proportional to the capacitance ratio, so it is more favorable to lower the static capacitance when designing resonators. In the later chapters, the capacitance ratio will be optimized using an innovative post-process technique by introducing the air cavities in between the IDT finger electrodes.

With the implementation of the BVD circuit, the piezoelectric resonators can be more accurately design and tuned by manipulating the values of the five elements in the model. More importantly, the frequency response of the individual resonator can be well controlled by adjusting the parameters during the resonator designs. It is crucially important for filter design because the

typical ladder filter topology consists of multiple pairs of series and shunt resonators with the right amount of frequency offset.

Beyond understanding the resonance frequencies, it is also necessary to know how the resonator behaves at other frequencies. In Figure 3.4, the estimated BVD circuit models are presented at series resonance and parallel frequencies and when the frequency is far off the resonance.

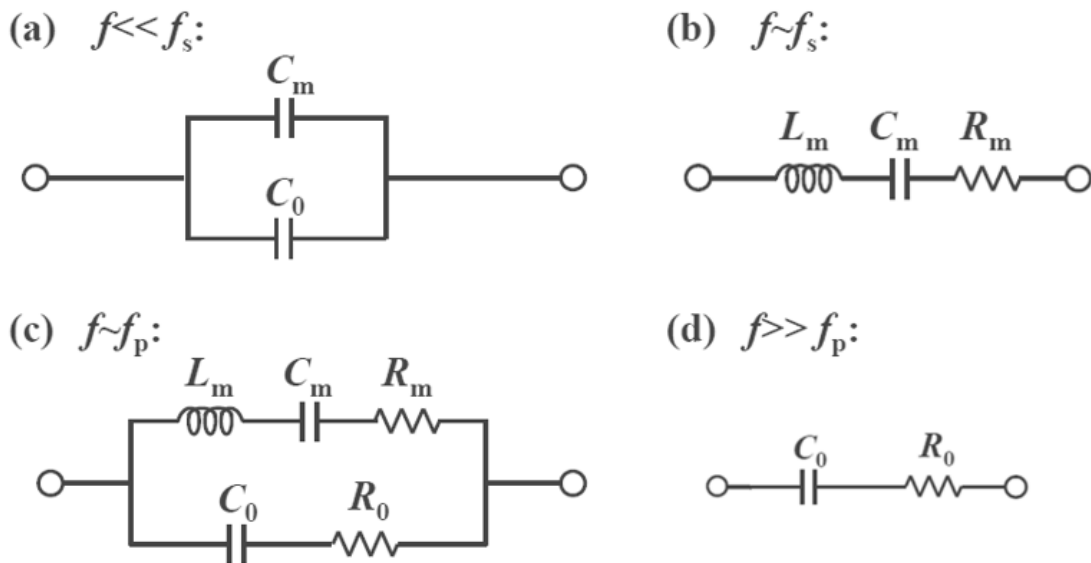


Figure 3.4 Estimated Butterworth-Van Dyke (BVD) circuit models at different frequency ranges.

It can be easily observed in Figure 3.4 (a) and (d), when far off the resonance frequencies, the resonator basically looks like a capacitor. In Figure 3.4 (c), when the resonator is at the series resonance frequency, the reactive part of the motional inductor and the motional capacitance is near zero, so the current can only go through the motional mechanical branch. The impedance at this time is primarily determined by the motional resistance, which is typically below 5 ohms. It is why the impedance of the resonator reaches at the series resonance. As seen in Figure 3.4 (c), at the parallel resonance, all the elements in the BVD circuit model are employed. The current

circulates in the moitonal mechanical and the static branches back to forth, resulting in no output signal can be detected at the terminals.

Chapter 4: Operation Modes and Finite Element Simulation Studies of Piezoelectrically-transduced Resonators

4.1 Operation Modes Studies of Piezoelectrically-transduced Resonators

The vibration modes of the piezoelectrically-transduced acoustic resonators can be controlled by the resonators' geometries and excitation metrologies. As previously discussed, the piezoelectric coefficients are in a matrix that piezoelectric can occur in different directions. Four different vibration modes can be achieved[39][40].

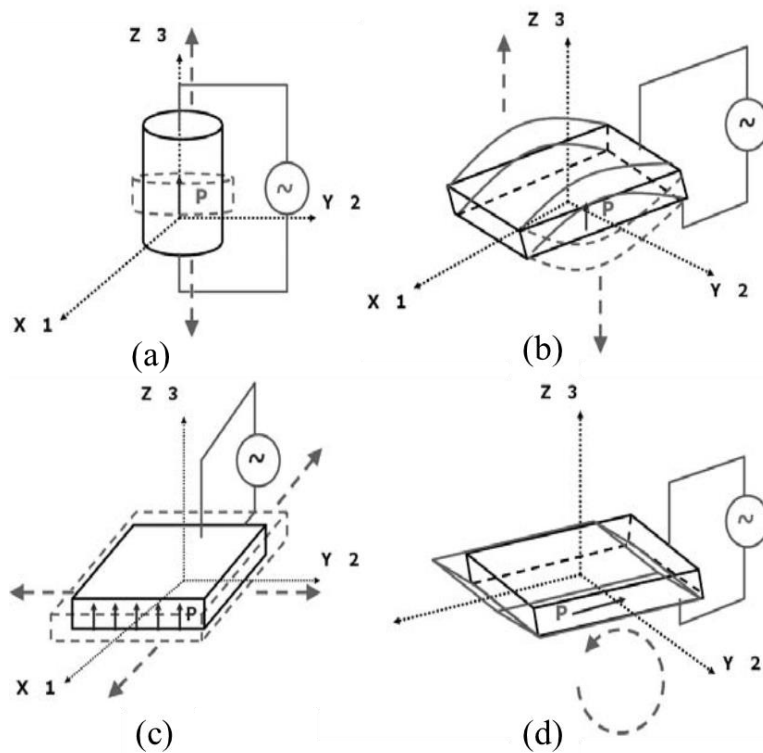


Figure 4.1 Vibration modes of piezoelectrically-transduced acoustic resonators: (a) longitudinal (“33” mode); (b) extensional (“31” mode); (c) thickness-transversal (“31” shear mode); and (d) lateral-shear (“15” mode). Courtesy of Takai et al. [39]. See permission in Appendix A.

When an electrical excitation is initiated across the top and the bottom surface of the piezoelectric rectangular plate, four types of mechanical vibrations are generated in two directions, as demonstrated in Figure 4.1, and they are the thickness vibration along with the electric field (“33” longitudinal or thickness mode) and the extensional vibration (“31” flexural mode) that is perpendicular to the electric field. Additionally, there is also the transversal vibration (“31” shear mode) that the center of the rectangular plate bends inward or outward, and the shear-mode vibration (“15” shear mode) caused by a twisting force.

Considering a resonator with a piezoelectric body in a rectangular block as seen in Figure 4.2, with the length of l and width of w , when an electrical field is applied in the z -direction, the lateral extensional (i.e., Length or Width Extensional Mode) vibration can be observed driven by force into the x -direction.

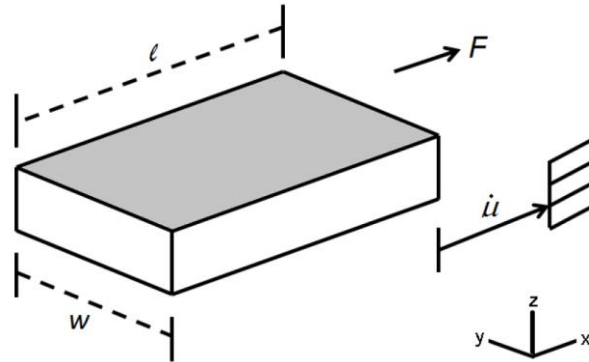


Figure 4.2 Longitudinal mode rectangular plate resonator.

Such vibration mode can be mathematically analyzed by a set of wave equations in [40], if only concerning the force that generates stress in the $u(x)$ direction, the wave equation in the x direction can be derived as:

$$\frac{E}{\rho} \frac{\partial^2 u}{\partial x^2} = -\omega^2 u \quad (4.1)$$

here E is Young's modulus, ρ represents the material density of the block, and u is the displacement. By applying the linear differential equation theory, a general solution to Equation (4.1) can be expressed as:

$$u(x) = A \sin kx + B \cos kx \quad (4.2)$$

where x is the coordinate in the length direction, and k is the propagation constant.

The two sides of the resonator block can be located by setting $x = 0$ and $x = l$. Therefore, by using the boundary condition $x = 0$ to Equation (4.2), the value of A can be found as:

$$\frac{\partial u}{\partial x} \Big|_{x=l}^{x=0} = Ak \cos kx - Bk \sin kx = 0 \quad (4.3)$$

$$Ak \cos kx - 0 = 0 \text{ or } A = 0 \quad (4.4)$$

$$u(x) = B \cos kx \quad (4.5)$$

By applying another boundary condition $x = l$ to Equation (4.13), the result is given as:

$$\sin kl = 0, \text{ for } k_n l = n\pi, n = 1, 2, 3, \dots \quad (4.6)$$

Therefore, by substituting equation (4.1) into (4.5), k can be expressed as:

$$k = \omega \sqrt{\frac{\rho}{E}} \quad (4.7)$$

By substitute the values of kn from Equation (4.6) into Equation (4.7), the higher-order (n^{th}) resonance frequencies of the length extension mode can be express as:

$$f_n = \frac{n}{2l} \sqrt{\frac{E}{\rho}} \quad (4.8)$$

The above describe analytical approach can also be adopted to the other piezoelectric acoustic resonators with different geometries and mode shapes. For example, as to a circular disk Contour Mode (i.e., fundamental Extensional Modes), as seen in Figure 4.3, the resonance frequency can be derived using a similar approach.

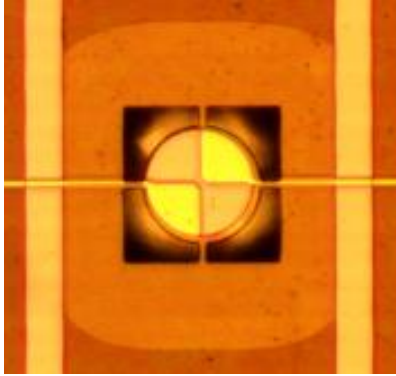


Figure 4.3 A microscope-view of a piezoelectrically-transduced disk resonator.

The equation of the resonance frequency can be expressed as:

$$f_{n(disk)} = \frac{a_n}{R} \sqrt{\frac{E}{\rho}} \quad (4.9)$$

where R is the radius of the resonator disk and a_n is a mode-dependent scaling. Unlike the rectangular-shaped resonator having the single direction of each vibration across the block, the round-shaped disk resonator can exhibit non-axisymmetric vibration modes showing in Figure 4.4.

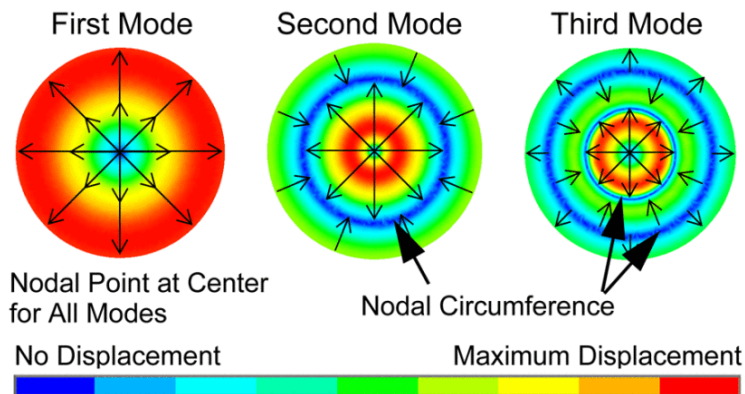


Figure 4.4 FEM nodal analysis using COMSOL Multiphysics® of a circular membrane vibrating in the first four contour modes. Courtesy of Clark et al. [41]. See permission in Appendix A.

By assuming a Poisson's ratio $\mu = 0.3$, the estimated frequency scaling factor a_n for the first four disk fundamental Contour Modes are: $a_1 = 0.272$, $a_2 = 0.342$, $a_3 = 0.418$, and $a_4 = 0.493$

[41]. a1 and a2 are also known as the fundamental Wine Glass mode and the first Radial Contour mode, respectively.

As introduced in the earlier chapters, the contour mode resonator (CMR) is also sometimes referred to as the Lamb wave resonator (LWR). As presented in Figure 4.5, the Lamb wave modes contain multiple-order symmetric (denoted as “S_n”) or asymmetric vibration modes (denoted as “A_n”) that have the displacements in x- and z-directions simultaneously.

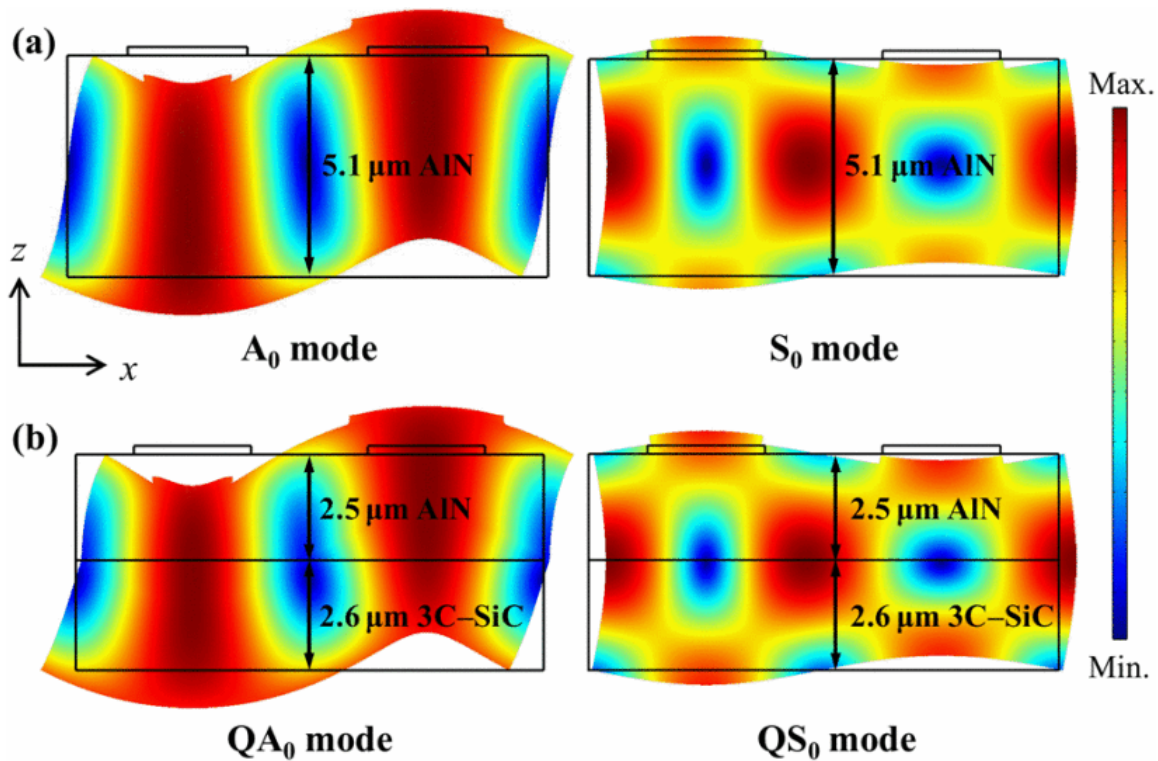
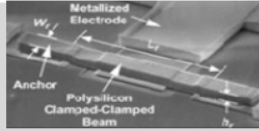
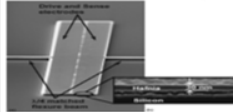
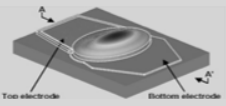
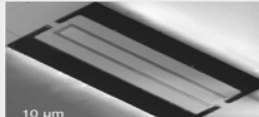


Figure 4.5 Multiple-order of displacements of Lamb wave modes from FEM nodal analysis using COMSOL Multiphysics. Courtesy of Lin et al. [44]. See permission in Appendix A.

Table 4.1 summarize the approximate resonance frequency for different vibration modes. It is observed that the resonance frequencies are all proportional to the acoustic velocity of the vibrating material, which is equal to the square root of the ratio of Young’s modulus over the material densities. Depending on the different mechanical vibration mechanisms, individual dimension parameters are applied to the equations.

Table 4.1 A Summary of Resonance Frequency Calculations for Different Vibration Modes.

Mode of Vibration	Frequency	Range	Example
Flexural	$f_0 \propto \frac{T}{L^2} \sqrt{\frac{E}{\rho}}$	[10 kHz-10 MHz]	
Shear Mode	$f_0 \propto \frac{1}{2T} \sqrt{\frac{G}{\rho}}$	[800 MHz-2 GHz]	
Thickness Extensional	$f_0 \propto \frac{1}{2T} \sqrt{\frac{E}{\rho}}$	[500 MHz-20 GHz]	
Contour Mode	$f_0 \propto \frac{1}{2W} \sqrt{\frac{E}{\rho}}$	[10 MHz-10 GHz]	

4.2 Finite Element Method on Piezoelectrically-transduced Acoustic Resonators

To facilitate analyzing and understanding the different vibration modes, one of the most convenient ways is to carry out the finite element method (FEM) simulation, which enables to investigate and analyze the electrical field and the strain/displacement distribution of each of the resonance modes including both the target mode and spurious modes. In the meantime, the FEM simulation results also guide the design trends by including multiple degrees of freedom in the model setups. In this section, many design variations will be exploited in the FEM simulation studies using the Comsol simulation tool.

4.2.1 3-D Model Setup for Piezoelectrically-transduced Acoustic Resonators

To carry out the piezoelectric effect in the FEM simulation, electrostatics and solid mechanics have been selected as the physics engaged, representing the electrical and the mechanical domain analysis. These two physics can practically solve the partial differential equations independently or coupled as the multiphysics for the piezoelectric effect. The resonator selected for FEM studies is based on a rectangular-shaped ZnO thin-film piezoelectric MEMS

acoustic resonator, as displayed in Figure 4.6 (a). The device consists of five 13 μm -wide IDT finger electrodes, 3 μm apart, making the pitch size equal to 16 μm . Figure 4.6 (b) shows the device's three-dimension meshed model in Figure 4.6 (a). In addition, the resonator structural body, the perfectly matched layers (PML) are included to imitate the function of air, reflecting acoustic energy at the edges of the resonator. The PLM is critically important to reduce the simulation time.

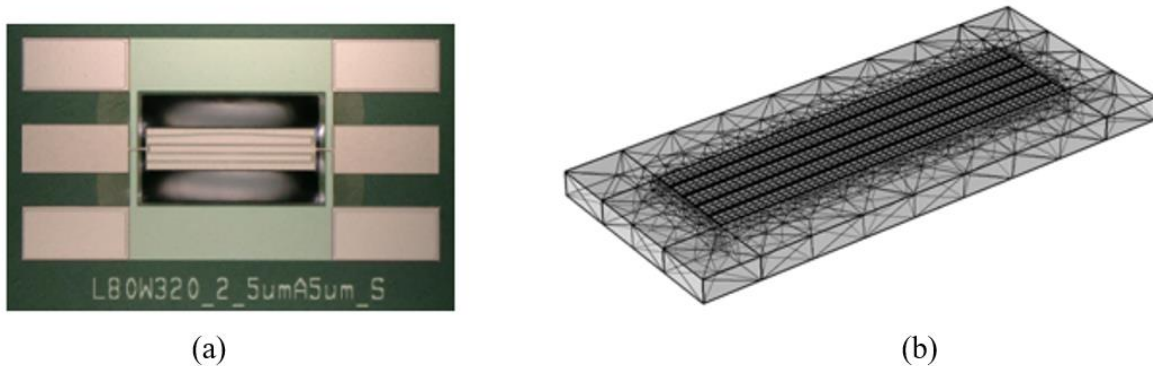


Figure 4.6 (a) The microscope image of a ZnO thin-film piezoelectric rectangular resonator that has a body dimension of 320 μm x 80 μm , 5 IDT fingers, a finger pitch size of 16 μm ; (b) 3-D meshed model for FEM simulation of the fabricated resonator design in (a).

To duplicate a 0dBm power input of the Vector Network Analyzer (VNA) measurement, a 1 mW was applied to the odd number of the IDT fingers in the simulation, and the other two IDT fingers were set at 0 watt. The bottom electrode layer was set as ground. By sweeping the ports' inputs, the reflection coefficients and the transmission coefficients can be produced in the FEM simulation.

4.2.2 FEM Studies of Piezoelectric Thickness

A piezoelectric MEMS resonator's performance drastically relies on the thickness and the crystal orientation of the piezoelectric material, which are thoroughly studied via FEM simulation in this work. The acoustic wave velocity can be largely affected in terms of the variation of the piezoelectric layer's thickness. The parametric study covers the thickness of the piezoelectric material (ToPZ), ZnO in this case, ranging from 0.2 μm to 0.8 μm . The thickness is limited to 0.8

μm by considering the fabrication constraints that will become more complicated if the piezoelectric material is too thick.

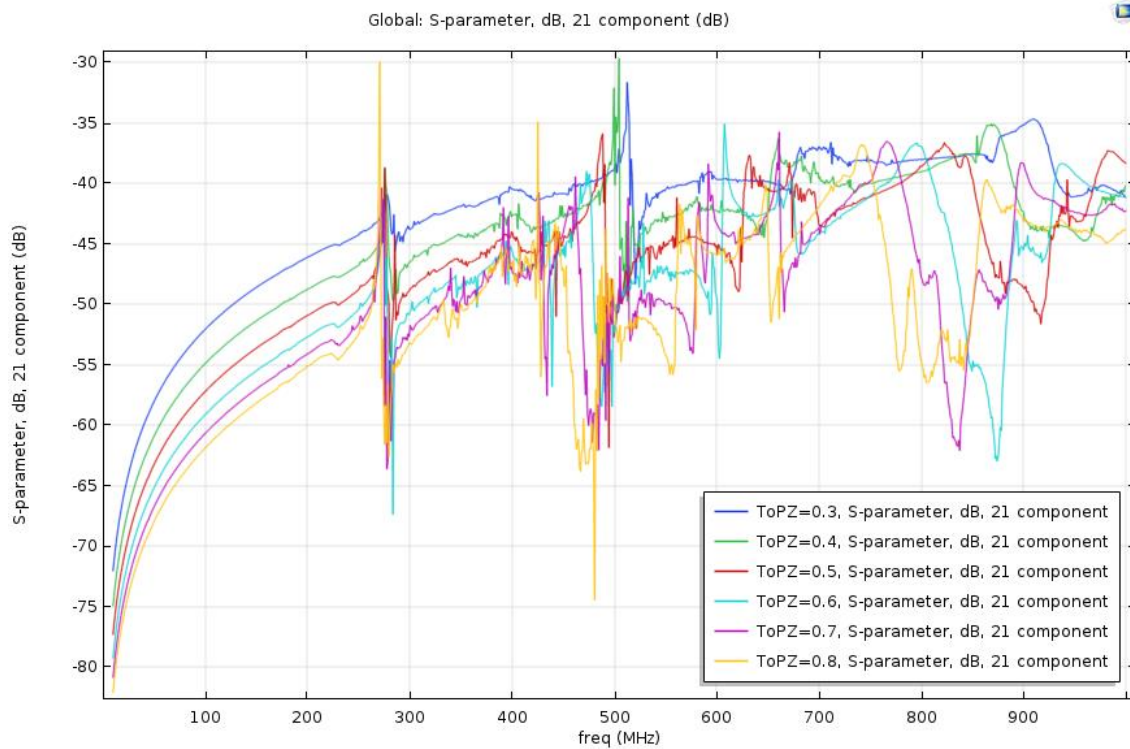


Figure 4.7 The FEM simulated frequency responses of the resonators as a parametric study of the piezoelectric material's thickness ($ToPZ$) ranging from $0.2 \mu\text{m}$ to $0.8 \mu\text{m}$.

As shown in Figure 4.7, the simulated frequency response shows the capacitive feedthrough level is lowered as the thickness of the piezoelectric ($ToPZ$) layer is increased when the parasitic capacitance decreases between the top electrode and bottom electrode. Meanwhile, with the piezoelectric layer's set at $0.8 \mu\text{m}$, the first order width extensional mode's signal-to-noise ratio appears to be significantly higher at 280 MHz . Whereas more spurious modes are found when the thickness is higher than $0.5 \mu\text{m}$, the thickness dominated mode shows the resonance frequency goes higher with $ToPZ$ gets thinner, as can be seen in the circled area.

4.2.3 FEM Studies of Crystalline Orientations of Piezoelectric Material

The crystalline orientation of piezoelectric thin-film materials can be tailored with different methods depending on what and how the piezoelectric material is deposited. For example, a PZT thin film's crystal orientation usually requires a “poling” process, during which an extremely high electrical potential difference is applied across both sides of the deposited piezoelectric material.

It is known that for surface acoustic wave resonators with a piezo-crystal substrate, such as LiNbO_3 and LiTaO_3 , the acoustic wave diffraction and energy leaked can be suppressed by precisely tuning the crystal cut angle, for example, Y 128° or Y-X 42° . It is also meaningful to explore the similar impacts by the orientation alignments on the piezoelectric ceramic material. Under optimized conditions, the crystallites in ZnO thin films deposited by sputtering techniques grow preferentially with the c-axis perpendicular to the substrate surface, but it is also reported that the crystalline quality of sputtered ZnO films, in particular the orientation of the crystallites in the film with respect to the substrate surface [42][43]. A number of factors can contribute, and the most important one is the nature of the substrate, such as chemical composition, crystalline orientation, and surface roughness. Also, the sputtering parameters, including pressure, substrate temperature, sputtering power, can play a significant role in adjusting the crystal orientation of the sputtered films slightly.

Currently, very few research has reported how to acquire and control the crystal orientation offsets by sputtering depositions. Figure 4.8 shows the FEM simulated frequency responses of the chosen resonator design with the piezoelectric material's crystal orientation (ToPZ) gradually varied from 0 degree (c-axis aligned and perpendicular to the substrate surface) to 40 degrees. As can be seen, a 10-degree misalignment concerning c-axis aligned orientation the simulated response surprisingly shows a performance enhancement below 600 MHz, but the feedthrough noise level becomes notably higher beyond 600 MHz.

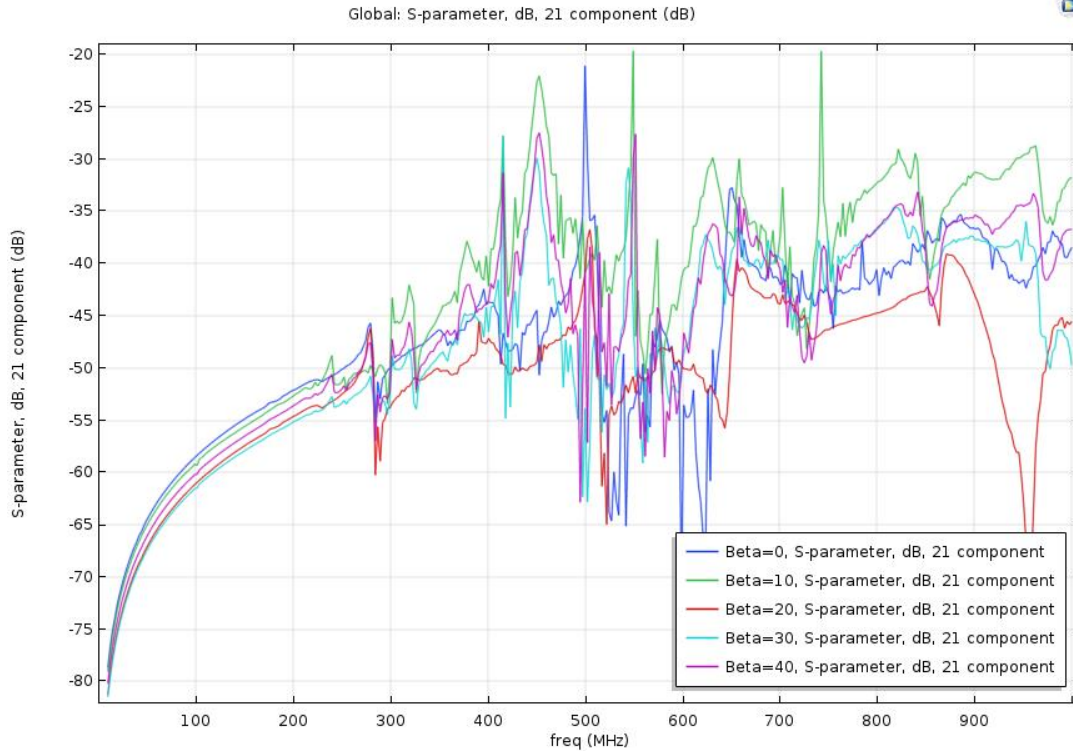


Figure 4.8 The FEM simulated frequency responses of the resonator's crystal orientation of the piezoelectric layer (ToPZ) ranging from 0 degree (c-axis aligned perpendicular to the surface) to 40 degrees.

4.2.4 FEM Studies of Aperture Size

The next study by the FEM simulations focuses on exploring the performance impact made by different aperture sizes defined as the interdigital transducer length. If without changing the pitch size and the number of the IDT fingers, the overall transducer area can be controlled by varying the aperture size. In RF filter designs, the resonator's area is an important parameter to shape the resonance responses. For instance, the resonance response's shape can be sharper of a SAW resonator connected in series. For BAW resonator designs, the electrodes' area can directly affect characteristic impedance, where a smaller FBAR typically associates larger impedance. For contour mode resonators, the impact from the transducer area has yet been thoroughly studied.

The purpose of this FEM experiment is to see how the electrode area (overlapped area of the top and bottom metal electrodes) affects the performance of the resonator while keeping the

same IDT pitch size. Theoretically, the variation of the aperture size (AP) should not influence the resonance frequencies because they are determined by the materials' pitch size and acoustic velocity. A change in AP may affect the feedthrough level due to a change in parasitic capacitance. It may also impact the insertion loss, given that more electrical charges are collected as the AP (effective electrode area) increases.

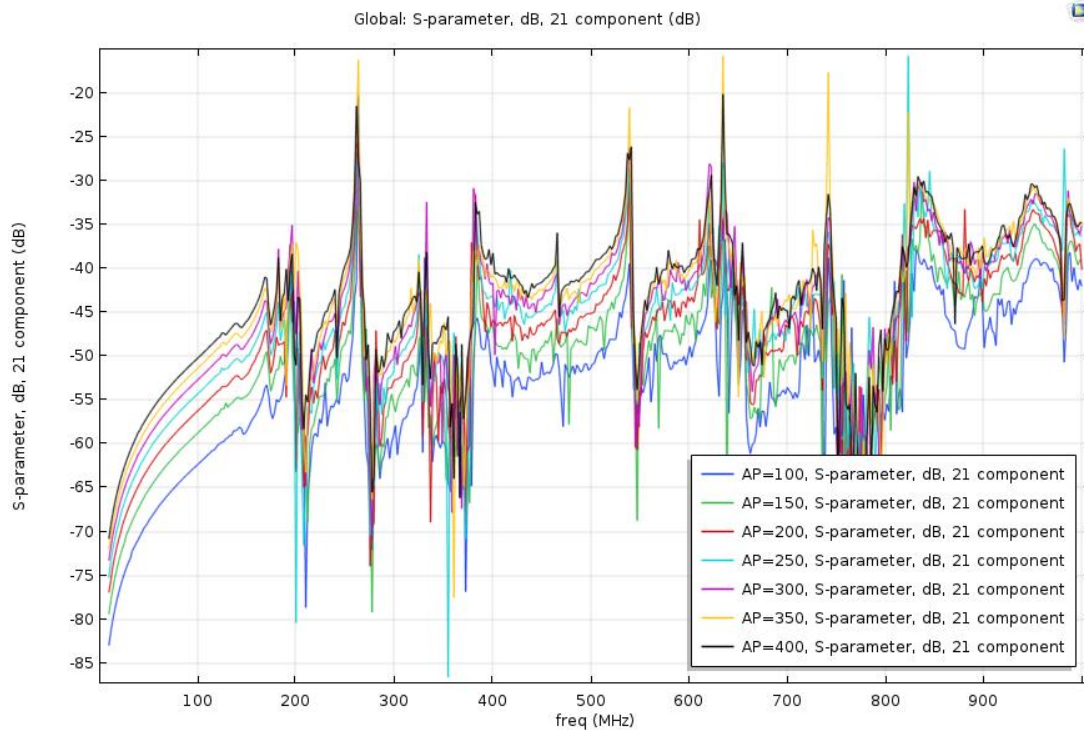


Figure 4.9 The FEM simulated frequency responses of the resonators with aperture size (AP) ranging from 100 μm to 400 μm .

As seen in Figure 4.9, the aperture size (AP) is increased from 100 μm to 400 μm with an increment of 50 μm . As expected, the variation of the aperture sizes has negligible impacts on the resonant frequencies. Still, the feedthrough level is elevated by 10 dB and changes in the peak amplitude as the aperture size increases from 100 μm to 400 μm . When the aperture size approaches 350 μm , the insertion loss has reached its lowest level.

4.2.5 FEM Studies of Finger-to-gap Ratio

Previously, first principle assumptions have been made in this regard that a larger IDT electrode area will generate more electrical charges from the piezoelectric effect. A smaller gap size will bring the adjacent electrodes closer to lead to a more severe capacitive parasitic effect. In the context of the finger-to-gap ratio of contour mode resonators, very few prior reports discuss the tradeoff between the width of the IDT fingers and the gap between them while keeping the pitch size (the sum of the IDT finger width and gap) fixed. Therefore, it makes great sense to scrutinize this tradeoff through the parametric study through FEM simulations.

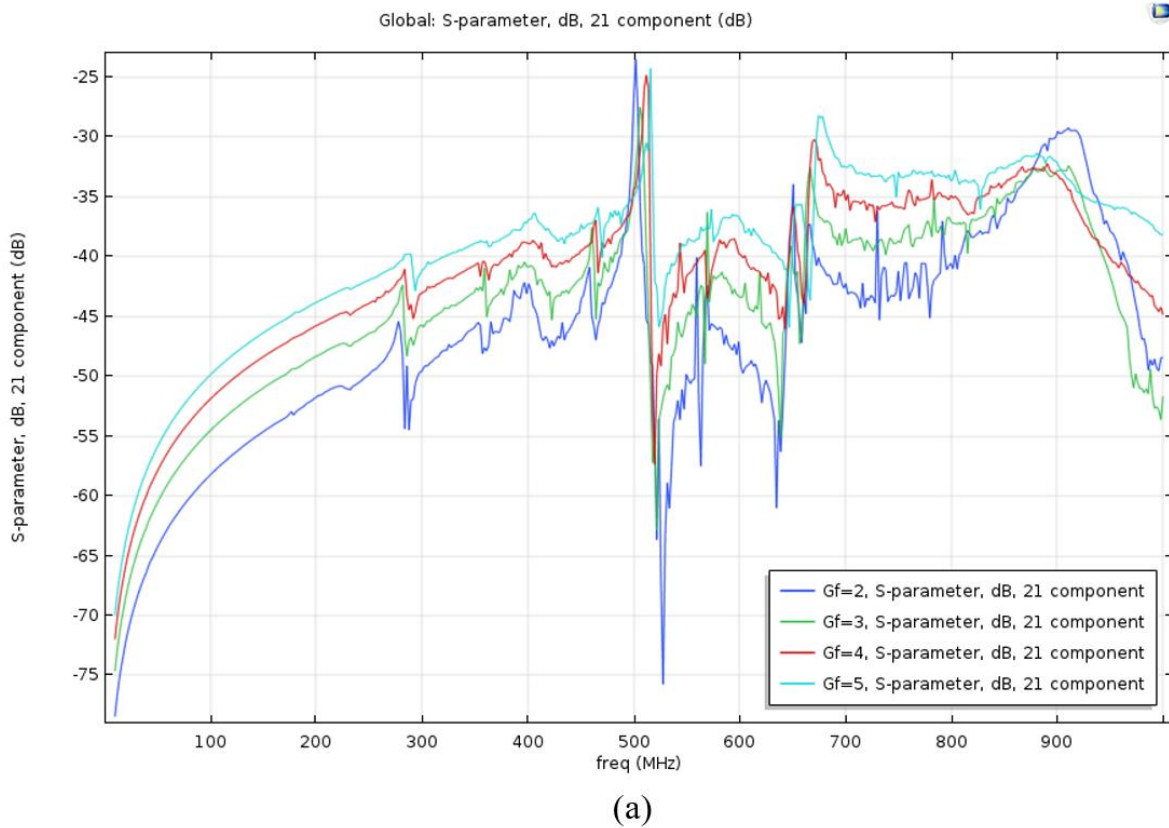
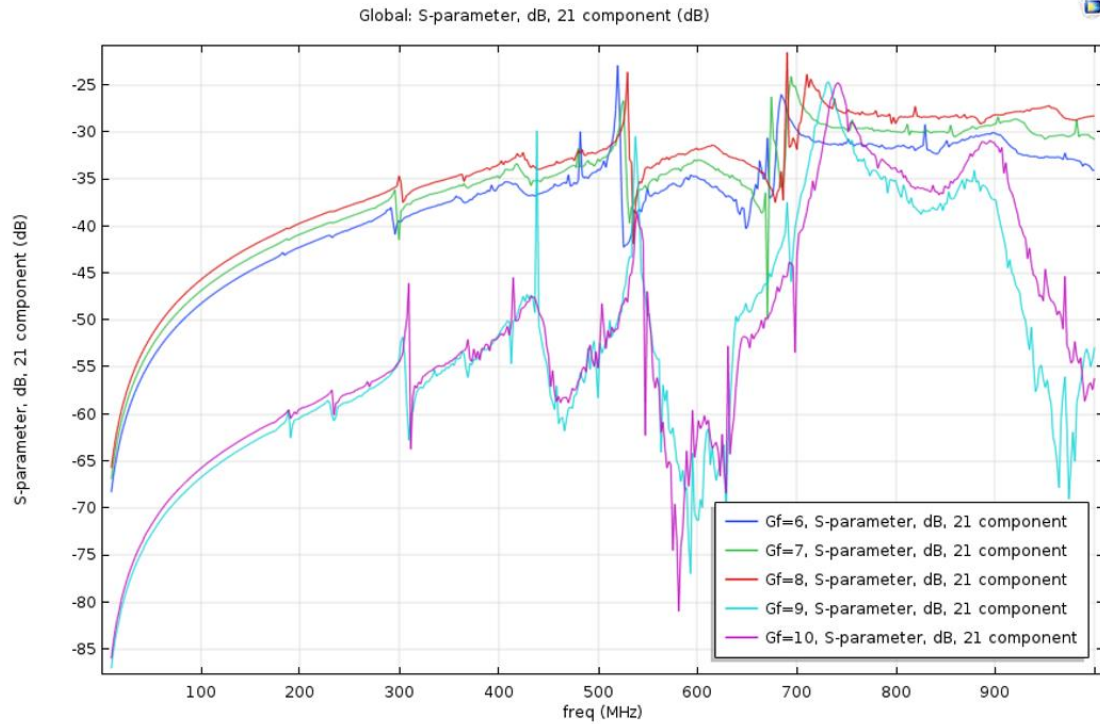


Figure 4.10a The FEM simulated frequency responses of the resonators with different finger-to-gap ratios. The pitch size is $16 \mu\text{m}$ along with the distance in between IDT electrode fingers (G_f) ranging from $2 \mu\text{m}$ to $5 \mu\text{m}$.



(b)

Figure 4.10b The FEM simulated frequency responses of the resonators, which have the same pitch size of $16\ \mu\text{m}$ along with the distance in between IDT electrode fingers (G_f) ranging from $6\ \mu\text{m}$ to $10\ \mu\text{m}$.

In this work, the pitch size is set to be $16\ \mu\text{m}$ while varying the gap-by-finger (G_f) value from $2\ \mu\text{m}$ to $15\ \mu\text{m}$, which corresponds to the IDT electrode width of $14\ \mu\text{m}$ to $1\ \mu\text{m}$, respectively. Figure 4.10 (a) shows the frequency response of the simulated resonator with varied gap sizes from $2\ \mu\text{m}$ to $5\ \mu\text{m}$, which results in a slight shift of the resonance frequency to the higher frequencies as the gap size is increased even though the pitch size maintains the same. As seen, the static capacitive feedthrough level is elevated as the gap size gets wider up to $8\ \mu\text{m}$ (with an IDT finger width of also $8\ \mu\text{m}$). However, in Figure 4.10 (b), it is observed that when the gap size is greater than $9\ \mu\text{m}$ that corresponds to an electrode finger width less than $7\ \mu\text{m}$, the feedthrough levels drastically drop by about $20\ \text{dB}$, and very minimal impacts occur to the feedthrough level when the gap size is further extended beyond $9\ \mu\text{m}$.

Chapter 5: Fabrication Process and Measurement Results

In this dissertation work, the proposed ZnO thin-film piezoelectrically-transduced MEMS acoustic resonators have been fabricated and measured at the University of South Florida (USF). The first two sections in this chapter present the resonators' detailed fabrication processes implemented on two types of wafers: high-resistivity silicon wafers and diamond-coated silicon wafers. A comparison of measured results demonstrates the advantage of employment of the thin-film diamond layer as the primary resonator structural body material in aspects of resonance frequencies and quality factors. The experimental results support analyzing the outcomes of many design techniques aiming to improve the resonators' performance in different ways, as detailed in the later sections. More specifically, a variation of tether design techniques is discussed to investigate the impacts of varying numbers and different dimensions of the tethers applied to the resonators while keeping the other parameters the same. Furthermore, the investigation of phononic crystals in the tethers is also thoroughly reported. The measurement results indicate different influences made by employing the phononic crystals of different shapes and quantities.

Three variations of the bottom electrode designs are included in this work, presenting a difference in the resonance response. As to the top IDT electrodes fingers, different finger-to-gap ratios are explored in the fabricated resonators to keep the pitch size the same. The goal is to find the optimized metal-to-gap ratio in terms of the capacitance ratios and insertion loss. Therefore the signal-to-noise ratio (SNR) can be enhanced. This is crucially important for mass sensing applications. To further improve the SNR of the acoustic resonators, some well-performed

resonators are cascaded and electrically coupled to significantly lower the feedthrough noise levels.

Moreover, the resonators' dimensions are carefully tuned and compared by changing the aperture size and resonator body shape. These design techniques also served the purpose of improving the capacitance feedthrough levels as well as the quality factors. In the last sections of this chapter, the temperature stability and the power-handling capability of the fabricated resonators are both measured and evaluated, along with the theoretical analysis of both topics.

5.1 Fabrication Process of ZnO Piezoelectric Resonator on Silicon Wafers

The piezoelectrically-transduced resonators were fabricated on high-resistivity wafers with a four-mask photo-lithography process. The first step is the wafer preparation through the RCA clean, which is an essential operation to remove contaminants that remained on the wafers, such as organic particles and other chemical residues. Previous fabrication attempts experienced uniformity problems during the photo-resist spinning, and a simple solvent cleaning could not resolve it. After the RCA clean, the wafers are ready for the fabrications.

The main fabrication process steps are illustrated in Figure 5.1. The bottom electrodes are patterned using a standard lift-off process. The first step is to spin a 4000Å-thick LOR, followed by an AZ1512 photoresist. The LOR photoresist has the advantages of creating an undercut profile on the sidewalls, and the thickness must be at least 1.5 times more than the metal's thickness. A descum process is recommended to ensure no photoresist residue remained in the open area. The exposure is then conducted using EVG 620 mask aligner, and then the photoresist is developed in AZ 726. Depending on the minimum feature size and the designed metal electrodes' thickness, the entire photolithography recipe needs to be characterized. The bottom electrodes are then sputtered with 30 nm Chrome (Cr) as an adhesion layer and 170 nm Platinum (Pt) as the main conductor,

and the patterns turn out nicely by soaking the wafer into a 65°C-heated photoresist stripper for liftoff. The mentioned photoresist and the metal dimensions need to be verified by profilometer tools. The next step is to deposit a 5000-Å thickness zinc oxide thin film by an AJA sputtering tool. The previous chapters discuss the optimized process conditions concerning different material properties. In this process, the ZnO thin films depositions are processed using dual RF power sources at 85 watts, 300 °C for substrate temperature, 5 mTorr for plasma pressure, 1:1 Ar: O₂ ratio along with a total of 12 sccm gas flow, followed by the post-annealing at 600 °C for 15 minutes using a rapid thermal processing (RTP) tool to eliminate the internal film stress.

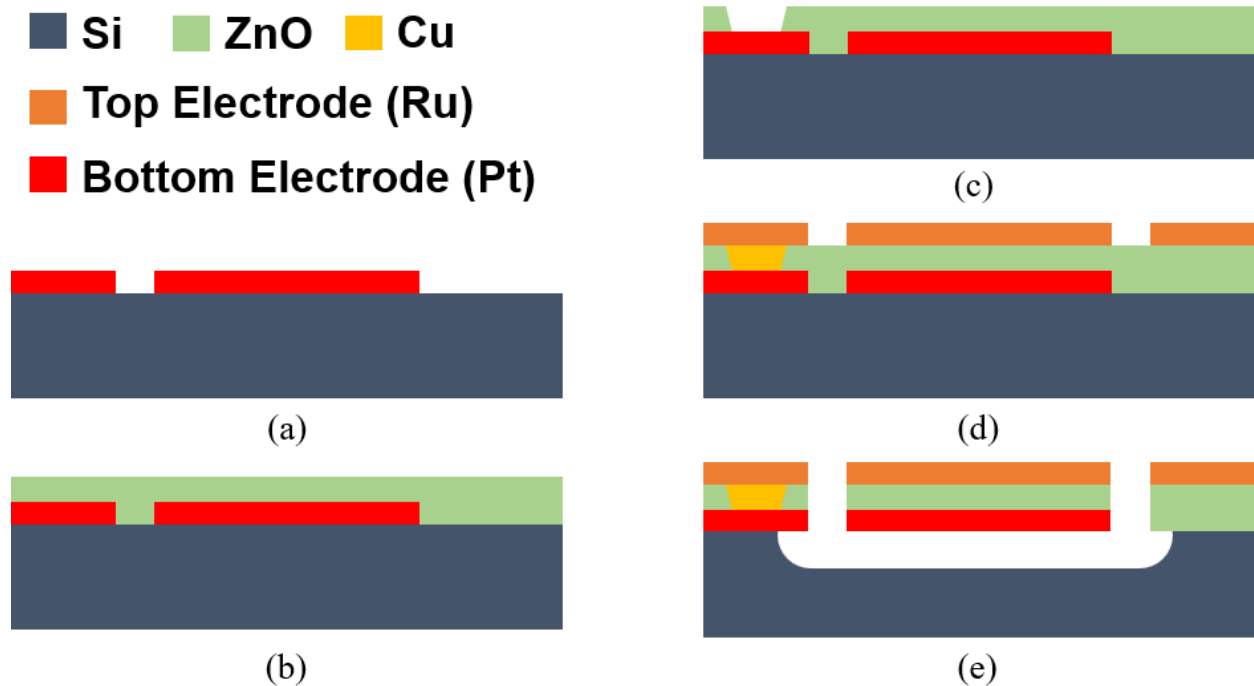


Figure 5.1 Simplified four-mask fabrication process flow of ZnO thin-film piezoelectric MEMS acoustic resonators. (a) Bottom electrode (Cr+Pt) deposition and patterning by a lift-off process; (b) sputtering deposition of the piezoelectric ZnO film; (c) via holes etching through ZnO and Cu filling by a lift-off process; (d) deposition and patterning of top electrodes; (e) ZnO dry etch followed by silicon dry etch.

Figure 5.1 shows that the via openings lithography is done using AZ 1512 photoresist, followed by wet etching through ZnO in a mixed solution of 1: 100 HCl: H₂O. This step is required

for good electrical contact between the top and the bottom electrodes, but note that the via openings do not apply to every device because of the mask specifications. These via holes are then filled with copper through a similar lift-off process with the same mask as the one used for creating the via openings. The top electrodes are also patterned using the same lift-off process for bottom electrodes, but the metal selection is switched to ruthenium, which exhibits similar chemical-resist capabilities, but with better electrical conductivity and less mass loading effect than that of Pt.

The device release process starts with a lithography process with the last-step mask to define the resonator structural bodies. The AZ12XT is used because of its superb chemical resistance to the gas plasma environment in the later steps. For the dry release process, the ZnO thin films are dry-etched in a CH₄-Ar plasma environment by an Adixen AMS-100 Deep Reactive Ion Etching (DRIE) tool. The 5000Å-thick ZnO thin films should be etched away within 8 minutes. Finally, the device resonator body is released by an anisotropic silicon dry etch using pure sulfur hexafluoride gas plasma. The bias power setting is reduced to promote the lateral etch rate. Finally, the remaining AZ 12XT is gently removed in an oxygen plasma environment by the DRIE tool. Special attention to avoid aggressive power must be paid here because, at this moment, the resonator structures are fully suspended and brittle. Previous lessons are learned at this last step that absolutely no wet chemical processing step shall be used on a fully dry-released wafer.

5.2 Fabrication Process of ZnO Piezoelectric Resonator on Diamond-on-Silicon Wafers

Diamond is known to have superb mechanical properties in many aspects. By the employment of the thin film diamond layer as the primary resonator body structural material, the equivalent acoustic velocity of the multi-layer piezoelectrically-transduced ZnO-on-Diamond (TPoD) MEMS resonators is significantly higher, thus resulting in higher resonance frequencies as compared to that silicon counterparts. Also, with its Young's modulus about 8X higher than

that of silicon, the quality factor of MEMS resonators is expected to be also higher than that of silicon devices because the energy is more efficiently conserved within the resonator body made of diamond thin films.

Figure 5.2 illustrates the piezoelectric resonators' fabrication process flow, which is built on a Diamond-on-Silicon substrate. Before the fabrication, the diamond thin films are deposited onto the silicon substrate by chemical vapor deposition provided by an external industrial collaborator. Similarly, this process also starts with bottom electrode deposition using sputtering patterned by a lift-off process. However, the specific recipe may need to be slightly adjusted since the reflection indexes varied based on the different wafers. Then, ZnO thin films, providing the piezoelectric transduction, are uniformly coated by the RF sputtering deposition with the same recipe as in the previous section. The top electrodes deposition and via filling are processed simultaneously after the via holes are opened through the wet etch using diluted hydrochloric acid. Unlike the fabricated process on the silicon wafer, a 2 μm PECVD SiO_2 thin film is used as the hard mask instead of photoresists because photoresists can be easily etched away in the oxygen plasma during the diamond dry etch in the later step. AZ 12XT is used during the lithography for defining the resonator bodies via the PECVD oxide hard mask layer.

The last part of the fabrication process consists of a series of dry etch processes by a DRIE tool to pattern SiO_2 , ZnO, diamond, and Si layers. The PECVD SiO_2 thin films are dry-etched using C_4H_8 and CH_4 gas at $-20\text{ }^\circ\text{C}$, and the etch rate is approximately $4000\text{ \AA}/\text{min}$. ZnO layer is then etched with CH_4 -Ar plasma, followed by etching the diamond layer using a very high RF power of 2800 W along with an additional 300 W substrate biasing power in O_2 plasma. To ensure a vertical side-wall profile, the biasing power needs to be high, but it also generates a fair amount of heat. Therefore, it is recommended to avoid a consecutive process longer than 20 minutes. Finally,

the silicon underneath the resonator body is released using the SF₆ plasma to achieve the structure shown in Figure 5.2 (f). The remaining PECVD SiO₂ thin films need to be carefully removed by a gentle dry etch recipe. Figure 5.2 (g) presents the optional post-processing step to create air cavities (also known as air notches) by removing the ZnO in between the top IDT electrode fingers. The adopted ZnO dry etch recipe has an excellent selectivity to Ru top electrodes, which can eventually survive to maintain the integrity of the fabricated resonators.

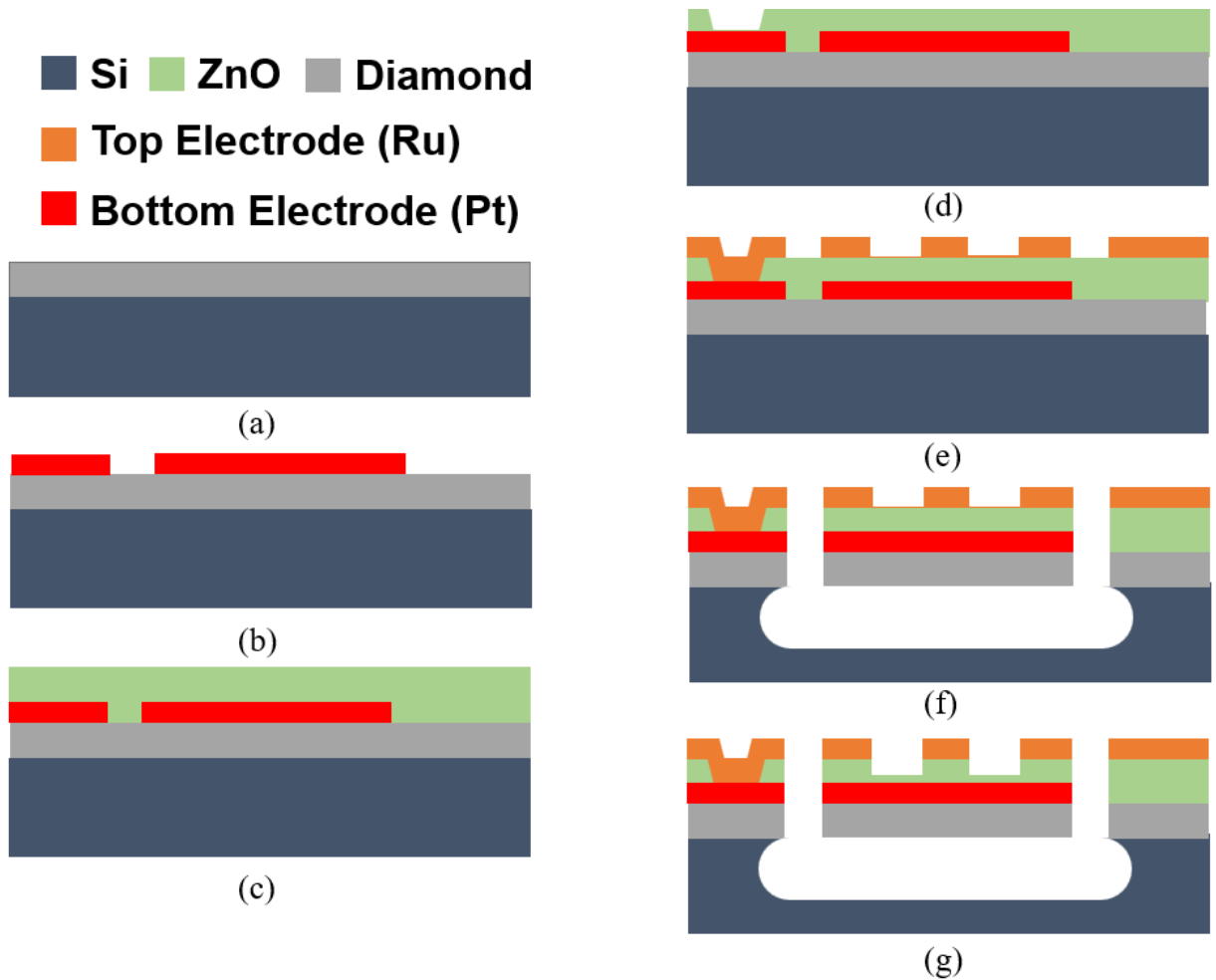


Figure 5.2 Four-masks fabrication process of ZnO piezoelectric resonator on diamond-on-silicon wafers. (a) Chemical vapor deposition of the diamond thin film on silicon; (b) bottom electrode (Cr+Pt) deposition and patterning by lift-off; (c) sputtering deposition of the piezoelectric ZnO film; (d) etch vias through ZnO for bottom electrodes access; (e) deposition and patterning of top electrodes; (f) ZnO dry etch followed by diamond dry etch and Silicon isotropic dry release; (g) optional post-process to create air cavity (also known as notch) in between the adjacent IDT fingers.

5.3 Measurement Results Analysis of Different Design Configurations of Piezoelectrically-transduced ZnO Thin-film MEMS Acoustic Resonators

In this section, the frequency responses in the form of scattering parameters (S-parameters) of the fabricated resonators are measured directly using the on-wafer probing method by a Keysight 8753ES vector network analyzer. A Short-Open-Load-Thru (SOLT) full two-port calibration is firstly performed on a CS-5 calibration substrate (GGB Industries Inc.) to compensate for the loss from network analyzer ports, RF cables, and probes so that the measuring reference planes are shifted to the probe tips to ensure that the results are the actual frequency response of the resonators under test. The measurement results are grouped into specific topics in respect of design techniques and applications. In addition, the temperature and the power-dependent performance are also evaluated by measuring the temperature coefficient of frequency (TCF) and the frequency response under high power.

5.3.1 Aperture Size

In the-current-state-of-art SAW resonators and filter technologies, the design of the interdigital transducer (IDT) finger electrodes makes a great deal of impact in terms of frequency tuning and diffraction suppressions because the resonance responses are extremely sensitive to a subtle variation of the thin-film electrodes. Similarly, contour-mode acoustic resonators use the similar IDT pattern philosophy as the SAW does, so it is worthwhile exploiting how the SAW “black magics” turn out on contour-mode resonators.

Aperture size is generally defined as the length of the IDT finger electrodes, which sit on the top of the piezoelectric material. During the piezoelectric transduction, the transducers with higher IDT finger length can more effectively collect the electric charges from the piezoelectric layer, strengthening the detectable signal. Hence, the aperture size should be reasonably large to

avoid severe insertion loss and more considerable distortion due to the acoustic diffractions. However, the static capacitance generated between the IDT fingers is also proportional to the aperture size. A larger static capacitance results in a higher feedthrough noise level, which may negatively influence the signal-to-noise ratios for mass sensing functionalities and so on.

In Figure 5.3, two resonators are fabricated and measured to compare the impact made by varying the aperture sizes. As seen in Figure 5.3 (a) and (b), both resonators have five pairs of 13 μm -wide IDT fingers, which are 3 μm apart from each other. The IDT electrode aperture sizes are set at 320 μm and 160 μm , respectively. The resonators are suspended in the air and are held by a tether on each side. In Figure 5.3 (c), a comparison of resonance responses is depicted, where the blue curve and the red curve represent the resonators with the aperture size of 320 μm and 160 μm , respectively. It is clear to see the insertion loss is improved by 8.352 dB at 129 MHz, and the motional resistance is also reduced from 574 Ω to 208 Ω , with nearly no change in quality factor.

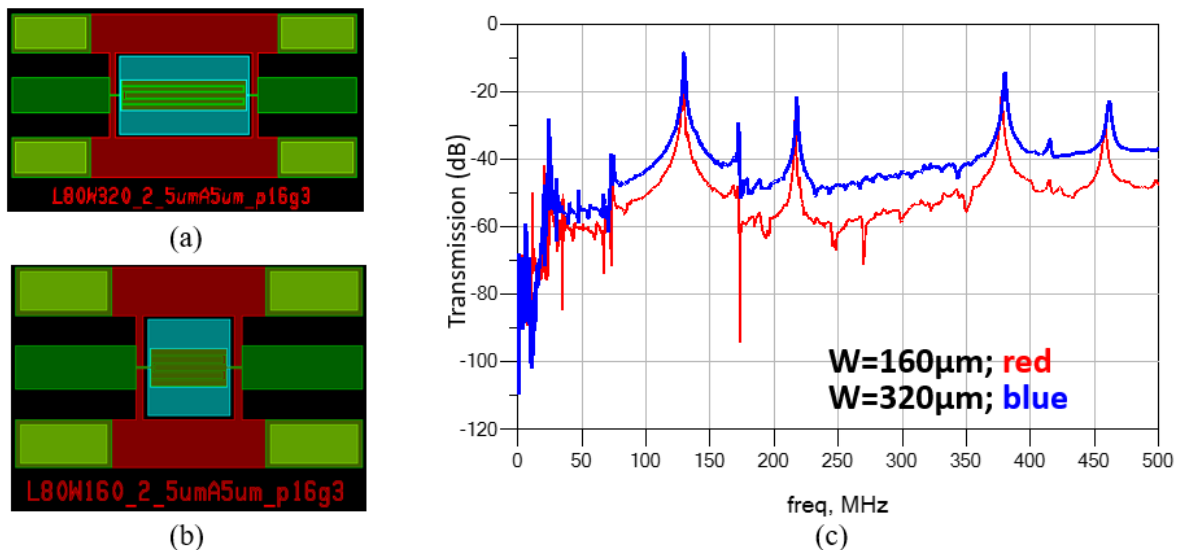


Figure 5.3 A comparison of the frequency response of the two resonators which are identically designed except for the aperture size. (a) A ZnO thin-film piezoelectric rectangular resonator built on a silicon wafer that has a body dimension of 320 μm x 80 μm , finger number of 5, finger pitch size of 16 μm , finger width of 13 μm and 1 pair of tethers; (b) a ZnO thin-film piezoelectric rectangular resonator with 50% shorter aperture size than that in (a); (c) the comparison of the frequency response of the two described resonators.

To confirm the observations from the previous demonstration. Another two resonators are brought into comparison to validate the statement in Figure 5.3. Both resonators have 22 pairs of IDT fingers, set at 2 μm wide and 2 μm apart. The pitch size is equal to 4 μm , which is four times smaller than that of the resonators in the previous example, so the resonance frequencies are expected to be higher. Similarly, the blue curve represents the resonator with an aperture size of 400 μm , and the red curve represents the resonator with an aperture size of 200 μm .

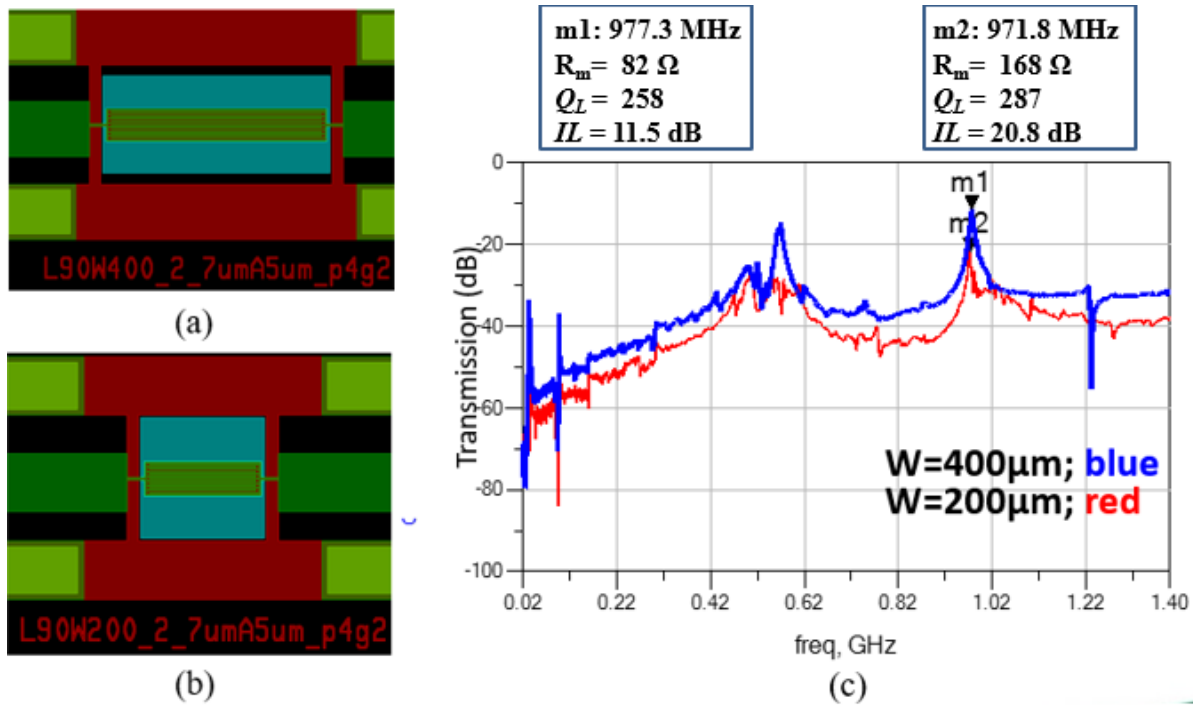


Figure 5.4 A comparison of the frequency response of the two resonators which are identically designed except for the aperture size. (a) A ZnO thin-film piezoelectric rectangular resonator built on a silicon wafer that has a body dimension of 400 μm x 90 μm , finger number of 22, finger pitch size of 4 μm , finger width of 2 μm and one pair of tethers; (b) a ZnO thin-film piezoelectric rectangular resonator with 50% shorter aperture size than that in (a); (c) the comparison of the frequency response of the two described resonators.

For the resonators with a smaller pitch size at 4 μm , the aperture size needs to be adequately long to excite the piezoelectric transduction, which is reflected by seeing the significant boost in both resonances around 570 MHz and 970 MHz. It is noticed that the capacitive feedthrough noise levels are elevated at high frequencies, and to obtain a good signal, the insertion loss must be small.

For example, As shown in Figure 5.4 (c), the insertion loss is reduced from 20.8 dB to 11.5 dB by extending the aperture size from 200 μm to 400 μm , and the motional resistance is also reduced by 50 %.

5.3.2 Finger-to-Gap Ratio (FGR) of Contour Mode Acoustic Resonators

As previously discussed in the earlier chapters, the resonance frequency depends on the pitch size and the utilized acoustic velocity. The pitch size is measured by the IDT finger electrode's width plus the distance between the adjacent electrodes. Theoretically, the piezoelectrically-transduced resonators should produce the same resonance frequencies if the pitch sizes are kept the same, but thicker and wider electrodes also tend to exhibit more loading effect, which may slightly shift the resonance frequencies down and the insertion loss up. From the simulation results presented in the last chapter, it is observed that the feedthrough noise levels are largely impacted by the finger-to-gap ratio of the top electrodes. A noticeable differentiation of insertion loss and static capacitance should also be expected.

In this section, four resonators with different FGRs are fabricated on silicon wafers and measured to support the FEM simulation results' observations. All four resonators have a body dimension of 320 μm \times 80 μm , finger number of 5, finger pitch size of 16 μm , and one pair of tethers. Ruthenium is selected as the IDT electrodes' material, and platinum is the material for the bottom electrode connected to the ground. The only difference is the finger-to-gap ratios listed in the following: 13:3, 11:5, 8:8, and 6:10, and the measured frequency responses of the resonators are depicted in Figure 5.5 (c) with their curves labeled in red, blue, pink, and blue representing the finger-to-gap configurations as seen in Figure 5.5 (a), (b), (c), (d), respectively. It is observed that the capacitive feedthrough levels get lower as the finger-to-gap ratios decreases. The resonance frequencies shift up by 13 -20 MHz when the finger-to-gap ratio drops.

Meanwhile, for the resonator with the 50% FGR, both signal strength and insertion loss are able to maintain at a decent level around 128 MHz and around 230 MHz, but the other higher resonance peaks are diminished. Another interesting observation is when the FGR is 6:10, labeled in green. There is a significant degradation in the resonance peak at 128 MHz and the resonance peaks above 300 MHz. However, the resonance peaks are much more strengthened at 230 MHz and 285 MHz, whereas the resonance peaks are found much weaker on the other resonators. Table 5.1 on the last page of this chapter summarizes the resonators' performance in the black circle in Figure 5.5.

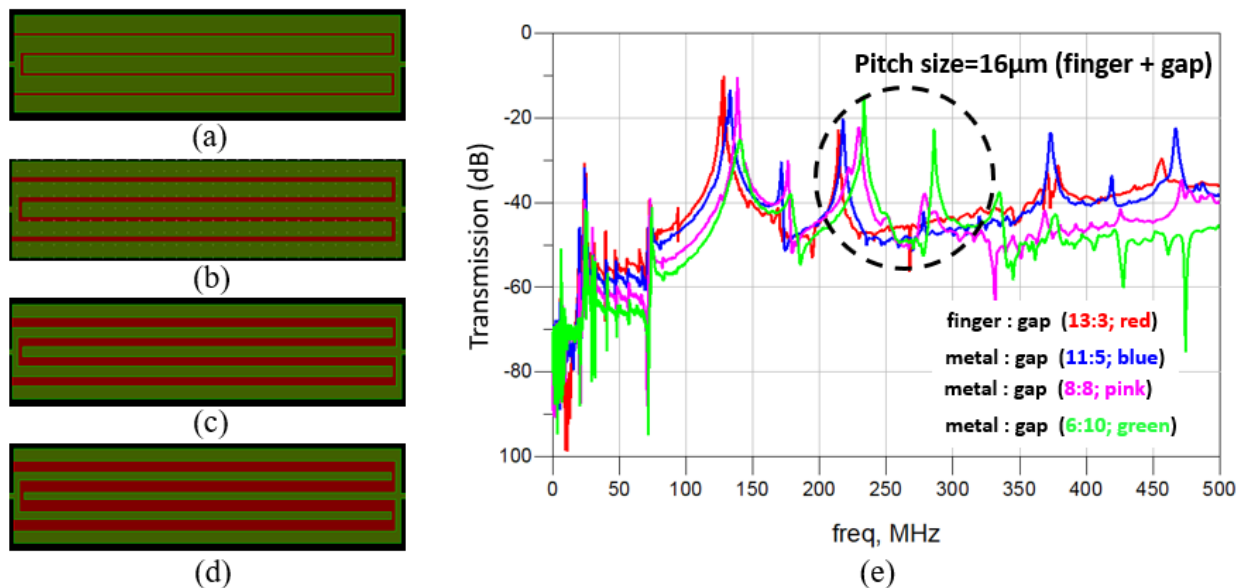


Figure 5.5 A comparison of the frequency response of four resonators based on a silicon wafer. Each having a body dimension of $320\ \mu\text{m} \times 80\text{-}\mu\text{m}$, 5 IDT fingers with the pitch size of $16\ \mu\text{m}$, held 1 pair of tethers: (a) the resonator with FGR: 16:3; (b) the resonator with FGR: 11:5; (c) the resonator with FGR: 8:8; (d) the resonator with FGR: 6:10; (e) the comparison of the measured frequency response of the four described resonators (a)-(d).

5.3.3 Bottom Electrode Configurations

Besides the various design techniques regarding the IDT fingers on the top electrodes, different bottom electrode configurations are also investigated. There is a prior research focused on this concern reported by other groups in recent years. Unlike that in SAW, the bottom electrodes

on a contour-mode resonator significantly impact the capacitance between the two electrodes sandwiching the piezoelectric layer and may cause a change in acoustic velocities for specific modes [44][45]. The static capacitance is altered in the BVD circuit model when the bottom electrodes are grounded through the via holes, as shown in Figure 5.6.

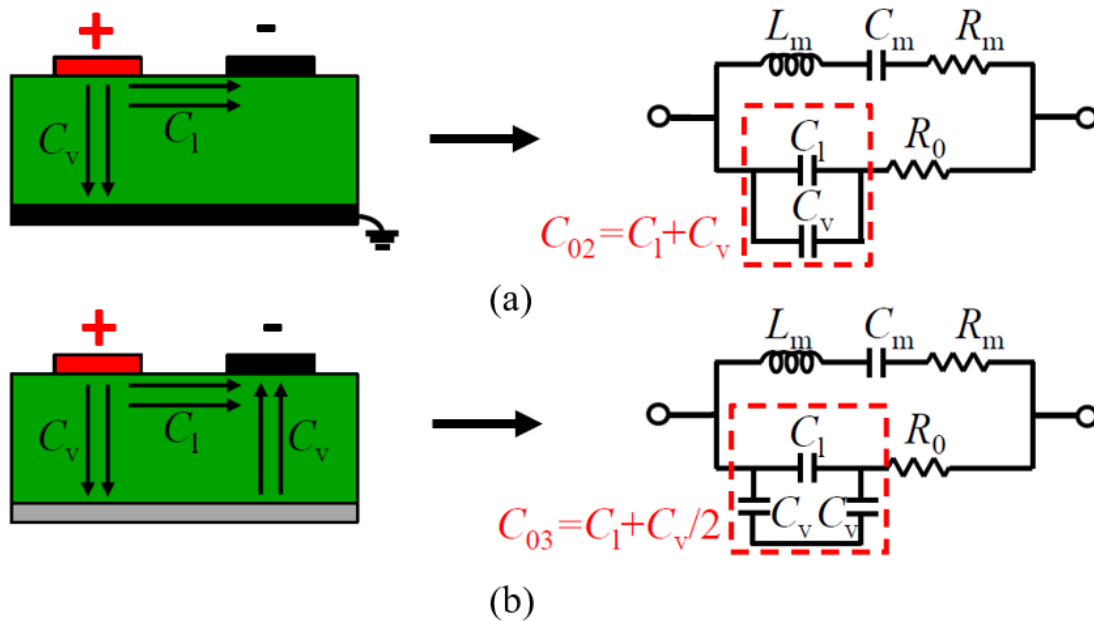


Figure 5.6 Equivalent static capacitances in the BVD circuit models for the two-port contour-mode resonators under different bottom electrodes conditions: (a) grounded-bottom electrodes; (b) floating bottom electrodes.

As illustrated in Figure 5.7 (a)-(c), the first design is for the resonator with the bottom electrodes grounded, and the second configuration is to adopt floating bottom electrodes when the via holes are disabled so that the electrical connection is cut out between the top and bottom electrodes. The third configuration is to employ grounded IDT-patterned bottom electrode fingers that are aligned to the gap of the top IDT fingers to create top/bottom IDT electrode offset.

Figure 5.7 (d) depicts the measured frequency responses of the resonators using the above three bottom electrode configurations. It is easily observed that the feedthrough noise levels are significantly influenced by the grounded bottom electrodes that increase the static capacitance. To compare the device designs with the grounded bottom electrodes and the floating bottom electrode

configurations, the resonance frequencies are found to be consistent, but the capacitive feedthrough noise level turns out to be higher for the floating bottom electrodes as expected, especially when the frequency is below 500 MHz. The measured frequency characteristics labeled in green represent the IDT-type configuration. The resonance peaks shift to higher because the equivalent pitch size is shortened by aligning the bottom IDT fingers to the top IDT electrodes' gap. A smaller pitch size IDT can generate completely different vibration modes that can lead to higher resonance frequencies. Meanwhile, due to the IDT misalignment of the top and the bottom IDT, the resulted capacitance is smaller due to the cancellation effect.

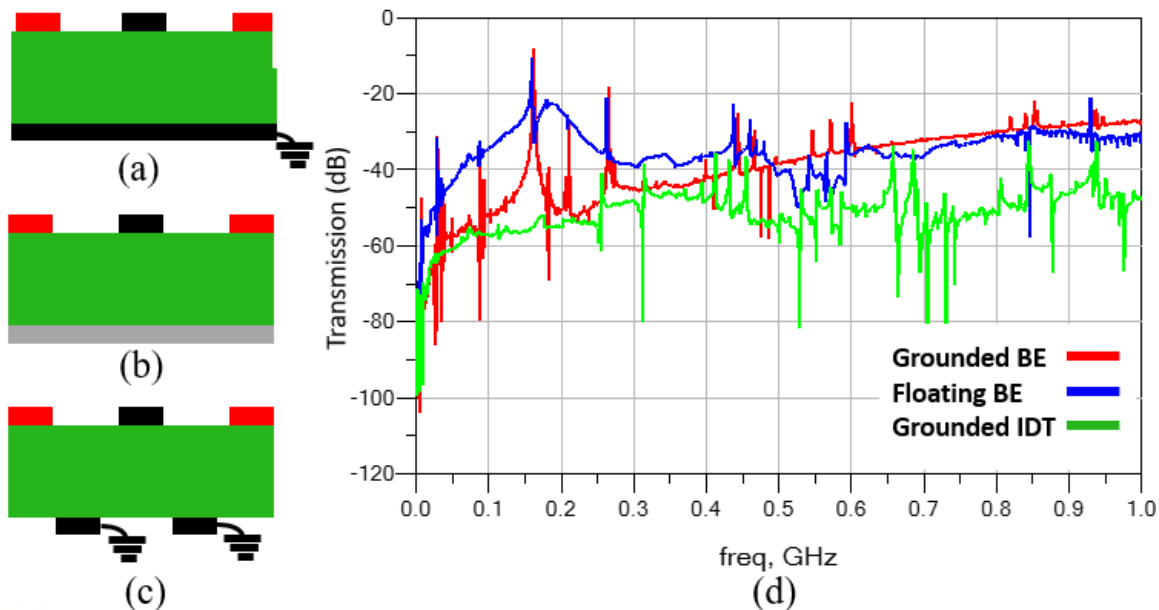


Figure 5.7 The measured frequency response of the two-port contour-mode resonators with different bottom electrode configurations: (a) grounded bottom electrodes (labeled in red); (b) floating bottom electrodes (labeled in blue); (c) grounded IDT bottom electrodes (labeled in green).

5.3.4 Design Techniques of Tethers

Unlike the BAW having a very robust mechanical frame linkage that holds the suspended resonator body, a contour-mode resonator's performance is very sensitive to the dimensions, and the number of the tethers as the tethers are used to holding the resonator body in the air while

connecting it to the substrate. Therefore, a good amount of stress may be likely to fall on tethers, resulting in energy loss. Not only serving as the mechanical linkage, but tethers are also used to conduct electrical signals at the input and the output terminals over a wide range of frequencies. Consequently, in this section, the two-port contour-mode resonators are designed and fabricated to address these concerns by varying the width, the length, and the quantity of the tethers.

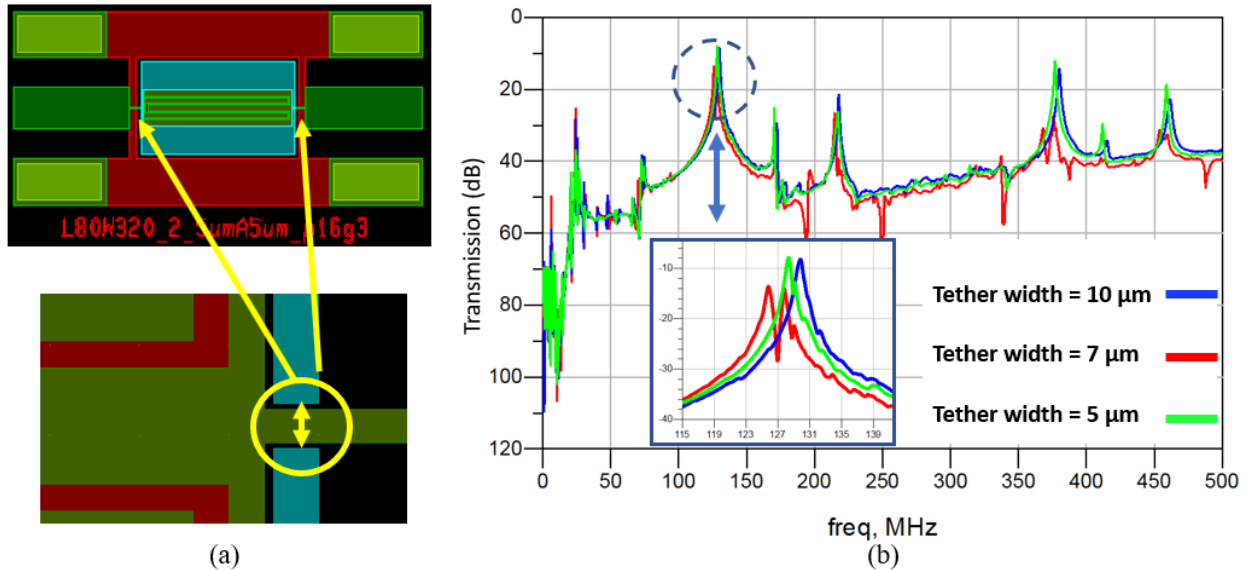


Figure 5.8 The measured frequency responses of the two-port contour-mode resonators with the tether width of 10 μm (labeled in blue), 7 μm (marked in red), and 5 μm (labeled in green).

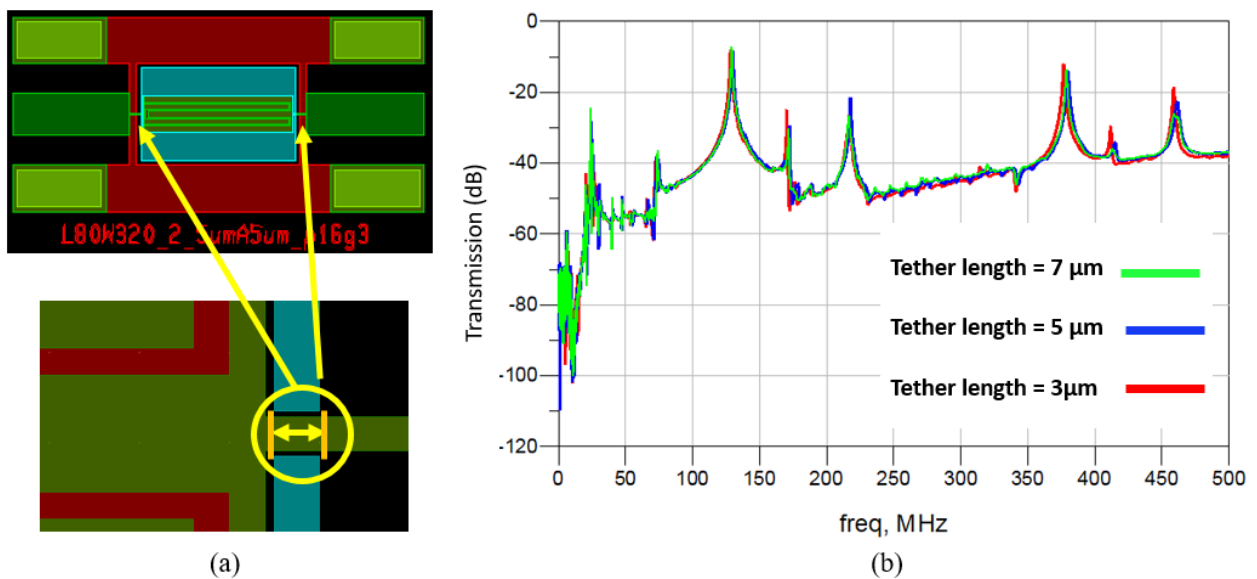


Figure 5.9 The measured frequency responses of the two-port contour-mode resonators with the tether length of 7 μm (labeled in green), 5 μm (marked in blue), and 3 μm (labeled in red).

The measured resonators have an identical body dimension of 320 μm x 80 μm , finger number of 5, finger pitch size of 16 μm , and one pair of tethers. And the only difference lies in the length of the tethers. As shown in Figure 5.8, the tether widths are varied to 10 μm , 7 μm , and 5 μm , and the highest Q is found when the tether width is set at 5 μm . Similarly, the tether's length is also varied to 7 μm , 5 μm , and 3 μm . As shown in Figure 5.9, a very minimal change in the frequency responses is found, which indicates the small range of variation in tether length does not significantly impact the resonator's performance.

The last degree of freedom in tether configurations is by changing the number of tethers. Since most of the stress is concentrated at the tethers, it is reasonable to believe that the number of tethers can make a difference in the insertion loss and the resonance quality factors.

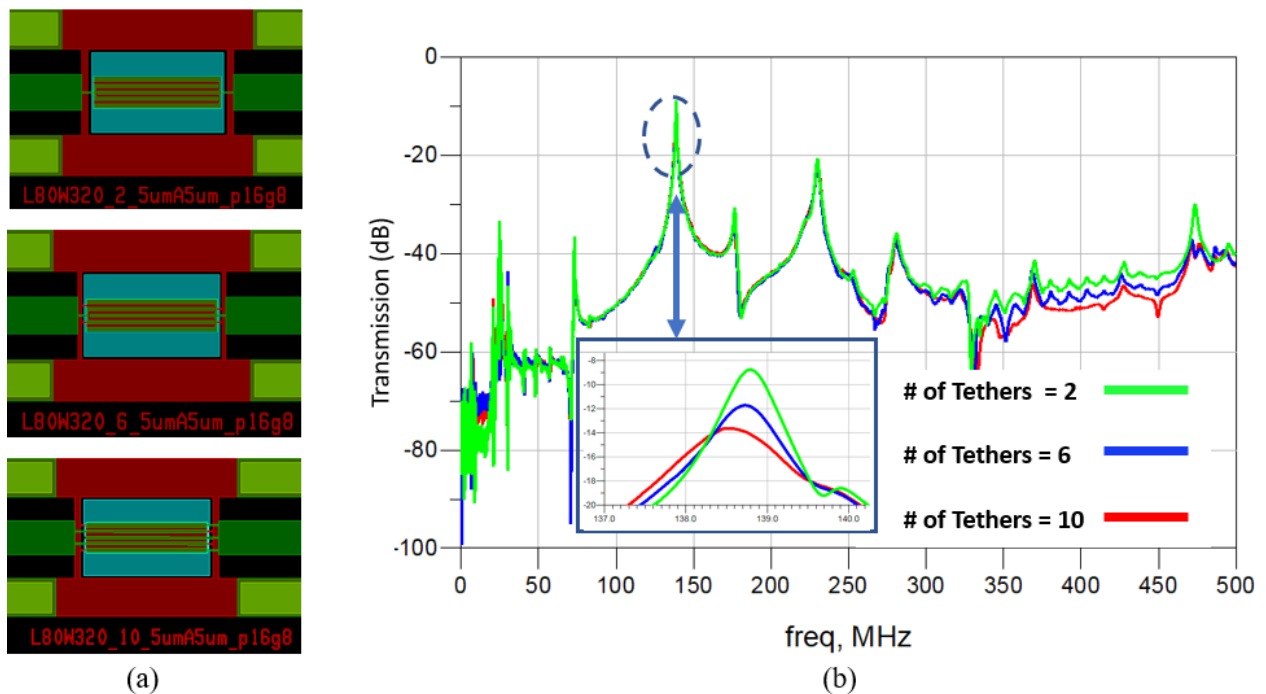


Figure 5.10 The measured frequency responses of the two-port contour-mode resonators with a different number of tethers: 2 tethers (labeled in green), 6 tethers (labeled in blue), and 10 tethers (labeled in red).

In Figure 5.10, the frequency responses of the resonators with the different number of tethers are displayed. The overall resonance responses seem to be very similar over a broader span. However, suppose one looks closer into the resonance peak around 138 MHz. In that case, it is found that both the insertion loss and the quality factors can deteriorate as the number of tether increases. In essence, the insertion loss increases by 3 dB and 5 dB, and the quality factor drops by 60% and 80% when the number of the tether is increased to 6 and 10 from 2, respectively.

5.4 Design Techniques for Quality Factor Improvements and Measurement Results

In the previous sections, a comprehensive study is performed to investigate the different design configurations of the important dimension parameters on a two-port piezoelectric contour-mode acoustic resonator. The presented results are measured and concluded consistently across the multiple dies on the multiple wafer samples, serving as a trusty design guide for the other researchers and designers working on similar technology. In this section, the measurement results are presented to support an investigation of the advantages and disadvantages of different design techniques for quality factor improvement.

As discussed in the previous chapters, the capacitive resonators generally tend to exhibit an extremely high quality factor (Q) but also experiencing a core weakness: a very high motional resistance (R_m). Meanwhile, the capacitive resonators are not considered a “serious” passive device because they need to operate with a bias voltage as an amplifier does. Unlike the capacitive resonators, the piezoelectrically-transduced resonators usually feature a reasonably high frequency with a much smaller R_m , and they are truly “passive”, but the relatively low quality factors can be problematic for specific applications. For example, SAW resonators may struggle with low Q at a frequency higher than 2.5 GHz.

As known, the quality factor is the ratio of the energy stored divided by the energy dissipated per cycle expressed as:

$$Q = 2\pi \times \frac{E_{stored}}{E_{dissipated}} \quad (5.1)$$

It is clear that the magnitude of the quality factor is inversely proportional to the amount of energy dissipated, which is caused by various loss mechanisms relevant to the resonator. The possible sources causing the energy dissipations are well summarized [46], the overall quality factor can be explained and estimated using the following equation:

$$\frac{1}{Q_{total}} = \frac{1}{Q_{tether}} + \frac{1}{Q_{interface}} + \frac{1}{Q_{damping}} + \frac{1}{Q_{material}} + \frac{1}{Q_{other}} \quad (5.2)$$

The interface loss, $Q_{interface}$, is usually related to the delamination and interfacial stress located at the surface of the deposited material, which is caused mainly by the flawed deposition process. The damping loss, $Q_{damping}$, comes from the energy dissipations during thousands of vibrations that lead to a temperature gradient due to a strain gradient. The damping loss can worsen when the resonator is vibrating in the air where the air's viscosity cannot be neglected. This is why very high-quality vacuum packaging is needed to minimize the loss due to the air viscous damping. The material loss, $Q_{material}$, is a complicated combination of different loss factors including, phonon-to-phonon scattering loss, dielectric loss, and so forth. The material loss tends to be low on a hard, non-conductive crystalline material, such as quartz, sapphire, and diamond. The tether loss (also known as anchor related loss), Q_{tether} , is a major energy loss source to a free-standing piezoelectric resonator, especially at low-frequency ranges. Most of the strain and stress are concentrated at the tether, and this is where the acoustic energy is leaked to the substrate. In this section, the material loss and the tether loss are the two mechanisms to be tackled in order to improve the quality factor.

5.4.1 Approach #1: Using Diamond Substrates

Natural diamond offers a variety of superior properties, such as Young's modulus (about eight times higher than that of silicon), resulting in high acoustic velocity that equals the square root of Young's modulus over the density. The extremely high Young's modulus makes diamond an excellent material for energy storage in resonator designs.

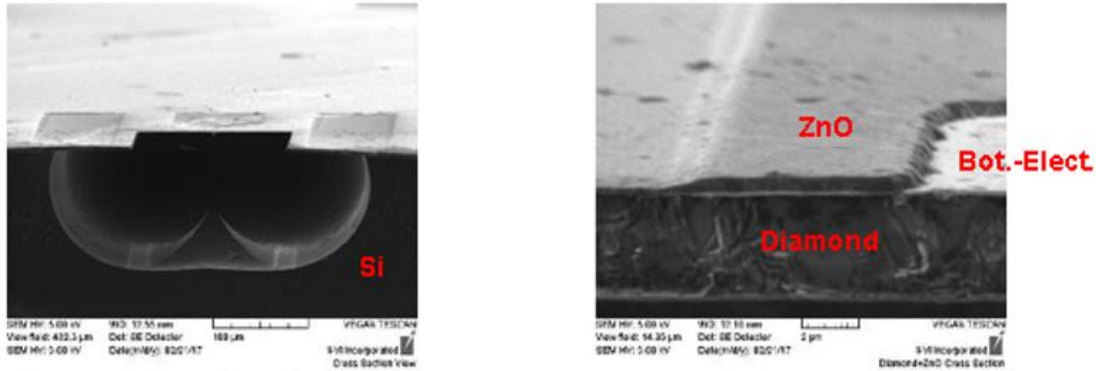


Figure 5.11 (a) A cross-sectional-view SEM photograph of a ZnO thin-film piezoelectric disk resonator on a diamond-coated silicon wafer; (b) a zoom-in view of the resonator structural body layers.

As illustrated in Figure 5.11 (a), the resonator structure is free-standing in the air by dry etching the silicon material underneath. As shown in Figure 5.11 (b), a layer of diamond thin film is added to the resonator structure under the bottom electrodes. Together with the ZnO, the resonator structural body becomes more robust, and less loss should be dissipated, thus resulting in much higher Q and resonance frequencies simultaneously.

For a direct comparison, the thin-film ZnO piezoelectric disk resonators are fabricated on a silicon wafer and a diamond-coated silicon wafer. Two different radiuses have been included in the design: 30 μm and 50 μm , as shown in Figure 5.12 (a).

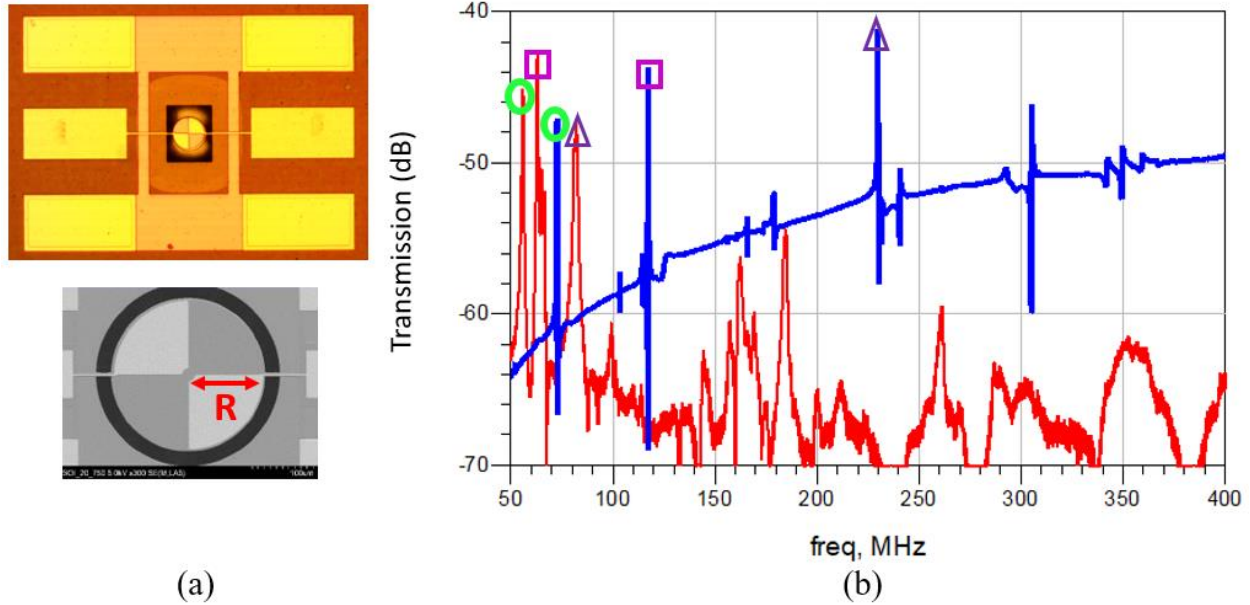


Figure 5.12 (a) A photograph of the ZnO thin-film piezoelectric disk resonators with different radius; (b) a comparison of the frequency responses of the piezoelectric disk resonators on different substrates (blue: on a diamond-coated wafer; red: on a silicon wafer).

The frequency response plotted in Figure 5.12 (b) depicts the resonance for a two-tether 30 μm -radius disk resonator. The fundamental wine-glass mode of the disk resonator built on the diamond-coated wafer is located at 72.67 MHz as compared to the one at 55.82 MHz on the silicon wafer. The loaded Q is measured at 3,892 on the diamond-coated wafer, which is more than ten times higher than that of the resonator built on the silicon wafer. In the radial contour mode, the Q measured on the diamond-coated wafer is 4,215, which is also more than ten times higher than the silicon counterpart. Similar results and observations were also found for the disk resonator with a radius of 50 μm .

5.4.2 Approach #2: Phononic Crystal Tethers

Another effective way to improve the resonator's quality factor is to reduce tether loss. As presented in the earlier sections, a narrower tether placed at the nodal locations of the resonance mode can reduce the loss. Also, designing the tether length with an odd multiple of a quarter-wave

may help confine the acoustic loss at tether [47], but it is difficult to implement in the actual design because the wavelength varied from the material to material.

Besides varying the dimension of the tether, the shape of the tethers can also be tailored to reduce the energy loss and enhance Q . Phononic crystals (PC) are designed in unique shapes and are implemented on tethers to eliminate vibration and prevent acoustic wave propagation through the tethers attached to the hosting substrate [48]-[52]. In this section, three different shapes of phononic crystals are compared.

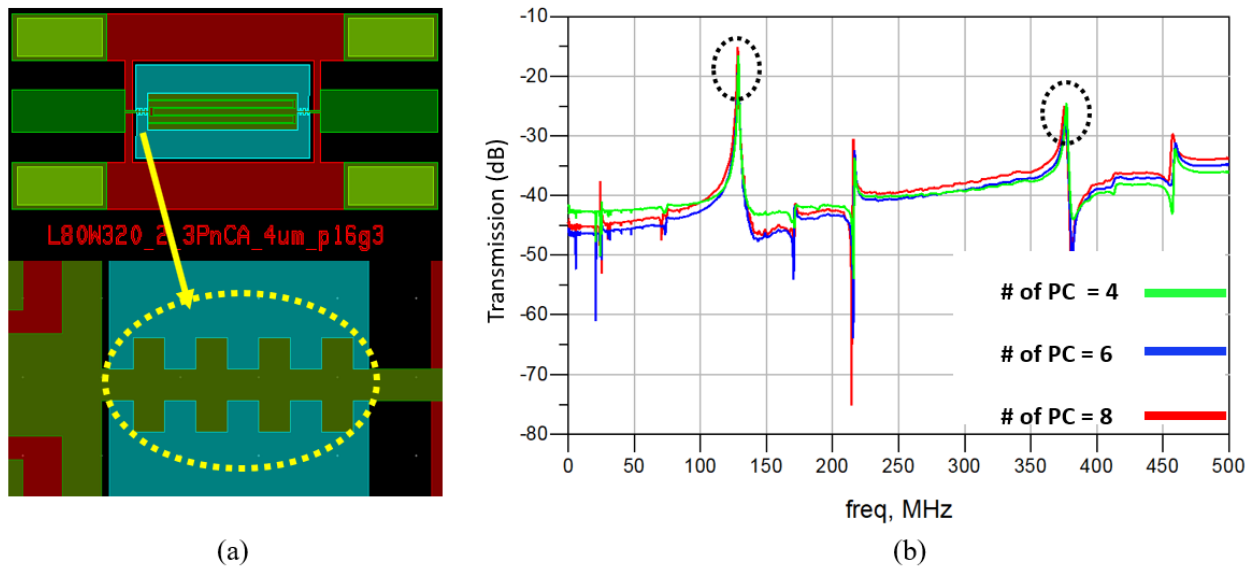


Figure 5.13 (a) A mask view example of a ZnO thin-film piezoelectric contour-mode resonators with 4 cross-shaped phononic crystals on the tethers; (b) a comparison of the frequency response of the resonators with different numbers of cross-shaped phononic crystals on the tethers.

As shown in Figure 5.13 (a), an example of the mask view illustrates that four cross-shaped PC are used at each side of the resonator, and a comparison of the measured frequency responses are depicted in Figure 5.13 (b). Figure 14 (a) and (b) provide zoomed-in views of the two major resonance peaks circled in Figure 5.13 (b). It is obvious the highest quality factor is achieved when 4 PC are placed in the tethers as compared to the original tether design without PC, the quality factor is improved by nearly 50%.

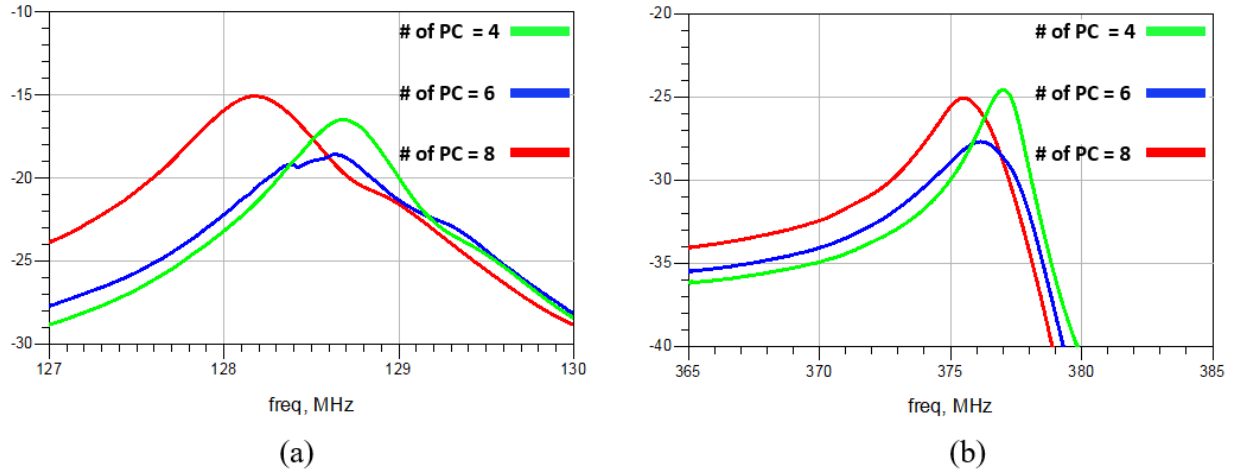


Figure 5.14 the zoomed-in views of the two circled peaks in Figure 5.13 (b).

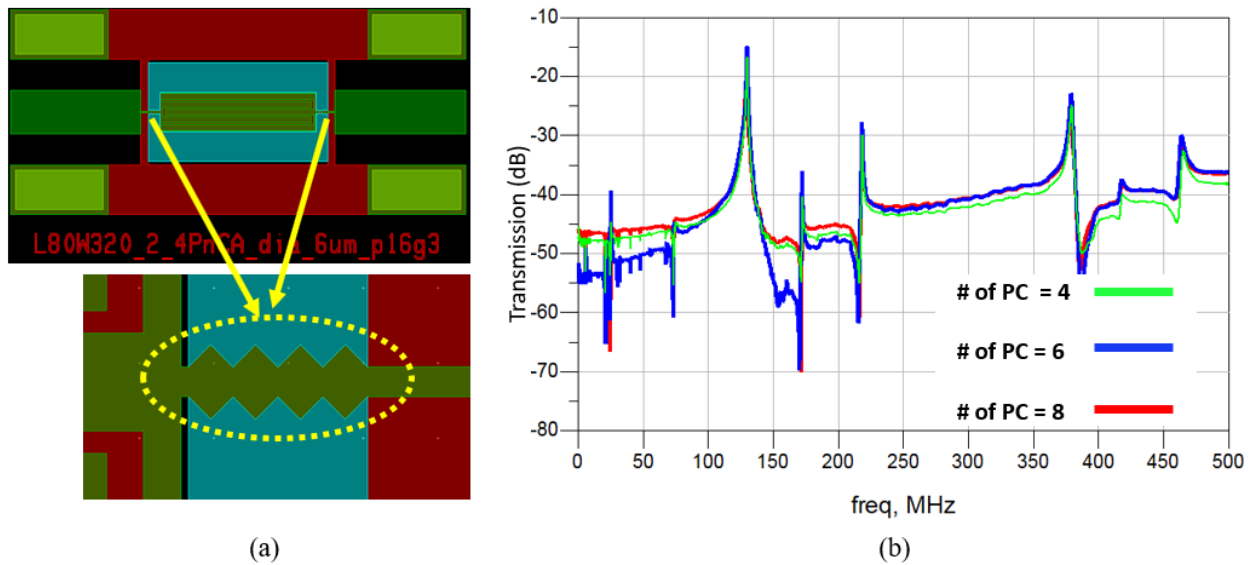


Figure 5.15 (a) A mask view example of a ZnO thin-film piezoelectric contour-mode resonators with 4 diamond-shaped phononic crystals on the tethers; (b) a comparison of the frequency responses of the resonators with different numbers of diamond-shaped phononic crystals on the tethers.

Similarly, diamond-shaped phononic crystals have also been implemented to tethers on other resonators. In Figure 5.15 (b) above, the measured frequency responses of three resonators with different numbers of diamond-shaped PC are presented, and the best performance is captured when the number of the PC equal to 6 in terms of quality factor and insertion loss, but the spurious modes are effectively suppressed below 100 MHz when 8 PCs are employed.

The following configuration consists of triangle-shaped PCs pointing in opposite directions, as displayed in Figure 5.16 (a) and (b), and the measured frequency responses exhibit different characteristics even when the number of the triangle-shaped PC's are kept to 4, as shown in Figure 5.16 (c).

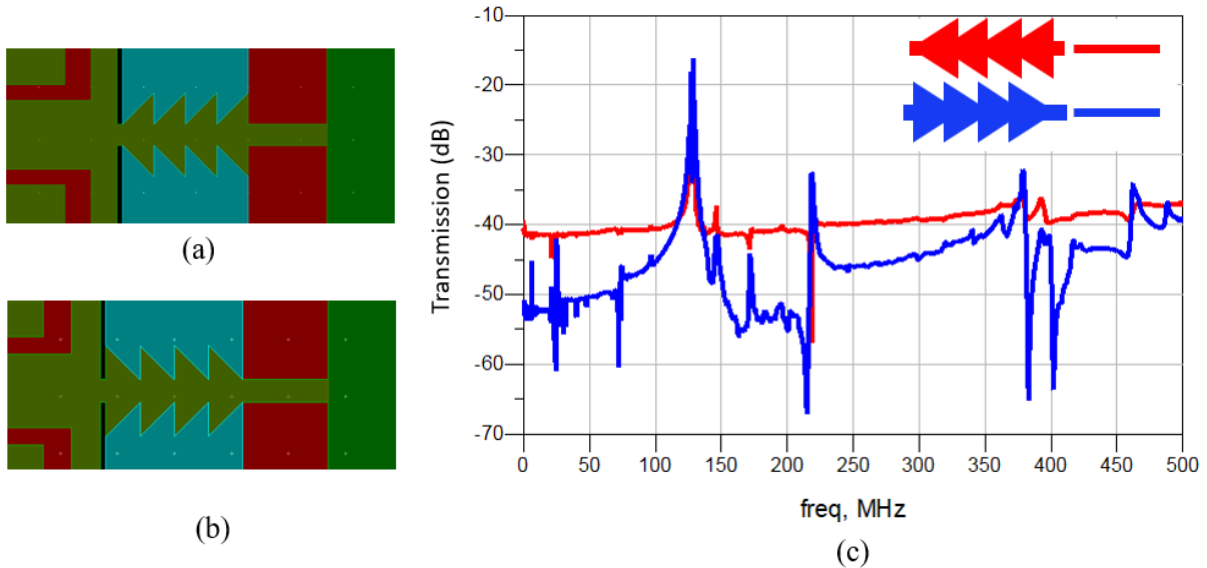


Figure 5.16 (a) A mask view example of a ZnO thin-film piezoelectric contour-mode resonators with 4 triangle-shaped phononic crystals on the tethers; (b) A mask view example of a ZnO thin-film piezoelectric contour-mode resonators with 4 triangle-shaped phononic crystals on the tethers pointing in the opposite direction; (c) a comparison of the frequency responses of the resonators with different numbers of triangle-shaped phononic crystals on the tethers.

To summarize the advantages and the disadvantages of the phononic crystals in the different shapes, Figure 5.17 compares the measurement results of the resonators on the same die. It is clear that all three types of phononic crystals work effectively in terms of spurious mode suppression at lower frequencies, and all the resonators with PC designs on the tethers are capable of boosting the quality factor by 30%-50%, but the cross-shaped PCs tend to have more static capacitance, which leads to a higher feedthrough noise level. With all the performance considered, the triangle-shaped phononic crystals seem to be the best PC design choice.

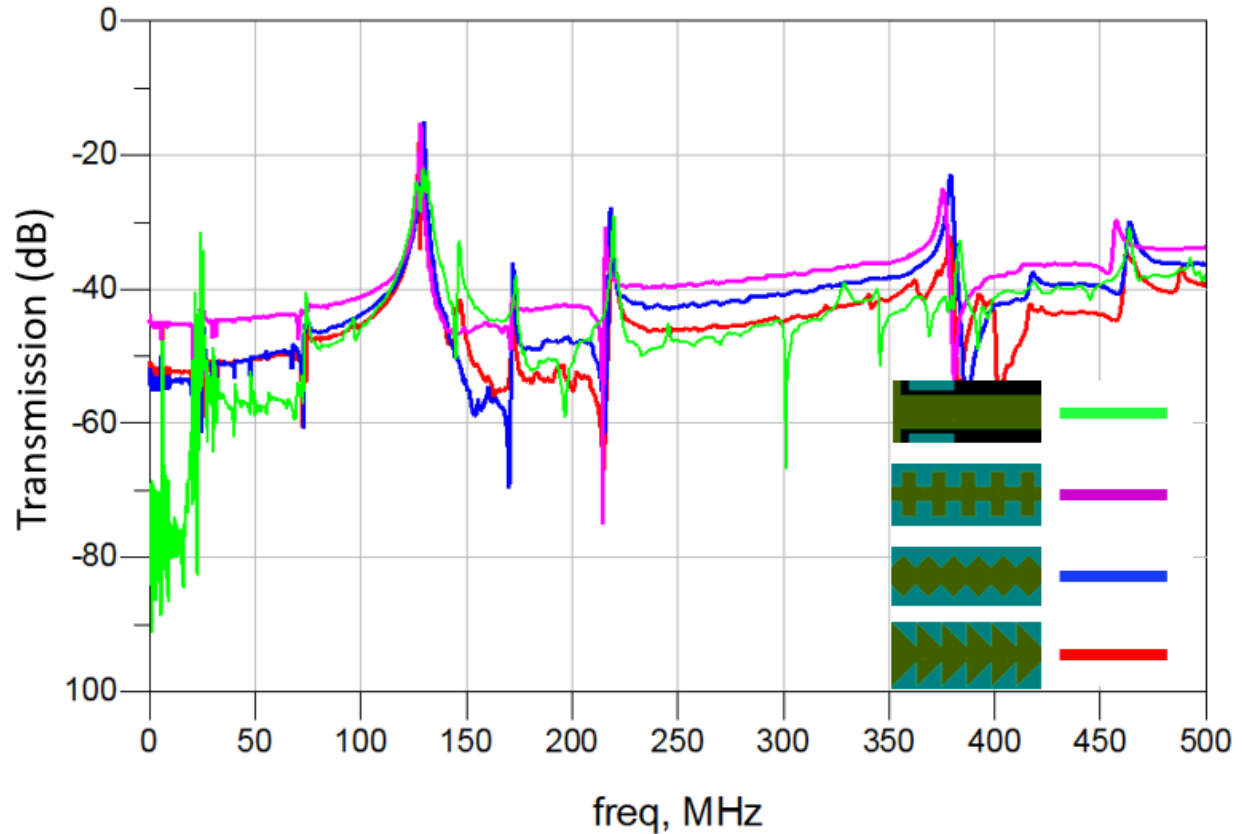


Figure 5.17 A comparison of the frequency response of the resonators with six phononic crystals in different shapes on the tethers (labeled in purple, blue, and red) against the original tether (labeled in green).

5.4.3 Other Q Improvement Approaches

Previous literature studies imply another design approach for quality factor enhancement can be achieved by introducing a non-rectangular-shaped resonator. For example, with a certain degree of curvature at the upper and lower edge of the resonator structure body, the quality factors can be significantly improved at resonance frequencies. However, curved edges can also generate a great amount of unwanted spurious modes due to the uncontrollable acoustic wave reflections [54]-[56], the electromechanical coupling coefficient is drastically reduced if the curvature exceeds a certain limit in respect to the wavelength [57]. In this dissertation, the measured results using the similar Q enhancement method show inconsistencies across the wafer, so it needs to be further validated.

5.5 Temperature Linearity of Temperatures

The temperature coefficient of frequency (TC_f) is commonly used to describe the temperature stability that is the frequency shift in response to the temperature variation. The temperature coefficient generally refers to the fractional slope of a linear fit to that quantity as a function of temperature, and divided by the specific resonance frequency, TC_f can be directly measured and used to calculate the frequency shift with specific temperature given.

The intrinsic TC_f of a resonator with stacked layers depends on the mechanical properties of the multiple materials, and a general formula with a unit of ppm per degree Celsius can be expressed as [58][59]:

$$TC_f = \frac{1}{f_o} \frac{\partial f}{\partial T} = -\frac{1}{\alpha} \frac{\partial \alpha}{\partial T} + \frac{1}{2} \frac{1}{E_p} \frac{\partial E_p}{\partial T} - \frac{1}{2} \frac{1}{\rho} \frac{\partial \rho}{\partial T} = -\alpha_p + \frac{1}{2} TC_E \quad (5.3)$$

where α is the fundamental geometrical parameter that sets the device resonance frequency, T is the temperature of operation, α_p is the thermal expansion coefficient of the stacked materials in the device layer, and TC_E is the temperature coefficient of Young's modulus of stacked layers in the resonators [60] [61].

Equation 5.3 can be extended and utilized for a thin-film piezoelectric acoustic resonator with multiple layers, including the electrodes and functional piezoelectric layer. By assuming all the layers have the same surface area, the temperature coefficient of frequency can be then written as:

$$TC_f = \sqrt{\frac{(1 + TC_{E1})E_1 t_1 + (1 + TC_{E2})E_2 t_2 + \dots}{E_1 t_1 + E_2 t_2 + \dots}} - 1 \quad (5.4)$$

where E and t are Young's modulus and thickness of each layer, respectively. Before introducing the temperature compensation techniques of acoustic resonators, it is important to understand what

causes the resonance frequency change under different temperatures. For the resonators with IDT finger patterns, the temperature coefficient of frequency is generally caused by two reasons: thermal expansion and elastic relaxation, quantified by two fundamental parameters. The first one is the coefficient of thermal expansion (CT_E), which is usually a positive number referring to the amount of material expansion due to heat. For a SAW resonator or a contour-mode resonator, when the device's substrate heats up and expands, the IDT fingers spread apart, thus lowering the resonance frequency of the device.

The second fundamental parameter determining the TC_f is called the temperature coefficient of velocity (TC_V) due to elastic relaxation. It is known that as most materials heat up, they tend to become softer. This reduces Young's modulus (stiffness) results in a slower acoustic wave velocity. A slower velocity means it takes more time for the acoustic wave to travel between the IDT fingers, thus lowering the resonance frequency of the device. For most materials, the TC_V is usually a negative number, quantifying how much the acoustic velocity is reduced as the temperature increases.

Combined the above two parameters, the temperature coefficient of frequency of a piezoelectric acoustic resonator can be presented as:

$$TC_f = TC_V - CT_E \quad (5.5)$$

It is noted that the CT_E does not apply to the TC_f of a BAW device because no IDT fingers are employed, and the resonance frequency is the acoustic velocity and the vertical thicknesses of the multiple stack layers.

The temperature compensation techniques have been well studied and used to stabilize the device's performance over a wide range of temperatures. For example, in many CMOS and SOI technologies, the temperature sensitivity of frequency can be improved by having a highly doped

Si in the stacked resonator structural layer [62]. For piezoelectric acoustic resonators, the temperature compensation techniques are mostly concentrated on overcoming the two fundamental parameters in Equation 5.5. Figure 5.14 (a) shows the first commonly-used approach to compensating the TC_V is called thin-film overlay technique. This is achieved by depositing materials with opposite thermal behavior onto the device surface. The most standard technique is to bury electrodes inside a silicon oxide overlay (SiO_2) because SiO_2 has a positive TC_V and gets harder as heated up [63]-[66]. By confining some of the acoustic energy in the positive TC_V material, it is possible to achieve a net-zero TC_f on an acoustic resonator. Although the resonator can be extremely stable with a near-zero TC_f , less of the total acoustic energy is confined to the piezoelectric layer, so the quality factor and the coupling factors can be degraded unless a higher coupling material is used.



Figure 5.18 Temperature compensation techniques used in piezoelectric acoustic resonators: (a) thin film overlay; (b) thermal expansion constraint.

Figure 5.14 (b) depicts another temperature compensation technique: thermal expansion constraint, achieved by depositing or bonding low thermal expansion material to the existing resonator structural body. The typical material has a very large Young's modulus, such as sapphire, quartz, and diamond [67]-[69]. The best achievable TC_f is between -10 to -30 ppm/ $^{\circ}C$.

Two identically-designed resonators are picked for a direct comparison, and TC_f are measured with a test setup including a VNA, a temperature controller, and a probe station with a

heated chuck. Both resonators have a body dimension of $320 \mu\text{m} \times 80 \mu\text{m}$, 5 IDT fingers with the pitch size of $16 \mu\text{m}$ (finger-to-gap ratio 13:3), equipped with one pair of tethers. As depicted in Figure 5.19 (a), the two-port frequency response of the resonator on the silicon wafer was measured over a range of temperatures from $20 \text{ }^\circ\text{C}$ to $100 \text{ }^\circ\text{C}$. Figure 5.15 (b) displays the frequency change versus temperature, and a linear behavior is easily captured. The TC_f of the ZnO piezoelectric thin-film resonator on the silicon wafer turn out to be $-51.86 \text{ ppm}/^\circ\text{C}$ from the calculation of the slope of the dashed line divided by the resonance frequency at room temperature. The measured TC_f is a slightly higher than a typical SAW device with IDT fingers, as the heat dissipation is slower because the resonator is free-standing in the air.

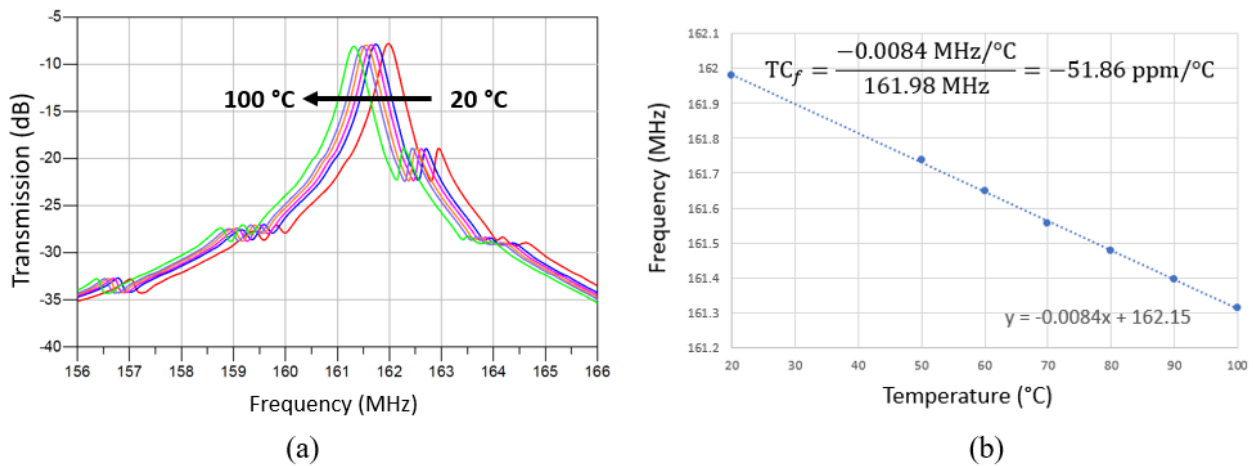


Figure 5.19 (a) Measured frequency response of the resonator built on a silicon wafer over a temperature range from 20 to 100°C ; (b) measured resonance frequencies over temperature.

The resonator fabricated on the diamond-coated silicon wafer, the measured resonance responses are shown in Figure 5.20 (a). It is clear to see that the frequency change is much smaller as compared to the silicon counterpart. The resonance frequency over the different temperatures also indicate a clear linear behavior, and the slope was measured at -0.0024 . After the calculation, the TC_f of the same device on the diamond-coated wafer is calculated to be $-14.05 \text{ ppm}/^\circ\text{C}$, which

is 37.81 ppm/°C better than the device built on the silicon wafer. It is obvious that the TC_f of the resonator can be significantly improved by employing the thin film diamond structural layer.

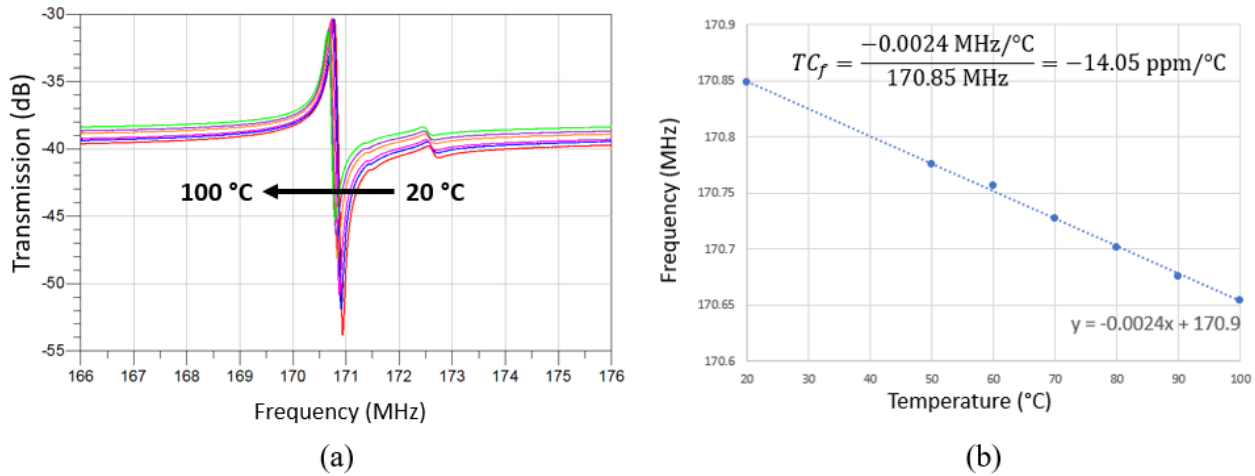


Figure 5.20 (a) Measured frequency response of the resonator built on a diamond-coated wafer over a temperature range from 20 to 100°C; (b) measured resonance frequencies over temperature.

5.6 Power-Handling Capability

Amongst a few key performances of RF filters based on piezoelectric acoustic resonators, the power handling capability has become an increasingly crucial concern, especially by today's long-term evolution (LTE) and 5G standards that require higher power for more data transfer rates. The power handling capability is anticipated to be quite different in the commercial BAW and SAW devices as the SAW resonators are more vulnerable to the high power because the closely-positioned IDT fingers tend to fail due to the acousto-migrations[70][71]. Similar to the more familiar the electro-migrations often seen in high-current situations, acousto-migrations are caused by physical "earthquake-motion" shakings of the structures synchronized with the acoustic wave motion [72], resulting in the electrode delaminations in forms of voids, fuzzy hillocks, and branches. Consequently, the adjacent IDT fingers may be shorted, or the electrical resistivity is dramatically increased, causing degradations in the overall performance. Meanwhile, a higher input power produces a more increased current flow through the multiple inter-connected

resonators in a SAW filter, and the uneven current densities at different resonators are dedicated to skewed temperature distributions, causing unwanted operation frequency shifts. A commonly-used strategy to address this issue is done by splitting the specific resonator at the hotter spot into multiple smaller resonators that work equivalently but with smaller current densities.

For BAW resonators, the self-heating is also the leading cause and failure mechanism that limits the maximum operation power [73]. The raised temperature over a particular area of a BAW device is triggered by the energy losses, which is the primary cause that tend to lower the resonance frequency, and the coupling between temperature and impedance has a nonlinear correlation. Amongst a few critical differences in terms of performance metrics, the power handling ability is anticipated to be quite different as FBAR resonators are fully suspended over a released air cavity, whereas the solidly mounted (unreleased) resonators are only separated from the substrate by a stack of Bragg reflector layers. The substrate can act as the heat sink for the BAW devices. For FBAR suspended over an air cavity, the air is not a good “thermally conductive” material for heat dissipation. SMR-BAW is standing on a solid materials stack as the Bragg reflector, which provides better heat dissipation. The silicon wafer provides outstanding properties such as low acoustic losses as well as mechanical and chemical stability [74]. The thermal conductivity of the chemical vapor deposited diamond is 1000-2000 W/mk that is about 10 times higher than that of the silicon substrate (135-150 W/mk) [75]. Therefore, the heat-dissipating ability of the diamond film is superior to that of a silicon substrate.

As discussed, the power handling evaluations have been primarily conducted at a filter level, which combines multiple pairs of series and shunt resonators. A continuous high-power signal (e.g., 30 dBm) is usually applied at the upper passband edge of the TX filter for a certain period to meet a certain power handling requirement standard. There are very few examples of

performing the power handling test on a single resonator from the literature study. Plus, most of the high-power measurements are based on the single-frequency multiple power non-destructive testing, the tested devices are usually irreversible and burned. Furthermore, the frequency response measurements under high power have hardly been investigated due to the complexity of the measurement setups and integrations.

In this section, the described issues are successfully addressed by introducing the two-port high-power measurement setup with a de-embedding system for data post-processing. Similar to comparing the temperature dependency of the piezoelectric contour-mode resonators fabricated on the different wafers, the power handling capabilities are also examined and compared. For the routine on-wafer probing measurement, 0 dBm is usually selected to be the device's incident power. Although this power can be adjusted internally on the vector network analyzer (VNA) over a wide range (-40 dBm to +10 dBm), the measured results are automatically compensated regardless of what power is applied. Therefore, for the best interest, it makes more sense to capture the power at the end of the input cable using a power meter in order to verify what the genuine power level is at the input. Moreover, to further extend the input power level, a power amplifier (PA) is needed to boost the RF power, demanding a more complicated testing scheme to attenuate the reflection signal back to VNA to ensure accurate high power measurement.

Figure 5.21 demonstrates the high-power measurement setup for the two-port frequency response of a device-under-test (DUT). The incident power coming out of VNA is set to be -20 dBm, boosted by a PA with a power gain of 45 dB, so the maximum deliverable incident power becomes 25 dBm to the left probe. The attenuators at different values are used to control the input power to be precisely at -20 dBm to +20 dBm.

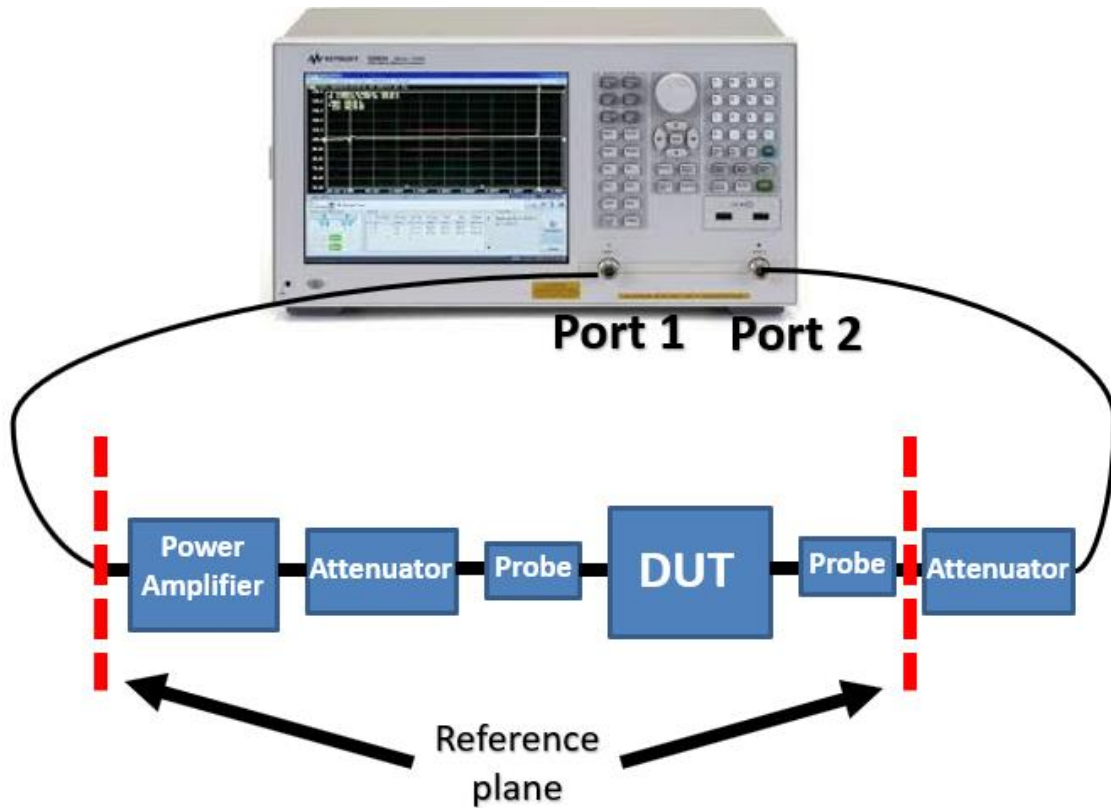


Figure 5.21 The two-port DUT device test scheme is strategically designed to enable the de-embedding process.

Before strategically implement the de-embedding technique, the standard classic open-short-load (OSL) calibration is performed on the VNA to compensate for the cables' loss and the attenuator at the right side of the DUT, so the reference planes are moved from port 1 and port 2 to the input of the amplifier and the input of the attenuator. Moreover, the full 2-port scattering parameters (S-parameters) of the PA and the attenuators are previously measured and converted to ABCD parameters, and then the ABCD parameters can be multiplied as a cascaded product of the transmission lines representing the PA and the attenuators. The resulted ABCD parameters are then rigorously converted back to the new S-parameters. The final result of the two-port devices is the product of the measured frequency response multiplied by the inverse of the new S-parameters.

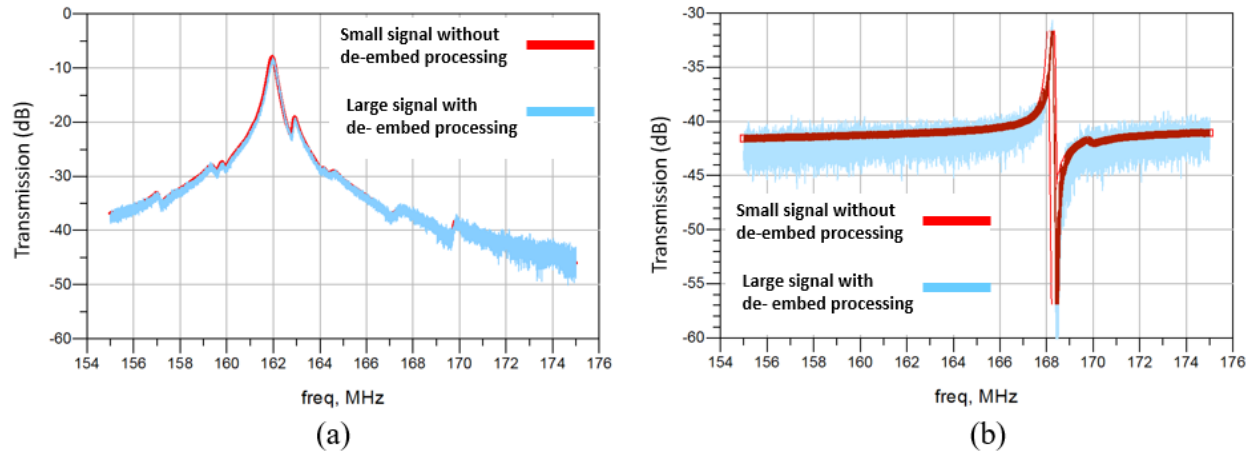


Figure 5.22 The comparisons of the measured frequency responses between the small-signal inputs and the high-power large signal inputs with proposed de-embedding data process: (a) the resonator's frequency responses on a silicon wafer; (b) the resonator's frequency response on a diamond-coat silicon wafer.

As depicted in Figure 5.22 (a) and (b), the measured result after the de-embedding process can match closely to the small-signal frequency response of the two-port devices on different wafers when the input power is -20 dBm. It is noticeable that the de-embedded results show fuzzy curves across the frequency, and that is because the PA has relatively high noise figures (4-6 dB) over the measured frequency range. The overall de-embedding process appeals to obtain a convincing outcome.

The next step is to test out the resonators' transmission response at higher power levels, and the measured data are post-processed using the described de-embedding technique. As shown in Figure 5.23 (a), the frequency responses of the resonator fabricated on a silicon wafer are presented, with the input power ranging from -20 dBm to +20 dBm, respectively. It is clear to see that the resonance peak bends over at +10 dBm, meaning the resonator starts to fail by showing a strong distortion under this high power. Figure 5.23 (b) shows the post-processed results the de-embedded results can successfully plot the frequency responses accordingly, and the insertion

losses are brought back to the levels with small-signal input, which are previously measured around to be around -7 dB.

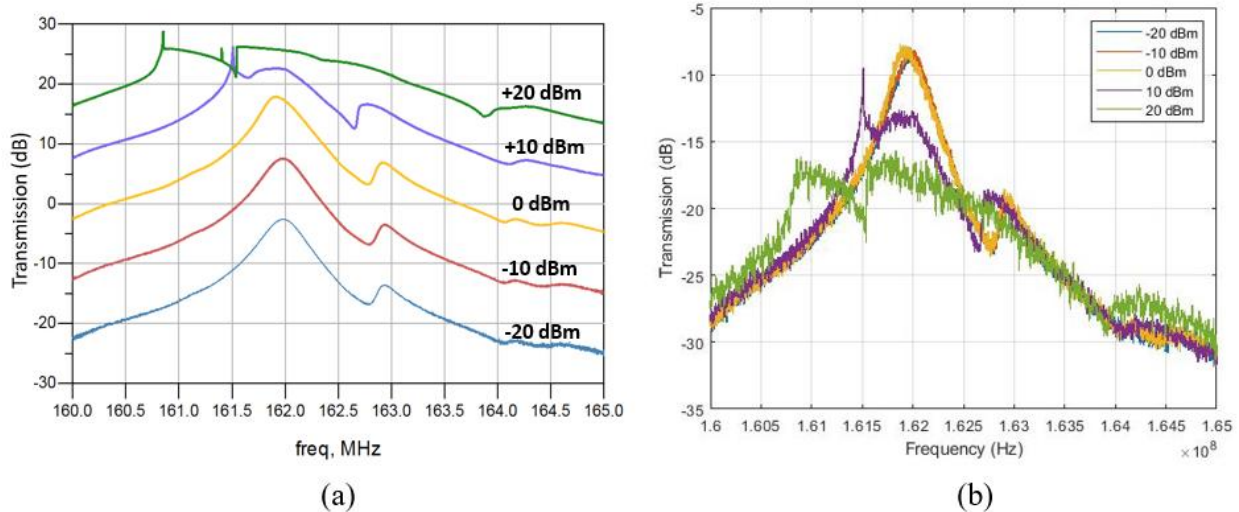


Figure 5.23 The comparisons of the two-port frequency responses wafer under high-power input of a silicon device: (a) the measured results without the de-embedding data processing; (b) the measured results with the de-embedding data processing.

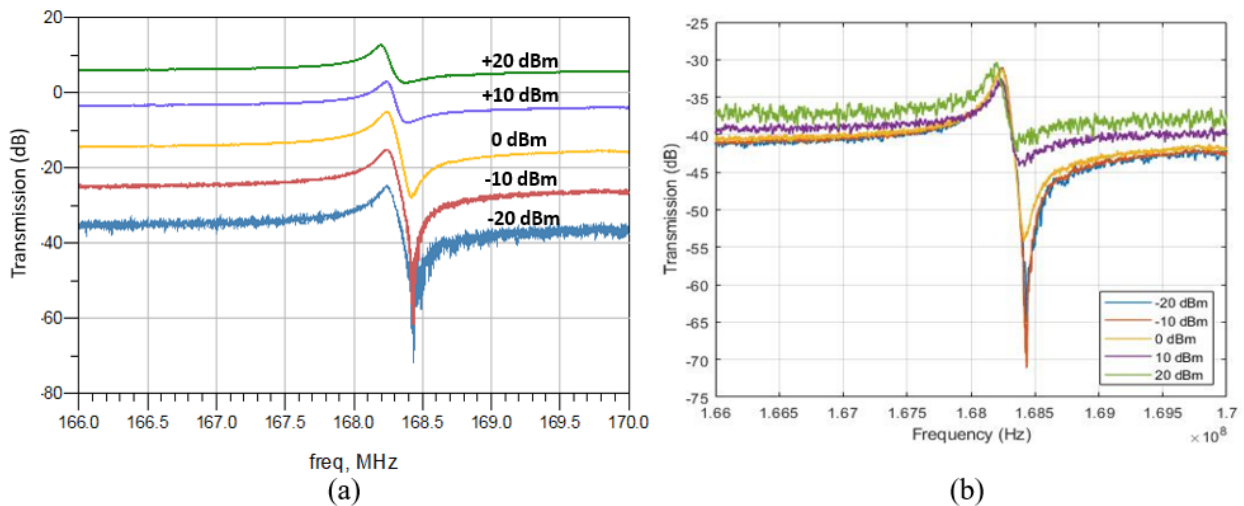


Figure 5.24 The comparisons of the two-port frequency responses wafer under high-power input of a device on a diamond-coated wafer: (a) the measured results without the de-embedding data processing; (b) the measured results with the de-embedding data processing.

The same measurement approach has also been implemented to the identically-designed resonator built on a diamond-coated silicon wafer. Similarly, as seen in Figure 5.24 (a) and (b), the frequency responses can maintain in decent shapes, although the input power is increased. The

feedthrough noise levels are elevated as the input power goes up. Meanwhile, the quality factor of the parallel resonance decreases under higher power. Additionally, it is expected that the resonances shift to the left due to the temperature increase under higher power. Comparing the results presented in the above two figures shows that the device on the diamond-coated wafer can withstand at least 10 dB more power than that of the silicon counterpart. By the employment of the diamond thin film added to the structural layer of the resonator body, the heat dissipation efficiency is tremendously improved, resulting in a much higher power handling capability.

Table 5.1 A Comparison of Resonance Responses with Different Finger-to-gap Ratios.

Finger-to-gap Ratio	4 th Width Extension Mode Freq (MHz)	Insertion Loss (dB)	6 th Width Extension Mode Freq (MHz)	Insertion Loss (dB)
16:3	213.9	22.1	Not Noticeable	NA
11:5	217.4	20.6	Not Noticeable	NA
8:8	229.1	22.5	278.6	37.8
6:10	233.4	14.5	285.3	22.8

Chapter 6: Signal-to-Noise Ratio Improvement and Portable Mass Sensing Unit

In this chapter, some innovative approaches are introduced in the first part to improve the signal-to-noise ratios (SNR). The main focus is to lower the feedthrough noise levels by noise cancellation and static capacitance reduction without sacrificing the signal strength. It is critical to achieve a higher SNR for signal detection and sensing applications. After the SNR optimizations, the resonator probing pads are extended to the edges of the die, and the die is placed inside a 3-D printed cavity with dispensed transmission lines to the SMA connector to enable a portable testing unit (connectorized assembly) without the requirement of on-wafer probing.

6.1 Notched Thin-Film Piezoelectric Interdigital Transducer for Enhanced Signal-to-Noise Ratio and Feedthrough Suppression

As discussed in the previous chapters, a resonator's feedthrough noise level is primarily determined by the static parasitic capacitance in the BVD equivalent circuit model. Meanwhile, the capacitance ratio is also inversely proportional to the electromechanical coupling coefficient. The static capacitance is formed between the sandwiched layered structure composed of the IDT metal fingers, the bottom electrodes, and the dielectric property of the piezoelectrical material. In this section, an innovative design is presented to improve the resonance signal-to-noise ratio (SNR) by introducing notched air cavities in the thin-film piezoelectric layer between interdigital transducer (IDT) electrodes of a two-port MEMS resonator [76].

ZnO-on-diamond lateral extensional mode resonators have been implemented to study the effect of the notched thin-film piezoelectric transducer with etched air cavities between the IDT

electrodes on the broadband feedthrough levels and the resonance response in terms of frequency, quality factor, and SNR. For a two-port thin-film piezoelectric resonator, the employment of notched air cavities of varied depth in between the adjacent IDT electrodes directly impacts the feedthrough level that largely depends on the parasitic capacitive coupling in between the two ports. Additionally, the partial removal of the lossy ZnO piezoelectric transducer layer also results in enhanced quality factors.

The chosen rectangular-plate resonators in this study have the dimension of $80\mu\text{m} \times 320\mu\text{m}$ with 5 IDTs, and each IDT is $13\mu\text{m}$ wide, leaving the gap size to be $3\mu\text{m}$. The feedthrough parasitic effect is initially studied with a three-dimensional finite element method (FEM) simulation using COMSOL Multiphysics. The calculated capacitance values are inserted into a circuit composing of the shunt-series-shunt capacitor combination with two terminations at both ends (ports) in Advanced Design System (ADS). In this way, an analytical feedthrough level is simulated based on the equivalent circuit model, and it is compared with the feedthrough level extracted from the real-world experimental measurement.

The FEM simulations have been first carried out using COMSOL software to investigate the strain/stress field and the change of the static capacitance made by partially removing the piezoelectric material between the IDT electrode fingers. The FEM study comprises two physics mechanisms: modal analysis and electrostatics, and each physics are subjective to observe the difference made by several parameters. For example, modal analysis is utilized to track the electrical field changes and mechanical displacement at the resonance frequencies with different structural composition in terms of the notch depth, which is defined as how much material gets etched in the gap. Similarly, the electrostatic study is selected for calculating the capacitance generated by the conductive IDTs and dielectric piezoelectric material. As depicted in Figure 6.1

below, in the simulated resonator's frequency response, the feedthrough noise levels are lowered by as much as 13 dB as the ZnO thin film is gradually removed in between the IDT fingers. While the insertion loss can still maintain at about the same level as depicted in the circled area, so the overall signal-to-noise ratios are presumably increased.

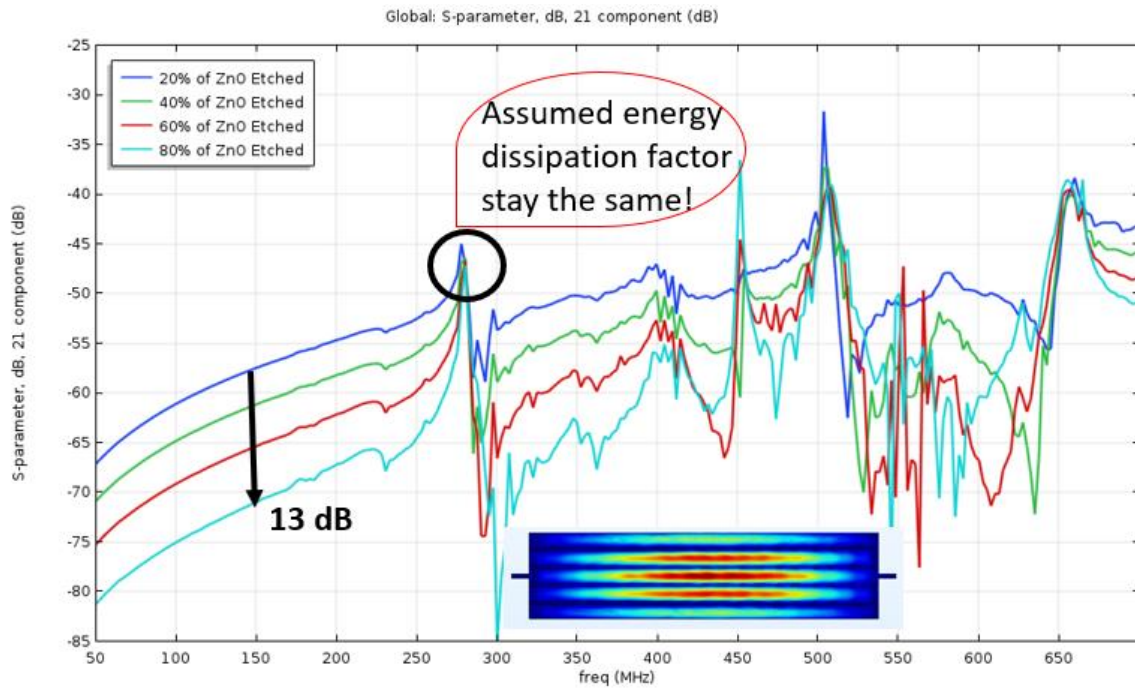


Figure 6.1 The FEM results depict the change of feedthrough noise levels due to the partial substitution of the ZnO piezoelectric transducer layer by air notches in between the IDT electrodes.

The next design parameter that influences the feedthrough level can be determined by calculating how much capacitance change is caused by etched notches between the IDTs. This turns out to be a more crucial factor because a change in capacitance between the two IDT electrodes will directly influence the two-port resonator's feedthrough level. Ideally, a lower feedthrough level over the frequency is favorable since it can contribute to an improved signal to noise ratio when the resonance peak maintains its insertion loss. In general, the capacitance calculation in the COMSOL program or even by hand is straightforward. The fringe capacitance is defined as the amount of charge that a body needs to raise its electric potential by one volt

referenced to the ground plane potential. However, that is all based on the assumption that there are only two conductors taken into consideration. The capacitance calculation becomes more complicated when more than two conductors are used in the system.

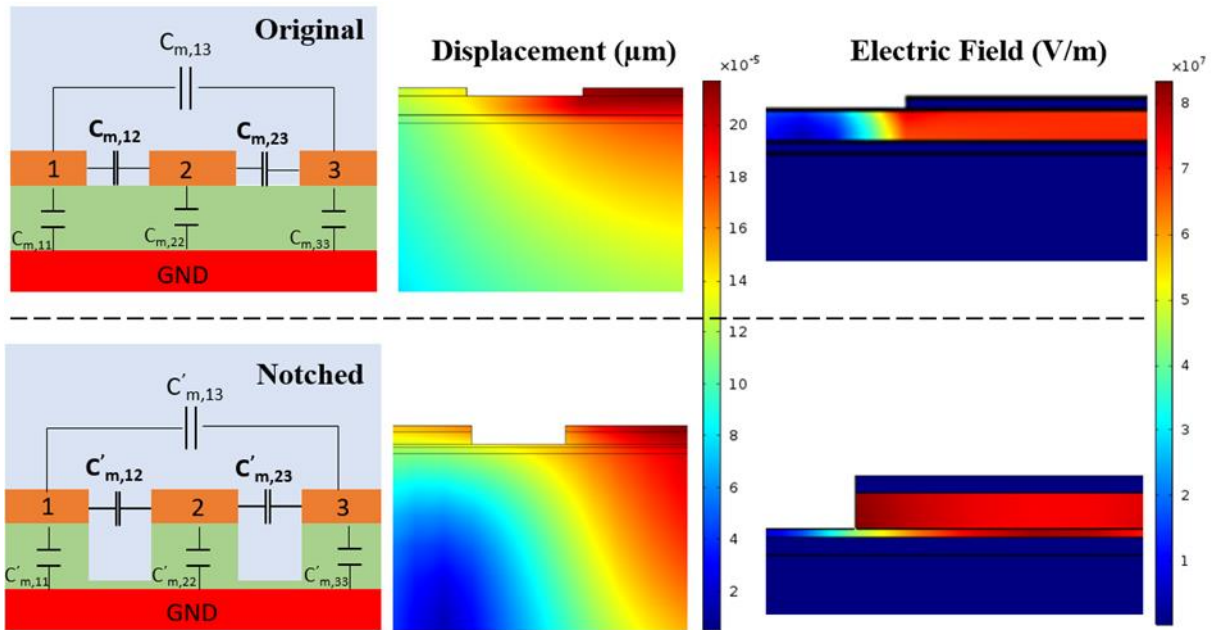


Figure 6.2 The change of electrical fields and displacement pattern due to the partial substitution of the ZnO piezoelectric transducer layer by air notches in between the IDT electrodes.

Figure 6.2 shows the comparison of simulated electric field and displacement patterns with and without the notches. As seen, the majority of displacement and electrical field is confined under the individual electrodes, and it seems to be agreeable to our assumption that etching the notch material in between the IDT electrodes makes a minimal impact on the mechanical displacement at resonance. The capacitance is generated laterally not only between the pair of IDTs or between the two ports, the capacitance is also formed vertically between the top electrodes and bottom electrode. Since there are totally three conductors in this electrical system, mutual capacitance must be introduced between several charge-holding objects, which can be calculated and arranged in a matrix form. In field theory, The Maxwell capacitance matrix expressed in

Equation 6.1 describes a relationship between the electrical charges of the i^{th} conductor to the voltages of all conductors in the system.

$$\begin{pmatrix} Q_1 \\ Q_2 \end{pmatrix} = \begin{bmatrix} C_{11} & C_{12} \\ C_{21} & C_{22} \end{bmatrix} \begin{pmatrix} V_1 \\ V_2 \end{pmatrix} \quad (6.1)$$

The mutual capacitance can be then derived as:

$$\begin{bmatrix} C_{m,11} & C_{m,12} \\ C_{m,21} & C_{m,22} \end{bmatrix} = \begin{bmatrix} C_{11} + C_{12} & -C_{12} \\ -C_{21} & C_{21} + C_{22} \end{bmatrix} \quad (6.2)$$

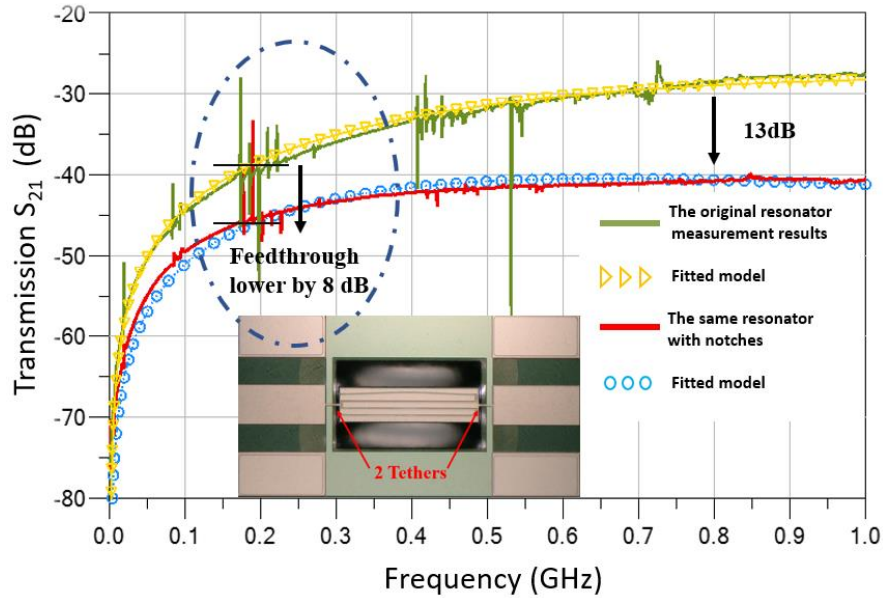


Figure 6.3 Measured frequency response of an $80\mu\text{m} \times 320\mu\text{m}$ MEMS resonator with two tethers (green) and the same resonator with etched notches/air cavities between each adjacent IDT electrode (red) as well as the equivalent circuit models that have been taken into account of both the feedthrough (noise) and the motional current (signal).

The measured results show a consistency with the FEM simulated trend when 80% of the ZnO material in between the IDT fingers is removed by dry etching. Figure 6.3 shows the frequency response for an identically-sized resonator with two tethers, which exhibits an 8 dB lower feedthrough due to the introduced notches (air cavities). It is also observed that several spurious modes have been effectively suppressed. Also, equivalent circuit models have been

developed and verified that match well with the measured results for devices with and without the newly added notches (air cavities) between the two-port IDT electrodes.

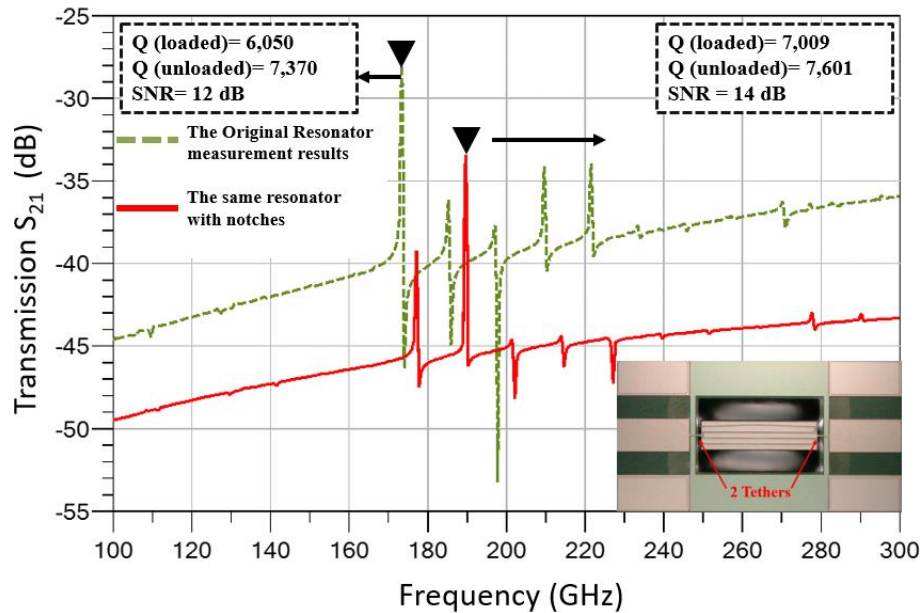


Figure 6.4 A zoom-in view of the circled area in Figure 6.13: the measured frequency responses of the first width extension mode within a narrower frequency span with and without the notched air cavity features for the same resonator design.

As shown in Figure 6.4, the unloaded quality factor increases from 6,050 to 7,009, while the SNR increases from 12 dB to 14 dB for a rectangular-plate resonator with two tethers operating at the first width extension mode. The resonance frequency is slightly increased in addition to the reduced feedthrough level and improved quality factor.

Figure 6.5 shows another example of the same methodology implemented on another resonator with ten tethers. As seen, a reduction of the feedthrough level of more than 10 dB has been achieved by incorporating the notched air cavities for a rectangular plate resonator with ten tethers, while the resonance peak drops from -28dB to -35dB that corresponds to a 3 dB SNR improvement. For this design, the resonance frequency shifts from 234 MHz to 232.7 MHz while

the quality factor is increased by 10% thanks to the partial removal of the piezoelectric layer with higher acoustic losses.

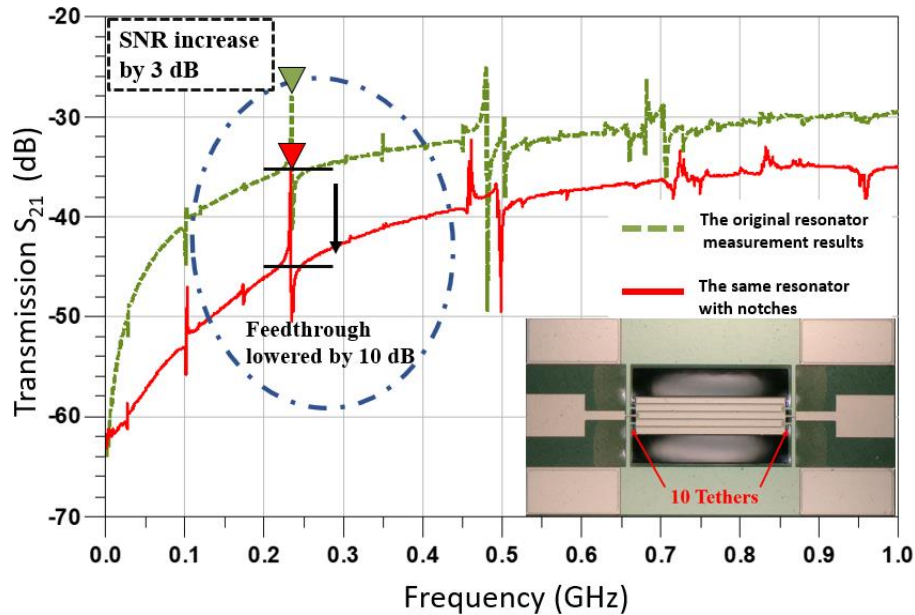


Figure 6.5 The frequency response with/without the etched notches of the resonator with 10 tethers.

To investigate the optimal notch depth with respect to the different finger-to-gap ratios, three more $80 \mu\text{m} \times 320 \mu\text{m}$ resonators have been post-processed using the proposed air notches methodology. The finger-to-gap ratios are 11:3, 8:8, 6:10, and the pitch size is set to be $16 \mu\text{m}$. The ZnO layer thickness is measured to be 500 nm , while the notch depth is gradually increased by etching the remaining ZnO from 20% - 80 % of the full ZnO thickness of 500 nm in between the IDT electrodes. The results are summarized and presented in the table below.

This technique does not negatively impact the electromechanical coupling coefficients (signal strength) or the original MEMS resonators' quality factors. Also, several spurious modes are adequately suppressed because of the modified distribution of electric fields and displacement/strain fields in the piezoelectric layer adjacent to IDT electrodes. The equivalent circuit models that combine the motional current signal and electronic feedthrough parasitic have

been successfully developed, which match well with the measured results. Given the feedthrough noise level for a two-port thin-film piezoelectric-on-substrate (TPoS) resonators operating in lateral extensional modes largely depends on the parasitic capacitive coupling between adjacent IDT electrode fingers, the introduction of notched air cavities of varied depth in between the IDT electrode fingers is anticipated to influence the level of the feedthrough noise. Meanwhile, most of the electric fields are contained in between the two-port IDT electrodes and the ground plane when the resonator device operates in its lateral extensional modes. As a result, partial removal of a portion of the thin-film piezoelectric transducer in between the IDT electrode fingers would not strongly impact the electromechanical coupling, thus sustaining an adequate signal strength at the resonance frequency. In fact, the piezoelectric thin film layer such as ZnO employed in this study tends to play a dominant role in contributing to the acoustic energy losses, thus allowing lower overall energy dissipations per cycle to achieve improved quality factor for the newly proposed device design with notches.

6.2 Feedthrough Noise Cancellation by Electrically Cascading Resonators

The cascading topology has been commonly used in narrow band-pass filter designs that are based on one or two-port piezoelectric MEMS resonators [77][78]. However, the limited Q and small coupling factor lead to poor out-of-band rejection and tiny bandwidth, while high motional resistance makes it very difficult to operate in a $50\text{-}\Omega$ system. Nevertheless, the cascading approach can still be viable for sensing and detection applications, where the SNR is deemed to be critical, but the motional impedance or insertion loss plays a less pivotal role.

In this section, a system-level strategy has been employed to lower the feedthrough noise levels by cascading multiple resonators, thus resulting in signal-to-noise ratios to be drastically boosted. In fact, in the BVD equivalent circuit model, when the resonators are electrically coupled,

the total static capacitance is reduced due to the mitigation of the static capacitance through all the cascaded resonators between the two ports. Meanwhile, the spurious modes at the lower frequency range are “buried” under the measuring instrument's ambient noise floor.

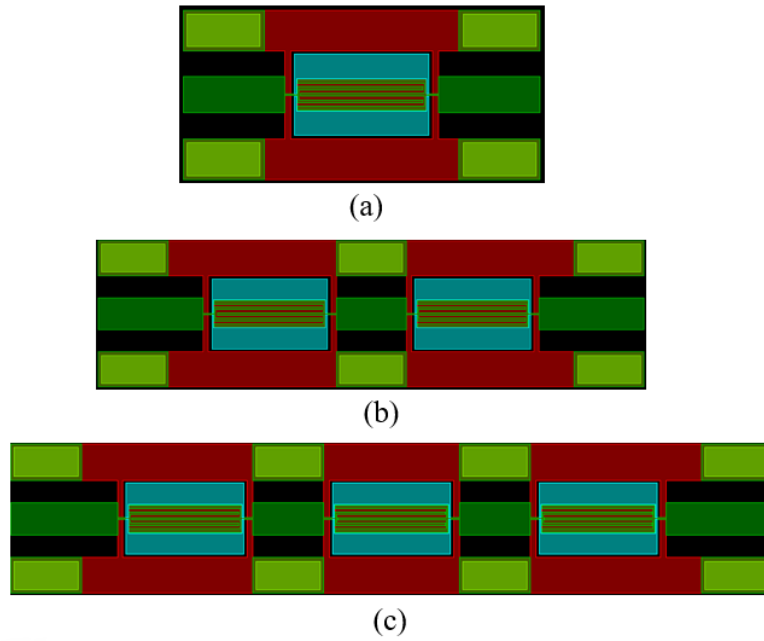


Figure 6.6 The mask views of the cascaded two-port rectangular resonator(s): (a) $\times 1$; (b) $\times 2$; (c) $\times 3$.

A comparison has been made between one single standalone rectangular-shaped resonator versus the multiple ones cascaded together. As seen in Figure 6.6 (a)-(c), the resonators have been electrically coupled by connecting the first two-port resonator's output signal pad to the input signal pad of the second resonators. The particular resonator consists of 5 IDT fingers, and the pitch size is set to be $16 \mu\text{m}$, with a finger-to-gap ratio of 8:8. The transducer area is set to be $80 \mu\text{m} \times 320 \mu\text{m}$, and a 500 nm-thick ZnO thin film has been deposited as the piezoelectric layer.

As depicted in Figure 6.7 above, the green curve represents the frequency response of the single two-port resonator. The feedthrough noise level is found to be -40 dB, resulting in small signal-to-noise ratios of 25 dB or so. However, when two or more resonators are cascaded together, the noise floor is dramatically lowered to -80 dB. The SNR of the resonance peak is increased

from 25 dB to 55 dB at 138 MHz, while the SNR of another peak at 230 MHz is also increased from 17 dB to 60 dB. Meanwhile, the spurious modes at lower frequencies are also suppressed by adding more resonators into the cascaded resonator array. Obviously, the insertion losses maintain at about the same levels, but the noise floors are well below the single device ambient noise floor.

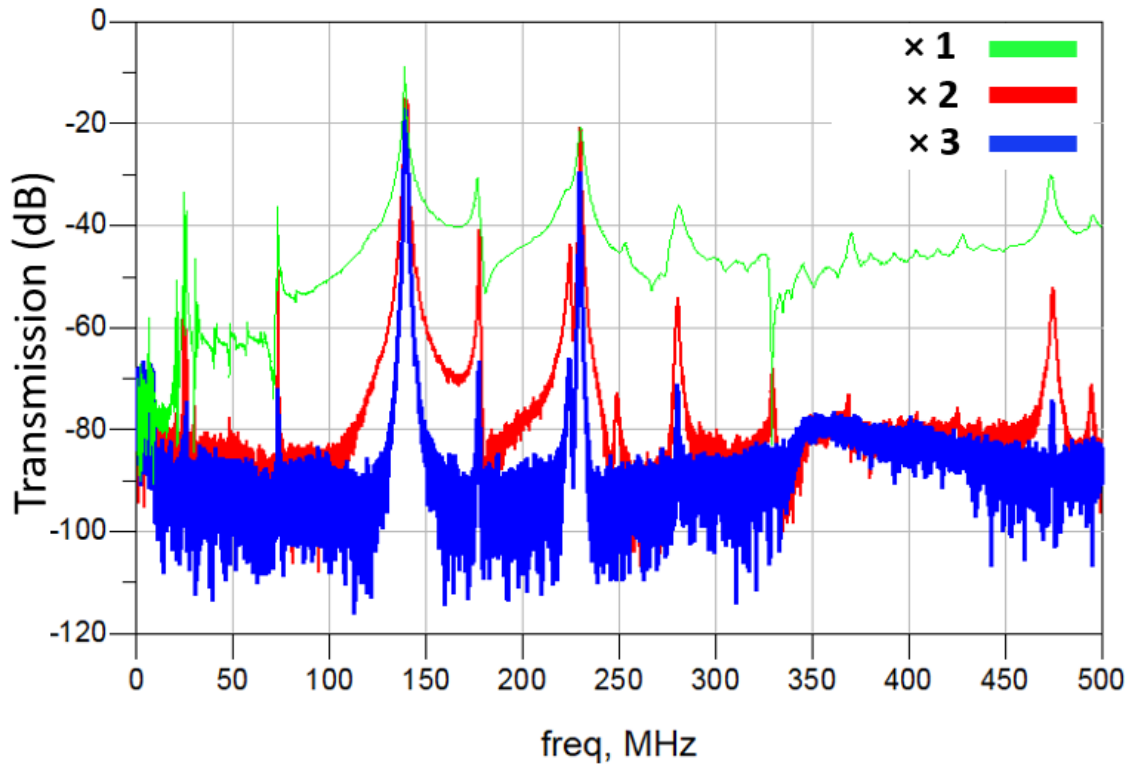


Figure 6.7 A comparison of the measured frequency responses between the single two-port resonator (green curve) and the cascading resonators ($\times 2$, red curve; $\times 3$, blue curve).

The cascading topology has also been implemented on the other devices, which have much smaller pitch sizes but higher feedthrough noise levels. The particular rectangular plate resonator has 42 IDT fingers and an IDT pitch size of $4 \mu\text{m}$, along with a finger-to-gap ratio of 2:2. The aperture length is $100 \mu\text{m}$, making the transducer area to be $170 \mu\text{m} \times 100 \mu\text{m}$, and a 500 nm -thick ZnO thin film has been deposited as the piezoelectric layer. Similarly, two and three resonators are cascaded together for making a direct comparison.

As shown in Figure 6.8 below, the resonance frequency of the single resonator is much higher than that in the previous example because the pitch size is four times smaller. In the meantime, the feedthrough noise of a single resonator with a small IDT pitch size is also elevated as the frequency goes up, resulting in a much smaller SNR. By using the cascading topology, the noise floor is lowered by more than 30 dB, while the insertion losses are only increased by 10 dB, so the overall signal-to-noise ratios are improved by 20 dB.

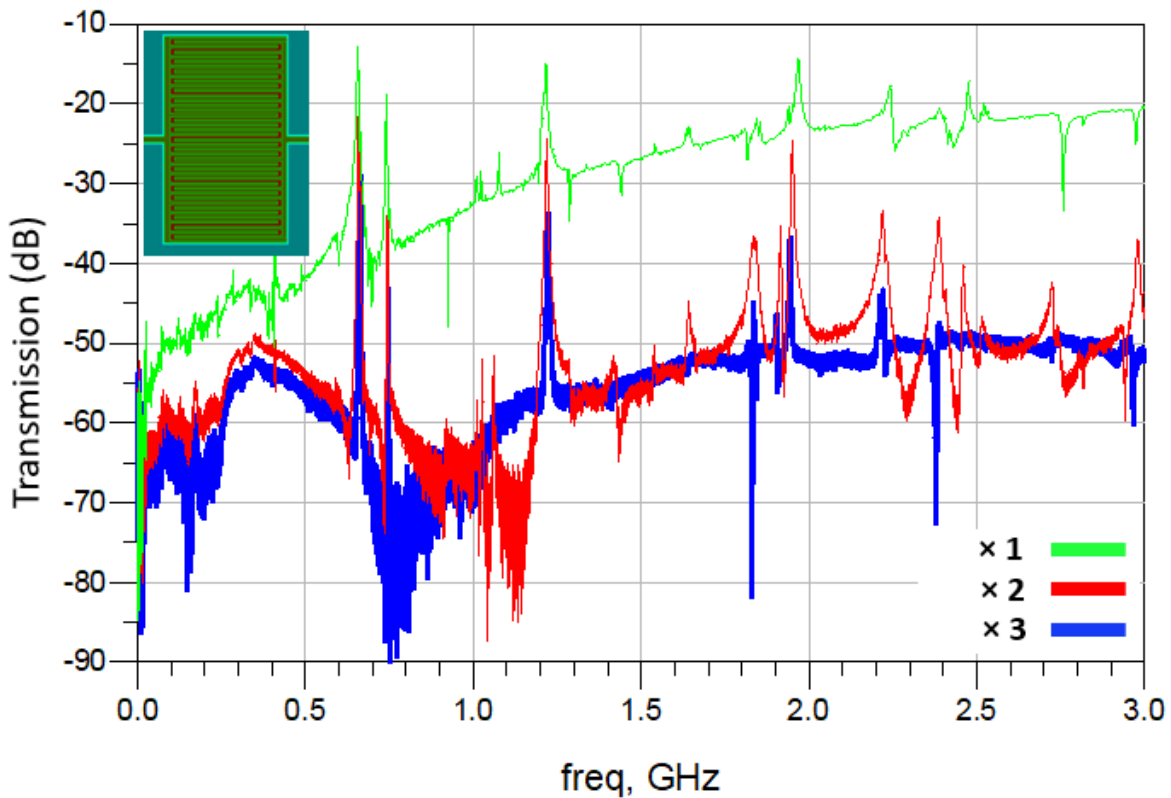


Figure 6.8 A comparison of the measured frequency responses between the single two-port resonator (green curve) and the cascading resonators ($\times 2$, red curve; $\times 3$, blue curve).

6.3 De-ionized Water Droplet Test and Portable Mass Sensing Unit

In this section, the droplet test has been performed to sense the different mass of the de-ionized (DI) water. The ground-signal-ground (GSG) probing pads of the MEMS resonators are extended to about 1 cm long, all the way to the edge of the die to keep the proper distance between the probe tips on both sides to separate wet analytes from both ports. With the longer extension

lines, the resonator's insertion loss is expected to be higher due to the high impedance. A pipette is used to accurately pick 0.8 μl DI water each time. Figure 6.9 presents the measured results before and after 0.8 μl , and 1.6 μl of DI water droplets are dispensed onto the resonator.

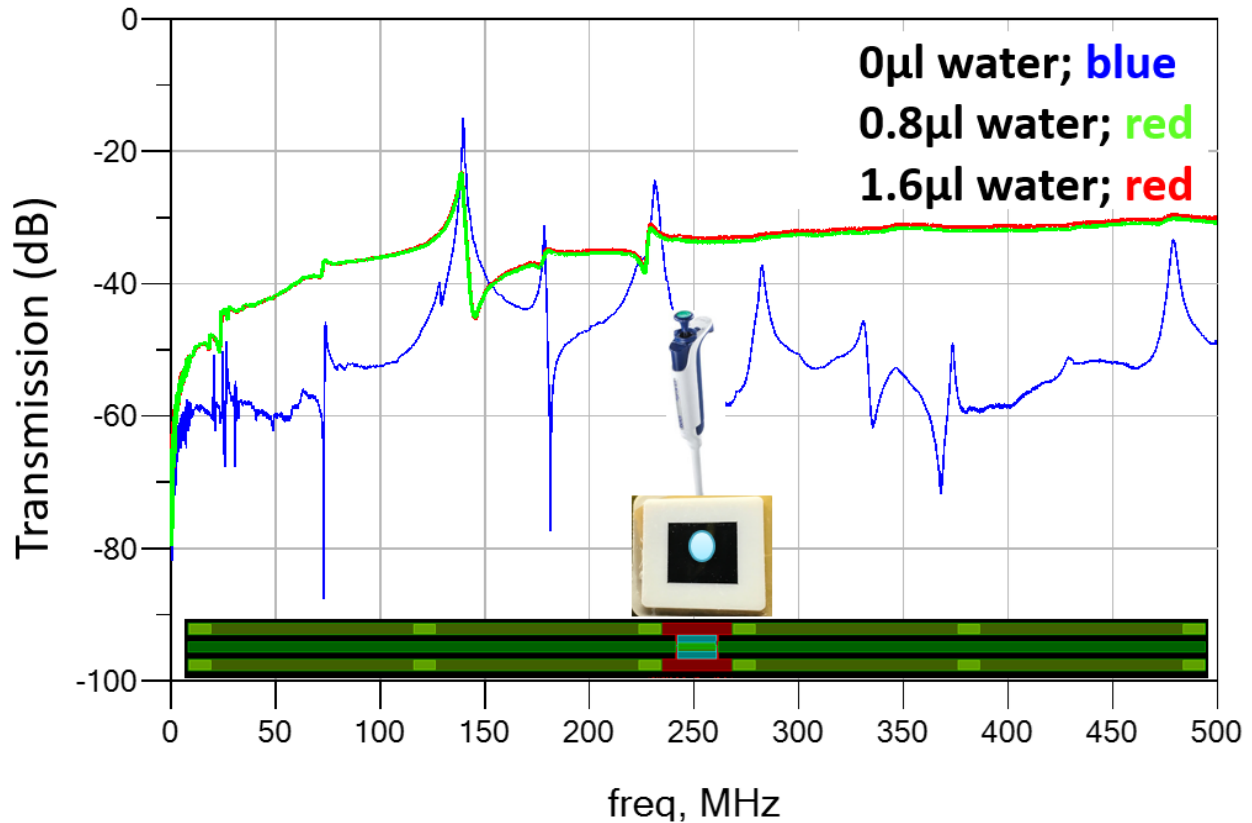


Figure 6.9 A comparison of the measured frequency responses of the two-port piezoelectric MEMS resonator during the droplet testing.

As a 0.8 microliter DI water droplet is applied to the resonator structural body, the insertion loss increases from 17.2 dB to 21.8 dB, and the quality factor has also dropped from 231 to 162. The spurious modes are largely suppressed due to the extra loaded mass. There is a negligible difference when another 0.8 ml droplet is added, showing limited effects of viscous damping.

This droplet testing was performed on a probe station. The appropriate packaging needs to be cooperated to directly connect the GSG probe pads to SMA connectors and a VNA to enable a

portable sensing setup. The testing board is 3-D printed with a 500 μm deep cavity by the milling function, and the routing lines are micro-dispensed using CB 028 conductive silver paste.

Chapter 7: Conclusions and Future Works

7.1 Conclusions

In this dissertation, the design, micro-fabrication, modeling, and testing of the piezoelectrically-transduced ZnO thin film acoustic MEMS resonators have been thoroughly studied and implemented. Initially, a comprehensive literature review has been performed to cover the most current-state-of-art piezoelectric acoustic resonators and the related applications. It provides very useful and detailed explanations and side-to-side comparisons of the acoustic technologies, such as SAW, BAW, and the proposed contour-mode resonators, so the readers should benefit from a glance of the systematic view and summary.

The piezoelectric effect and basic acoustic knowledge have been discussed to set the foundation to understand the operation principle of the piezoelectric acoustic resonator. The ZnO thin film has been fully characterized by different deposition conditions using the AJA sputtering system. The correlation of the k^2t and resistivity of the sputter ZnO thin films have been optimized by multiple measurements. It is found that the best thin film quality is achieved when the process gas includes 50% oxygen gas, and the substrate temperature is set at 300 °C, followed by the post-annealing at 600 °C to reduce the internal stress. For the first time, the omega-scan rocking curve measurement has also been successfully performed using the existing XRD equipment at the Nanotechnology Research & Education Center (NREC) at the University of South Florida.

Furthermore, the acoustic resonator is modeled using the BVD equivalent circuit model and the FEM simulations in order to evaluate the predicted resonator performance using different

design parameters, so the simulated results provide the design trends that eventually are implemented into design variations during the layout masking. The methodology used in FEM in Comsol can directly predict the frequency responses of the devices, providing two-port S-parameters with a very reasonable speed for a 3-D model simulation with large degrees of freedom. After many attempts and modifications, the simulation model has been well developed as a sample file for future research.

After that, the entire micro-fabrication process has been done successfully based on the in-house process development and equipment at NREC at the University of South Florida. A great amount of effort has been spent on micro-machining technologies to fulfill the research's needs. For example, for the first time, a 2 μm feature size has been achieved using the metal lift-off method with an EVG mask aligner. The optimal thickness of the LOR-3B must be 1.5 times greater than that of the metal thickness. For a 220 nm-thick electrode layer, the LOR-3B's thickness needs to be maintained at 400 nm, and the photoresist (AZ 1512) cannot also be too thick because it would affect the resolution.

Furthermore, the exposure dosage is defined as the product of the UV power and the exposure time, controlling the over or under-development profiles. Theoretically, one can have the same outcome if the exposure dosage is kept the same, but it is found that many photoresists are very sensitive to the high power, so it is recommended to reduce the power to 7-9 mW/sec and increase the time to have more control. The diamond dry etching recipe has also been developed and optimized using an Adixen DRIE tool. The estimated etch rate is about 350 nm/min in a pure oxygen plasma environment and very high power. For any dry etch process with a high of more than 2500 watts, it is not recommended to run a long process for more than 10 minutes with a

pause because significant heat generated may burn the sample's material, such as the photoresist. Instead, a 40-minute dry etching process should be broken into four 10-minute ones.

The fabricated resonators are measured by the on-wafer probing method, and the results show many interesting and promising observations. The aperture size of the rectangular-shaped contour-mode resonators must be long enough to ensure resonance sharpness and low insertion losses. Also, with the same IDT pitch size, the different finger-to-gap ratios have been investigated on the contour-mode resonators for the first time. The capacitive feedthrough levels can be lowered as the finger-to-gap ratios reduce, and both the resonance frequencies are slightly increased in the meantime. Additionally, the compared results show the tether's width and length is proportional to the loss dissipated into the substrate. Phononic-crystal designs have also been employed to reduce the tether loss and suppress the spurious modes at lower frequencies. It is found that the diamond-shaped PCs stand out as compared to other shapes in the PC design. The measured insertion loss is as low as 5.82 dB at 128.3 MHz, which is lower than the previously reported on a rectangle ZnO MEMS resonator, but the quality factor is low (230-380) because of the high dielectric loss of the deposited ZnO thin film. To address this concern, a thin-film diamond has been employed as a part of the resonator structural layer by the adjusted fabrication process built on a diamond-coated silicon wafer. The equivalent acoustic velocity and Young's modulus have been significantly boosted, so the resonance frequencies (over three times higher) and the quality factors (as high as 6050) are much higher than the identically-designed resonators fabricated on the silicon wafers. Meanwhile, the temperature and the power handling performance are found out to be much better on the resonators with the diamond thin film on their structural bodies, where the TC_f is measured at -14.05 ppm/°C without any temperature compensation technique. For the first time, the power handling capability testing has been performed on a two-port piezoelectric

acoustic resonator. The newly designed de-embedding system works beautifully to compensate for the added PA and attenuators used to produce large-power signals. With the extremely high thermal conductivity of the diamond thin film, the single resonator can withstand more than 20 dBm input power, making it very promising for next-generation filtering and timing applications that demand more power-handling capabilities.

An innovative design improves the resonance signal-to-noise rate (SNR) by 3 - 10 dB by introducing notched air gaps in the thin-film piezoelectric transducer between interdigital transducer (IDT) electrodes of a MEMS resonator. In the meantime, several spurious modes can be effectively suppressed or fully eliminated due to the modified distribution of the electrical field and displacement/strain field in the piezoelectric transducer layer adjacent to IDT electrodes. The equivalent circuit models that combine the motional current and electronic feedthrough parasitic have been successfully developed, which match well with the measured results. To further improve the SNR, two and three resonators are cascaded together, so the static capacitance has been canceled out each other, leading to a 30-40 dB feedthrough noise reduction and a 20-40 dB SNR improvement.

7.2 Future Works

Due to the facility limitations, ZnO was used as the piezoelectric material in this dissertation for “proof-for-concept” purposes. In fact, AlN thin film is widely proven to be a much better piezoelectric material for its higher acoustic velocity and coupling factor. Compared to ZnO, AlN exhibits a lower loss and can be compatible with the CMOS foundry. Therefore, it would be nice to replace the ZnO thin film with AlN in the future for better performance. Although the quality factor, temperature, and power handling performance have been largely improved by the employment of the diamond thin film as part of the resonator’s structural layer, the insertion loss

and the electromechanical coupling factor is found worse than the silicon counterpart, and the measured motional resistance is also quite high (more than 500 Ω). This makes it impossible to be utilized for filter designs. The poor k^2t indicates the deposited ZnO's piezoelectric property is not good enough to support an acceptable bandwidth because the surface roughness of the diamond thin film looks very coarse from the AFM scan. Therefore, the NCD growth needs to be characterized.

The FEM simulations provide design ideas and trends, but there is certainly more work to be done. For example, the capacitive feedthrough levels and resonance frequency locations need to match the measured ones closely so that the FEM model can be relied on for more design variations. Tether loss has not been included in the existing simulation, so it is very beneficial to implement a specific model focused on tracking the loss change at the tethers. It would also be great to spend time in the thermal simulation using the FEM tool, such as IcePak or Comsol. The dissertation presents the frequency responses by changing the temperature and incident power individually. However, the device temperature is still unknown under a specific input power level, so it is worth a great deal to be able to simulate the frequency responses under high-power inputs.

Dummy finger designs have been adopted into the contour-mode resonators, aiming to suppress unwanted wave dispersion, but very subtle influences are found because the length of the dummy fingers is too short. Hence, it is worthy of running a parametric study using FEM simulations to investigate how different length of dummy fingers may impact the resonator's performance.

The innovatively designed air notch can lower the feedthrough noise while maintain the signal strength by partially removing the ZnO in between the adjacent IDT fingers because the static capacitance has been reduced. The capacitance ratios (motional capacitance over static

capacitance) should also be lowered, resulting in a larger coupling, but in many devices, the measurement results show most of the resonance peaks do not have a parallel resonance because of the high static resistance on the resonator fabricated on the silicon wafers. Theoretically, the static capacitance reduction causes a high capacitance ratio, leading to a higher coupling coefficient.

As to the measurements, with diamond thin film added to the resonators' structures, the device can handle as high as 20 dBm input power without failing, but it should still be more, so a PA with more power is needed to see where the limit is. The two-port power measurement seems very promising as it can capture the frequency responses at different levels of power. However, such a measurement setup and the de-embedding system cannot be implemented on a one-port resonator, which is primarily used for commercialized filters. Therefore, it would be of great significance if the high-power frequency responses measurement setup and de-embedding system are implemented to a one-port passive device.

Also, the droplet test has been performed, and the 3-D printed packing enables portable testing without the need of probing. The 3-D printed package needs to be further improved to fit the device more precisely. The routing lines to the SMA connectors must also be carefully designed and simulated in an EM environment. The long routing lines increase the impedance over the frequencies, so the equivalent circuit model and the related EM simulation are needed to extract the droplet experiment's actual data.

References

- [1] J. Lu et al., "Piezoelectric MEMS devices and its application as bio-chemical sensors," The 8th Annual IEEE International Conference on Nano/Micro Engineered and Molecular Systems, pp. 163-166, 2013.
- [2] M. Maute et al., "Fabrication and application of polymer coated cantilevers as gas sensor", *Microelectronic Engineering*, Vol.46, pp.439-442, 1999.
- [3] P.Waggoner, H.G.Craighead, "Micro- and nanomechaical sensors for enviromental, chemical, and biological detection", *Lab Chip*, Vol.7, pp.1238-1255, 2007.
- [4] J. Lu et al., "Hybrid piezoelectric mems resonators for application in bio-chemical sensing," *Journal of Applied Science and Engineering*, iss.1, vol. 17, pp.17-24, 2014.
- [5] L. Bueno et al., "Voltammetric electronic tongue for discriminationof milk adulterated with urea, formaldehyde and melamine," *Chemosensors*, vol. 2, no. 4, pp. 251-266, 2014.
- [6] B. Jakoby, and M. Vellekoop, "Physical sensors for water-in-oil emulsions," *Sensors and Actuators A: Physical*, vol. 110, no. 1-3, pp. 28-32, 2004.
- [7] K. Ping, S. Doerner, T. Schneider, D. Allara, P. Hauptmann, and S. Tadigadapa, "A Micromachined Quartz Resonator Array for Biosensing Applications," *Microelectromechanical Systems*, *Journal of*, vol. 18, pp. 522-530, 2009.
- [8] V. M. Mecea, "Is quartz crystal microbalance really a mass sensor," *Sensors and Actuators A: Physical*, vol. 128, pp. 270-277, 2006.
- [9] H. Campanella, J. Esteve, J. Montserrat, A. Uranga, G. Abadal, N. Barniol, et al., "Localized and distributed mass detectors with high sensitivity based on thin-film bulk acoustic resonators," *Applied Physics Letters*, vol. 89, pp. 033507-033507-3, 2006.
- [10] W. D. Bowers, R. L. Chuan, and T. M. Duong, "A 200 MHz surface acoustic wave resonator mass microbalance," *Review of Scientific Instruments*, vol. 62, pp. 1624-1629, 1991.
- [11] Z. Chen and F. Zhao, "Single crystalline 4H-polytype silicon carbide microresonator sensor for mass detection," *Materials Letters*, vol. 128, pp. 64-67, 2014.

- [12] C. Zuniga, M. Rinaldi, S. M. Khamis, A. T. Johnson, and G. Piazza, "Nanoenabled microelectromechanical sensor for volatile organic chemical detection," *Applied Physics Letters*, vol. 94, pp. 223122, 2009.
- [13] A. Cagliani and Z. J. Davis, "Ultrasensitive bulk disk microresonator-based sensor for distributed mass sensing," *Journal of Micromechanics and Microengineering*, vol. 21, pp. 045016, 2011.
- [14] M. Shiddiky, A. Torriero, "Application of ionic liquids in electrochemical sensing systems," *Biosensors and Bioelectronics*, vol. 26, no. 5, pp. 1788-1799, 2011.
- [15] T. Manzanque et al., "Piezoelectric MEMS resonator-based oscillator for density and viscosity sensing," *Sensors and Actuators A: Physica*, vol. 220, pp. 305-315, 2014.
- [16] J. Wang, J. E. Butler, T. Feygelson and C. Nguyen, "1.51-GHz nanocrystalline diamond micromechanical disk resonator with material-mismatched isolating support," 17th IEEE International Conference on Micro Electro Mechanical Systems. pp. 641-644, 2004.
- [17] J. Wang, Z. Ren, and C. Nguyen, "1.156-GHz self-aligned vibrating micromechanical disk resonator," *IEEE Transactions on Ultrasonics, Ferroelectrics, and Frequency Control*, vol. 51, no. 12, pp. 1607-1628, 2004.
- [18] T. Kimura, M. Omura, Y. Kishimoto and K. Hashimoto, "Comparative study of acoustic wave devices using thin piezoelectric plates in the 3–5-GHz range," in *IEEE Transactions on Microwave Theory and Techniques*, vol. 67, no. 3, pp. 915-921, 2019.
- [19] T. Takai et al., "I.H.P. SAW technology and its application to microacoustic components (Invited)," 2017 IEEE International Ultrasonics Symposium (IUS), pp. 1-8, 2017.
- [20] T. Scheiter, H. Kapels, K.-G. Oppermann, M. Steger, C. Hierold, W. M. Werner, and H.-J. Timme, "Full integration of a pressuresensor system into a standard BiCMOS Process", *Sensors and Actuators A: Physical*, vol. 67, pp. 211–214, 1998.
- [20] G. Piazza, P. J. Stephanou and A. P. Pisano, "Piezoelectric aluminum nitride vibrating contour-mode MEMS resonators," *Journal of Microelectromechanical Systems*, vol. 15, no. 6, pp. 1406-1418, 2006.
- [21] <https://www.cyberphysics.co.uk/topics/medical/Ultrasound/piezoElectric.html>
- [22] Ikeda, Takuro. *Fundamentals of Piezoelectricity*. Oxford University Press, 1996.
- [23] ANSI/IEEE, IEEE standard on piezoelectricity. IEEE Standard 176-1987, 1987.
- [24] J. Tichý, *Fundamentals of Piezoelectric Sensorics: Mechanical, Dielectric, and Thermodynamical Properties of Piezoelectric Materials*. Verlag Berlin Heidelberg: Springer, 2010.

- [25] M.-A. Dubois and P. Muralt, "Properties of aluminum nitride thin films for piezoelectric transducers and microwave filter applications," *Applied Physics Letters*, vol. 74, pp. 3032-3034, 1999.
- [26] B. A. Auld, *Acoustic Fields and Waves in Solids*, New York: Wiley, 1973.
- [27] H. Iwanaga, A. Kunishige, and S. Takeuchi, "Anisotropic thermal expansion in wurtzite-type crystals," *J. Mater. Sci.*, vol. 35, pp. 2451-2454, May 2000.
- [28] E. Bowen, H. Kim, P. Weaver, and S. Dunn, "Piezoelectric and ferroelectric materials and structures for energy harvesting applications," *Energy Environ. Sci.*, vol 7, pp 25-44, 2014.
- [29] Kallaev, S.N., Gadzhiev, G.G., Kamilov, I.K. et al. Thermal properties of PZT-based ferroelectric ceramics. *Phys. Solid State* 48, 1169–1170, 2006.
- [30] D. L. Raimondi, and E. Kay, "High resistivity transparent ZnO thin films," *Journal of Vacuum Science and Technology*, vol 7, pp 96-99, 1970.
- [31] Powell, C.F.; Oxley, J.H.; Blocher, J.M. *Vapour Deposition*; John Wiley & Sons: New York, NY, USA, 1966.
- [32] T. Yamamoto, T. Shiosaki, and A. Kawabata, "Characterization of ZnO piezoelectric films prepared by rf planar-magnetron sputtering," *Journal of Applied Physics*, vol 51, no.6, pp 3113-3120, 1980.
- [33] Ozgur, U., Alivov, Y. I., Liu, C., et al. "A comprehensive review of ZnO materials and devices," *Journal of Applied Physics*, vol 98, no. 4, pp. 041301, 2005.
- [34] A. Baptista, F. Silva, et al. "Sputtering physical vapour Deposition (PVD) coatings: a critical review on process improvement and market trend demands," *Coatings*, no. 8, pp. 402, 2018.
- [35] D. A. Feld, R. Parker, R. Ruby, P. Bradley and S. Dong, "After 60 years: A new formula for computing quality factor is warranted," 2008 IEEE Ultrasonics Symposium, pp. 431-436, 2008.
- [36] R. Ruby, "11E-2 review and comparison of bulk acoustic wave FBAR, SMR technology," 2007 IEEE Ultrasonics Symposium Proceedings, pp. 1029-1040, New York, NY, 2007.
- [37] R. Schneider, "High-Q AlN contour mode resonators with unattached, voltage-actuated electrodes," UC Berkeley. ProQuest ID: Schneider_berkeley_0028E_15893. Merritt ID: ark:/13030/m5sv2bnj. Retrieved from <https://escholarship.org/uc/item/7v82z9fr>
- [38] J. Larson, P. Bradley, S. Wartenberg and R. Ruby, "Modified Butterworth-Van Dyke circuit for FBAR resonators and automated measurement system," 2000 IEEE Ultrasonics Symposium. Proceedings. An International Symposium, vol. 1, pp. 863-868, 2000.

- [39] H. Campanella, Acoustic wave and electromechanical resonators: concept to key applications. Boston: Artech House, 2010.
- [40] Robert A. Johnson. Mechanical filters in electronics. Wiley series on filters. Wiley, 1983.
- [41] J. Clark, W. Hsu, M. Abdelmoneum and C. Nguyen, "High-Q UHF micromechanical radial-contour mode disk resonators," in Journal of Microelectromechanical Systems, vol. 14, no. 6, pp. 1298-1310, Dec. 2005.
- [42] J. G. E. Gardeniers, Z. M. Rittersma, and G. J. Burger, "Preferred orientation and piezoelectricity in sputtered ZnO films," Journal of Applied Physics, vol. 83, no. 12, pp. 7844-7854, 1998.
- [43] O. Roger, H. Essone-Obame et al., "Capacitive properties of zinc oxide thin films by radiofrequency magnetron sputtering," J. Theor. Appl. Phys. vol. 12, pp. 309–317, 2018.
- [44] C. Lin, Y. Chen, V. V. Felmetger, G. Vigevani, D. G. Senesky and A. P. Pisano, "Micromachined aluminum nitride acoustic resonators with an epitaxial silicon carbide layer utilizing high-order Lamb wave modes," 2012 IEEE 25th International Conference on Micro Electro Mechanical Systems (MEMS), pp. 733-736, Paris, 2012.
- [45] J. Zou and C. S. Lam, "Electrode design of AlN Lamb wave resonators," 2016 IEEE International Frequency Control Symposium (IFCS), pp. 1-5, New Orleans, LA, 2016.
- [46] S. Ghaffari, S. A. Chandorkar, S. Wang, E. J. Ng, C. H. Ahn, V. Hong, Y. Yang, and T. W. Kenny, "Quantum limit of quality factor in silicon micro and nano mechanical resonators," Sci. Rep., vol. 3, pp. 3244, 2013.
- [47] L. Wu, M. Akgul, Z. Ren, Y. Lin, W. Li, and C. Nguyen, "Hollow stems for higher micromechanical disk resonator quality factor", in Proc. IEEE Intl. Ultrason. Symp., pp. 1964-1967, 2011.
- [48] F.-C. Hsu, J.-C. Hsu, T.-C. Huang, C.-H. Wang, and P. Chang, "Design of lossless anchors for microacoustic-wave resonators utilizing phononic crystal strips," Appl. Phys. Lett., vol. 98, pp. 143505, 2011.
- [49] L. Sorenson, J. L. Fu, and F. Ayazi, "One-dimensional linear acoustic bandgap structures for performance enhancement of AlN-on-silicon micromechanical resonators," in Proc. Int. Conf. Solid-State Sens. Actuators Microsyst., pp. 918–921, 2011.
- [50] F.-C. Hsu, J.-C. Hsu, T.-C. Huang, C.-H. Wang, and P. Chang, "Reducing support loss in micromechanical ring resonators using phononic band-gap structures," J. Phys. D: Appl. Phys., vol. 44, pp. 375101, 2011.
- [51] D. Feng, D. Xu, G. Wu, B. Xiong, and Y. Wang, "Phononic crystal strip based anchors for reducing anchor loss of micromechanical resonators," J. Appl. Phys., vol. 115, pp. 024503, 2014.

- [52] C. M. Lin, J. C. Hsu, D. G. Senesky and A. P. Pisano, "Anchor loss reduction in ALN Lamb wave resonators using phononic crystal strip tethers," 2014 IEEE International Frequency Control Symposium (FCS), pp. 1-5, Taipei, 2014.
- [53] H. Zhu, J. Lee, "Design of phononic crystal tethers for frequency-selective quality factor enhancement in AlN piezoelectric-on-silicon resonators," *Procedia Engineering*, vol. 120, pp. 516-519, 2015.
- [54] C. Lin, Y. Lai, J. Hsu, Y. Chen, D. Senesky, and A. Pisano, "High-Q aluminum nitride Lamb wave resonators with biconvex edges," *Appl. Phys. Lett.*, vol. 99, pp. 143501, 2011.
- [55] J. Zou, C.-M. Lin, and A.P. Pisano, "Anchor loss suppression using butterfly-shaped plates for AlN Lamb wave resonators," in *Proc. IEEE Int. Freq. Contr. Symp. & the Eur. Freq. Time Forum (FCS)*, pp. 432-435, 2015.
- [56] C. Tu and J. Lee, "VHF-band biconvex AlN-on-silicon micromechanical resonators with enhanced quality factor and suppressed spurious modes," *J. Micromech. Microeng.*, vol. 26, pp. 065012, 2016.
- [57] M. Siddiqi, C. Tu and J. Lee, "Effect of curvature and electrode coverage on the quality factor of biconvex ALN-on-Si MEMS resonators," 19th International Conference on Solid-State Sensors, Actuators and Microsystems (TRANSDUCERS), pp. 98-101, Kaohsiung, 2017.
- [58] W. Pan and F. Ayazi, "Thin-film piezoelectric-on-substrate resonators with Q enhancement and TCF reduction," 2010 IEEE 23rd International Conference on Micro Electro Mechanical Systems (MEMS), pp. 727-730, Hong Kong, 2010.
- [59] H. Yu, W. Pang, H. Zhang and E. S. Kim, "Ultra temperature-stable bulk-acoustic-wave resonators with SiO₂ compensation layer," in *IEEE Transactions on Ultrasonics, Ferroelectrics, and Frequency Control*, vol. 54, no. 10, pp. 2102-2109, 2007.
- [60] D. Lan, "Development of 3-D Printed Hybrid Packaging for GaAs-MEMS Oscillators based on Piezoelectrically-Transduced ZnO-on-SOI Micromechanical Resonators" (2018). Graduate Theses and Dissertations.
- [61] J. Kuypers, C. Lin, G. Vigevani and A. Pisano, "Intrinsic temperature compensation of aluminum nitride Lamb wave resonators for multiple-frequency references," 2008 IEEE International Frequency Control Symposium, pp. 240-249, Honolulu, HI, 2008.
- [62] A. K. Samarao and F. Ayazi, "Temperature Compensation of Silicon Resonators via Degenerate Doping," in *IEEE Transactions on Electron Devices*, vol. 59, no. 1, pp. 87-93, 2012.
- [63] R. Goto, H. Nakamura and K. Hashimoto, "Spurious free TC-SAW duplexer using the SiO₂/LiNbO₃ structure," 2019 IEEE International Ultrasonics Symposium (IUS), pp. 2075-2078, Glasgow, United Kingdom, 2019.

- [64] Q. Zou et al., “Temperature-compensated FBAR duplexer for Band 13,” IEEE International Ultrasonics Symposium (IUS), pp. 236-238, 2013.
- [65] C. Lin et al., “Thermally compensated aluminum nitride Lamb wave resonators for high temperature applications,” Appl. Phys. Lett. 97, 2010.
- [66] Y. Wang et al., “A zero TCF Band 13 SAW duplexer,” 2015 IEEE International Ultrasonics Symposium (IUS), pp. 1-4, Taipei, 2015.
- [67] H. Kobayashi, K. Tohyama, Y. Hori, Y. Iwasaki and K. Suzuki, “A study on temperature-compensated hybrid substrates for surface acoustic wave filters,” 2010 IEEE International Ultrasonics Symposium, pp. 637-640, San Diego, CA, 2010.
- [68] Y. Hori, H. Kobayashi, K. Tohyama, Y. Iwasaki and K. Suzuki, “A hybrid substrate for a temperature-compensated surface acoustic wave filter,” 2009 IEEE International Ultrasonics Symposium, pp. 2631-2634, Rome, 2009.
- [69] M. Miura et al., “Temperature compensated LiTaO₃/sapphire bonded SAW substrate with low loss and high coupling factor suitable for US-PCS application,” 2004 IEEE Ultrasonics Symposium, vol. 2, pp. 1322-1325, Montreal, Quebec, Canada, 2004.
- [70] Q. Li, S. Fu, C. Song et al. “Improved resistance to electromigration and acoustomigration of Al interdigital transducers by Ni underlayer,” Rare Met, vol. 37, pp. 823–830, 2018.
- [71] W. Ruile, G. Raml, A. Springer and R. Weigel, “A novel test device to characterize SAW acoustomigration,” 2000 IEEE Ultrasonics Symposium. Proceedings, vol. 1, pp. 275-278, San Juan, Puerto Rico, USA, 2000.
- [72] B. Ivira, R.-Y. Fillit, F. Ndagijimana, P. Benech, G. Parat, and P. Ancy, “Self-heating study of bulk acoustic wave resonators under high RF power,” IEEE Transactions on Ultrasonics, Ferroelectrics and Frequency Control, vol. 55, no. 1, pp. 139–147, 2008.
- [73] H. Schmidt, R. Kunze, M. Weihnacht and S. Menzel, “Investigation of acoustomigration effects in Al-based metallizations,” 2002 IEEE Ultrasonics Symposium, vol.1, pp. 415-418, Munich, Germany, 2002.
- [74] R. Abdolvand, B. Bahreyni, J. Lee, and F. Nabki, “Micromachined Resonators: A Review,” Micromachines, vol. 7, no. 9, p. 160, Aug. 2016.
- [75] F. Ejeckam, D. Francis, F. Faili, F. Lowe, J. Wilman, T. Mollart, J. Dodson, D. Twitchen and B. Bolliger, Element Six Technologies and D. Babic, “GaN-on-Diamond: The Next GaN,” Microwave Journal, May. 2014.

[76] X. Han, D. Lan and J. Wang, "ZnO-on-diamond resonators with notched thin-film piezoelectric interdigital transducer for enhanced signal-to-noise ratio and feedthrough suppression," 33rd IEEE International Conference on Micro Electro Mechanical Systems (MEMS), pp. 1289-1291, Vancouver, BC, Canada, 2020.


[77] G. Piazza et al. "One and two port piezoelectric higher order contour-mode MEMS resonators for mechanical signal processing," Solid-State Electronics, vol. 51, iss. 11-12, pp. 1596-1608, 2007.

[78] G. Piazza and A. Pisano, "Two-port stacked piezoelectric aluminum nitride contour-mode resonant MEMS," Sensors and Actuators A: Physical, vol. 136, iss. 2, pp. 638-645, 2007.

Appendices


Appendix A: Copyright Permissions

The permission below is for the use of Figure 1.1



EMERGING SOURCES CITATION INDEX
THOMSON REUTERS

Scopus®



OPEN ACCESS

0.6 2019 CiteScore
27th percentile

Powered by Scopus

Journal of Applied Science and Engineering

Q3 Engineering (miscellaneous) best quartile

SJR 2019 0.16
powered by scimagojr.com

Search keywords

Research Categories

Computer Science and Information Engineering

Open Access License Agreement

The Journal of Applied Science and Engineering uses an Immediate Open Access model (Gold Open Access). All articles published at the Journal of Applied Science and Engineering are Open Access. The publication is funded by a fee paid at the time of acceptance (Article Processing Charge). All manuscripts accepted and published after July 14, 2020 on this site use the Creative Commons Attribution 4.0 License (CC BY 4.0). Author(s) retain the copyright of their work, with articles licensed to the publisher (Tamkang University Press) and Journal of Applied Science and Engineering. You do not need to seek permission from the Journal of Applied Science and Engineering for reuse of contents published on this site.

This means;

1. All articles are immediately available free-of-charge upon publication.
2. Copyright on all Open Access articles accepted after July 14, 2020, in the Journal of Applied Science and Engineering is retained by the author(s), or the author's employer.
3. Author(s) grant Tamkang University Press a license to publish the article and identify itself as the original publisher.
4. Author(s) also grant any third party the right to use the article freely as long as its integrity is maintained and the original authors, citation details, and publisher are identified.

You are free to:

Share — copy and redistribute the material in any medium or format

Adapt — remix, transform, and build upon the material for any purpose, even commercially.



Under the following terms:


Attribution — You must give appropriate credit, provide a link to the license, and indicate if changes were made. You may do so in any reasonable manner, but not in any way that suggests the licensor endorses you or your use.

No additional restrictions — You may not apply legal terms or technological measures that legally restrict others from doing anything the license permits.

Where an author is prevented from being the copyright holder (US government employees, UK, Canadian, Australian Government employee, or Crown Copyright), minor variations may be required. In such cases, the copyright line and license statement in individual PDF articles will be adjusted. Authors requiring a variation of this type should inform the Editorial team immediately after submission of their article. Changes to the copyright line cannot be made after publication of an article.

The permission below is for the use of Figure 1.2

Home Help Email Support Sign in Create Account



1.51-GHz nanocrystalline diamond micromechanical disk resonator with material-mismatched isolating support

Conference Proceedings: 17th IEEE International Conference on Micro Electro Mechanical Systems, Maastricht MEMS 2004 Technical Digest

Author: Jing Wang

Publisher: IEEE

Date: 2004

Copyright © 2004, IEEE

Thesis / Dissertation Reuse

The IEEE does not require individuals working on a thesis to obtain a formal reuse license, however, you may print out this statement to be used as a permission grant:

Requirements to be followed when using any portion (e.g., figure, graph, table, or textual material) of an IEEE copyrighted paper in a thesis:

- 1) In the case of textual material (e.g., using short quotes or referring to the work within these papers) users must give full credit to the original source (author, paper, publication) followed by the IEEE copyright line © 2011 IEEE.
- 2) In the case of illustrations or tabular material, we require that the copyright line © [Year of original publication] IEEE appear prominently with each reprinted figure and/or table.
- 3) If a substantial portion of the original paper is to be used, and if you are not the senior author, also obtain the senior author's approval.



Requirements to be followed when using an entire IEEE copyrighted paper in a thesis:


- 1) The following IEEE copyright/ credit notice should be placed prominently in the references: © [year of original publication] IEEE. Reprinted, with permission, from [author names, paper title, IEEE publication title, and month/year of publication]
- 2) Only the accepted version of an IEEE copyrighted paper can be used when posting the paper or your thesis on-line.
- 3) In placing the thesis on the author's university website, please display the following message in a prominent place on the website: In reference to IEEE copyrighted material which is used with permission in this thesis, the IEEE does not endorse any of [university/educational entity's name goes here]'s products or services. Internal or personal use of this material is permitted. If interested in reprinting/republishing IEEE copyrighted material for advertising or promotional purposes or for creating new collective works for resale or redistribution, please go to http://www.ieee.org/publications_standards/publications/rights/rights_link.html to learn how to obtain a License from RightsLink.

If applicable, University Microfilms and/or ProQuest Library, or the Archives of Canada may supply single copies of the dissertation.

BACK

CLOSE WINDOW

Home Help Email Support Sign in Create Account



1.156-GHz self-aligned vibrating micromechanical disk resonator

Author: Jing Wang

Publication: IEEE Transactions on Ultrasonics, Ferroelectrics, and Frequency Control

Publisher: IEEE

Date: Dec. 2004

Copyright © 2004, IEEE

Thesis / Dissertation Reuse

The IEEE does not require individuals working on a thesis to obtain a formal reuse license, however, you may print out this statement to be used as a permission grant:

Requirements to be followed when using any portion (e.g., figure, graph, table, or textual material) of an IEEE copyrighted paper in a thesis:

- 1) In the case of textual material (e.g., using short quotes or referring to the work within these papers) users must give full credit to the original source (author, paper, publication) followed by the IEEE copyright line © 2011 IEEE.
- 2) In the case of illustrations or tabular material, we require that the copyright line © [Year of original publication] IEEE appear prominently with each reprinted figure and/or table.
- 3) If a substantial portion of the original paper is to be used, and if you are not the senior author, also obtain the senior author's approval.

Requirements to be followed when using an entire IEEE copyrighted paper in a thesis:

- 1) The following IEEE copyright/ credit notice should be placed prominently in the references: © [year of original publication] IEEE. Reprinted, with permission, from [author names, paper title, IEEE publication title, and month/year of publication]
- 2) Only the accepted version of an IEEE copyrighted paper can be used when posting the paper or your thesis on-line.
- 3) In placing the thesis on the author's university website, please display the following message in a prominent place on the website: In reference to IEEE copyrighted material which is used with permission in this thesis, the IEEE does not endorse any of [university/educational entity's name goes here]'s products or services. Internal or personal use of this material is permitted. If interested in reprinting/republishing IEEE copyrighted material for advertising or promotional purposes or for creating new collective works for resale or redistribution, please go to http://www.ieee.org/publications_standards/publications/rights/rights_link.html to learn how to obtain a License from RightsLink.

If applicable, University Microfilms and/or ProQuest Library, or the Archives of Canada may supply single copies of the dissertation.

The permission below is for the use of Figure 1.2



RightsLink®



I.H.P. SAW technology and its application to microacoustic components (Invited)

Conference Proceedings: 2017 IEEE International Ultrasonics Symposium (IUS)

Author: Tsutomu Takai

Publisher: IEEE

Date: Sept. 2017

Copyright © 2017, IEEE

Thesis / Dissertation Reuse

The IEEE does not require individuals working on a thesis to obtain a formal reuse license, however, you may print out this statement to be used as a permission grant:

Requirements to be followed when using any portion (e.g., figure, graph, table, or textual material) of an IEEE copyrighted paper in a thesis:

1) In the case of textual material (e.g., using short quotes or referring to the work within these papers) users must give full credit to the original source (author, paper, publication) followed by the IEEE copyright line © 2011 IEEE.

2) In the case of illustrations or tabular material, we require that the copyright line © [Year of original publication] IEEE appear prominently with each reprinted figure and/or table.

3) If a substantial portion of the original paper is to be used, and if you are not the senior author, also obtain the senior author's approval.

Requirements to be followed when using an entire IEEE copyrighted paper in a thesis:

1) The following IEEE copyright/ credit notice should be placed prominently in the references: © [Year of original publication] IEEE. Reprinted, with permission, from [author names, paper title, IEEE publication title, and month/year of publication]

2) Only the accepted version of an IEEE copyrighted paper can be used when posting the paper or your thesis on-line.

3) In placing the thesis on the author's university website, please display the following message in a prominent place on the website: In reference to IEEE copyrighted material which is used with permission in this thesis, the IEEE does not endorse any of [university/educational entity's name goes here]'s products or services. Internal or personal use of this material is permitted. If interested in reprinting/republishing IEEE copyrighted material for advertising or promotional purposes or for creating new collective works for resale or redistribution, please go to http://www.ieee.org/publications_standards/publications/rights/rights_link.html to learn how to obtain a License from RightsLink.

If applicable, University Microfilms and/or ProQuest Library, or the Archives of Canada may supply single copies of the dissertation.

BACK

CLOSE WINDOW

The permission below is for the use of Figure 4.1

Order Number: 1088883
Order Date: 07 Jan 2021

[Print order](#)

Payment Information

XU HAN
xhan@usf.edu
Payment method: Invoice

Billing Address:
XU HAN
University of South Florida
5100 Burchette Road
TAMPA, FL 33647
United States
+1 (408) 660-5140
xhan@usf.edu

Customer Location:
XU
University of South Florida
5100 Burchette Road
Unit 3201
TAMPA, FL 33647
United States

Order Details

1. Acoustic wave and electromechanical resonators : concept to key applications

Billing Status:
Open

[Print License](#)

Order license ID	1088883-1	Type of use	Republish in a thesis/dissert...
Order detail status	Completed	Publisher	Artech House
ISBN-13	9781607839774	Portion	Image/photo/illustration
			0.00 USD
			Republication Permission

[Hide Details](#)

LICENSED CONTENT

Publication Title	Acoustic wave and electrom...	Country	United States of America
Author/Editor	Campanella, Humberto.	Rightholder	Artech House Inc
Date	01/01/2010	Publication Type	Book
Language	English		

REQUEST DETAILS

Portion Type	Image/photo/illustration	Distribution	Worldwide
Number of images / photos / illustrations	1	Translation	Original language of publica...
Format (select all that apply)	Electronic	Copies for the disabled?	No
Who will republish the content?	Academic institution	Minor editing privileges?	No
Duration of Use	Life of current edition	Incidental promotional use?	No
Lifetime Unit Quantity	Up to 499	Currency	USD
Rights Requested	Main product		

NEW WORK DETAILS

Title	Piezoelectrically-Transduced...	Institution name	University of South Florida
Instructor name	Xu Han	Expected presentation date	2021-01-22

ADDITIONAL DETAILS

The requesting person / organization to appear on the license
Xu Han/ University of South ...

REUSE CONTENT DETAILS

Title, description or numeric reference of the portion(s)	Figure 2.7 Vibration modes ...	Title of the article/chapter the portion is from	Fundamentals of Piezoelectr...
Editor of portion(s)	NA	Author of portion(s)	Campanella, Humberto.
Volume of serial or monograph	NA	Publication date of portion	2010-01-01
Page or page range of portion	44		

Total Items: 1

Subtotal: 0.00 USD

The permission below is for the use of Figure 4.4



RightsLink®



High-Q UHF micromechanical radial-contour mode disk resonators

Author: J.R. Clark
Publication: Journal of Microelectromechanical Systems
Publisher: IEEE
Date: Dec. 2005

Copyright © 2005, IEEE

Thesis / Dissertation Reuse

The IEEE does not require individuals working on a thesis to obtain a formal reuse license, however, you may print out this statement to be used as a permission grant:

Requirements to be followed when using any portion (e.g., figure, graph, table, or textual material) of an IEEE copyrighted paper in a thesis:

- 1) In the case of textual material (e.g., using short quotes or referring to the work within these papers) users must give full credit to the original source (author, paper, publication) followed by the IEEE copyright line © 2011 IEEE.
- 2) In the case of illustrations or tabular material, we require that the copyright line © [Year of original publication] IEEE appear prominently with each reprinted figure and/or table.
- 3) If a substantial portion of the original paper is to be used, and if you are not the senior author, also obtain the senior author's approval.

Requirements to be followed when using an entire IEEE copyrighted paper in a thesis:

- 1) The following IEEE copyright/ credit notice should be placed prominently in the references: © [year of original publication] IEEE. Reprinted, with permission, from [author names, paper title, IEEE publication title, and month/year of publication]
- 2) Only the accepted version of an IEEE copyrighted paper can be used when posting the paper or your thesis on-line.
- 3) In placing the thesis on the author's university website, please display the following message in a prominent place on the website: In reference to IEEE copyrighted material which is used with permission in this thesis, the IEEE does not endorse any of [university/educational entity's name goes here]'s products or services. Internal or personal use of this material is permitted. If interested in reprinting/republishing IEEE copyrighted material for advertising or promotional purposes or for creating new collective works for resale or redistribution, please go to http://www.ieee.org/publications_standards/publications/rights/rights_link.html to learn how to obtain a License from RightsLink.

If applicable, University Microfilms and/or ProQuest Library, or the Archives of Canada may supply single copies of the dissertation.

The permission below is for the use of Figure 4.5



RightsLink®



Micromachined aluminum nitride acoustic resonators with an epitaxial silicon carbide layer utilizing high-order Lamb wave modes

Conference Proceedings: 2012 IEEE 25th International Conference on Micro Electro Mechanical Systems (MEMS)
Author: Chih-Ming Lin
Publisher: IEEE
Date: Jan. 2012

Copyright © 2012, IEEE

Thesis / Dissertation Reuse

The IEEE does not require individuals working on a thesis to obtain a formal reuse license, however, you may print out this statement to be used as a permission grant:

Requirements to be followed when using any portion (e.g., figure, graph, table, or textual material) of an IEEE copyrighted paper in a thesis:

- 1) In the case of textual material (e.g., using short quotes or referring to the work within these papers) users must give full credit to the original source (author, paper, publication) followed by the IEEE copyright line © 2011 IEEE.
- 2) In the case of illustrations or tabular material, we require that the copyright line © [Year of original publication] IEEE appear prominently with each reprinted figure and/or table.
- 3) If a substantial portion of the original paper is to be used, and if you are not the senior author, also obtain the senior author's approval.

Requirements to be followed when using an entire IEEE copyrighted paper in a thesis:

- 1) The following IEEE copyright/ credit notice should be placed prominently in the references: © [year of original publication] IEEE. Reprinted, with permission, from [author names, paper title, IEEE publication title, and month/year of publication]
- 2) Only the accepted version of an IEEE copyrighted paper can be used when posting the paper or your thesis on-line.
- 3) In placing the thesis on the author's university website, please display the following message in a prominent place on the website: In reference to IEEE copyrighted material which is used with permission in this thesis, the IEEE does not endorse any of [university/educational entity's name goes here]'s products or services. Internal or personal use of this material is permitted. If interested in reprinting/republishing IEEE copyrighted material for advertising or promotional purposes or for creating new collective works for resale or redistribution, please go to http://www.ieee.org/publications_standards/publications/rights/rights_link.html to learn how to obtain a License from RightsLink.

If applicable, University Microfilms and/or ProQuest Library, or the Archives of Canada may supply single copies of the dissertation.

Appendix B: Detailed Fabrication Process for Piezoelectric ZnO Resonators

Cleaning Samples

Label on the back of the wafer with Diamond Tipped Scribe
RCA clean
Solvent clean

1. Bottom Electrode (Mask Name: Bottom_Electrodes)

1.1. Lithography LOR10B + G-thinner and AZ1512 (~1.5um)

Equipment: Photoresist Spinner

- Spin diluted LOR 10B
 - Step 1: 10 sec @ 500 RPM, ACL= 500
 - Step 2: 40 sec @ 3500 RPM, ACL= 1500
- Soft-bake: 8 min 30 sec @ 170°C (LOR needs to be around 400 nm)

Equipment: Photoresist Spinner

- Spin AZ1512
 - Step 1: 12 sec @ 500 RPM, ACL=150
 - Step 2: 40 sec @ 2500 RPM, ACL=1550
- Soft-bake 50 sec @ 95°C

Equipment: EVG620 Mask Aligner

Expose 3.3 sec @ 9.7 mW/cm² with hard contact

Post-bake 50 sec @ 105°C

Develop 25 sec in AZ726

DI water rinse and N₂ dry

Step-height check using profilometer (it should be around 1.2 μm)

1.2. Descum

Equipment: Tegal O2 Plasma Asher

O₂: 60 sccm

RF Power: 2/5 of the max power

Time: 2 min

1.3. Chrome Deposition

Equipment: AJA Sputtering

Power: 100 watts RF

Pressure: 5 mTorr

Flow rate: Ar 12 sccm

Time: 14 min (~40 nm)

1.4. Platinum Deposition

Equipment: AJA Sputtering

Power: 100 W DC

Pressure: 5 mTorr
Flow rate: Ar 12 sccm
Time: 20 min (~200 nm)

1.5. Lift-off

Submerge wafer in Microposit 1165 for ~15 min @ ~65 °C
Rinse wafer with water
Solvent clean and N₂ dry
Descum (1.2)

2. ZnO Deposition

Equipment: AJA Sputtering
Power: 85 W RF (dual-gun system)
O₂: Ar 6:6 sccm
Pressure: 5 mTorr
Temperature: 300°C
Time: 2.5 hr (~500 nm)

2.1 RTP Annealing

Annealing: 600°C for 30 min with (N₂)

3. Open Vias (Mask Name: Vias)

3.1. Lithography AZ1512

Equipment: Photoresist Spinner #1

- Spin AZ1512
 - Step 1: 12 sec @ 300 RPM, ACL=110
 - Step 2: 40 sec @ 2500 RPM, ACL=1650

Soft-bake 50 sec @ 95°C

Equipment: EVG620 Mask Aligner
Expose 7 sec @ 9.7 mW/cm² with hard contact

Post-bake 50 sec @ 105°C
Develop 25 sec in AZ726
DI water rinse and N₂ dry

3.2. ZnO Wet Etch

Solution: 1: 100 = HCl: H₂O (5 mL HCl, 500 mL H₂O)
Submerge wafer in solution (etch rate: 500 nm-600 nm/min, i.e 500 nm ZnO, start with 50 sec and etch every 3 sec more to achieve 1 um-1.5 um undercut)
Rinse wafer with water
Solvent clean and N₂ dry

4. Top Electrode (Mask Name: Top_Electrodes)

4.1. Lithography LOR10B + G-thinner and AZ1512

Equipment: Photoresist Spinner #1

- Spin diluted LOR 10B
 - Step 1: 10 sec @ 500 RPM, ACL= 500
 - Step 2: 40 sec @ 3500 RPM, ACL= 1500

Softbake: 8 min 30 sec @ 180°C

Equipment: Photoresist Spinner #1

- Spin AZ1512
 - Step 1: 12 sec @ 500 RPM, ACL=150
 - Step 2: 40 sec @ 2500 RPM, ACL=1550

Softbake 50 sec @ 95°C

Equipment: EVG620 Mask Aligner

Expose 3.3 sec @ 9.7 mW/cm² with hard contact

Postbake 50 sec @ 105 °C

Develop 25 sec in AZ726

DI water rinse and N₂ dry

Descum (1.2)

Step-height check using profilometer (it should be around 1.2 μm)

4.2. Descum

Equipment: Tegal O2 Plasma Asher

O₂: 60 sccm

RF Power: 2/5 of the max power

Time: 2 min

4.3. Chromium Deposition

Equipment: AJA Sputtering

Power: 100 W RF

Pressure: 5 mTorr

Flow rate: Ar 6 sccm

Time: 16 min (~30 nm)

4.4. Ruthenium Deposition

Equipment: AJA Sputtering

Power: 100 W DC

Pressure: 5 mTorr

Flow rate: Ar 6 sccm

Time: 25 min (~200 nm)

4.5. Lift-off

Submerge wafer in Microposit 1165 for ~15 min @ ~65 °C
Rinse wafer with water
Solvent clean and N₂ dry
Descum (1.2)

5. Pattern Resonator Body (Mask Name: Resonator_Body)

5.1(optional for diamond device) PECVD SiO₂ (2 um)

5.2. Lithography HMDS and AZ12XT (~10 um)

Equipment: Photoresist Spinner #1

- Spin HMDS
 - Step 1: 40 sec @ 3500 RPM, ACL=1650
- Spin AZ12XT
 - Step 1: 10 sec @ 300 RPM, ACL=1650
 - Step 2: 30 sec @ 3000 RPM, ACL=880
 - Step 1: 2 sec @ 6500 RPM, ACL=8500
 - Step 2: 10 sec @ 2000 RPM, ACL=880

Soft-bake: 2 min @ 110°C

Equipment: EVG620 Mask Aligner

Expose 13 sec @ 9.7 mW/cm² with hard contact

Post-bake 60 sec @ 90 °C

Develop 75 sec in AZ300

DI water rinse and N₂ dry

Descum (1.2)

Step-height check using profilometer (should be around 7.5-9.5 μm)

5.3. SiO₂ DRIE (optional for diamond device)

Equipment: Adixen AMS-100 Deep Reactive Ion Etcher

C₄F₈: 17 sccm

He: 150 sccm

CH₄: 13 sccm

Power: RF Source 1800 W / SH Biasing 400 W

Substrate temperature: -20 °C

Regulation mode: "position 100%"

SH position from the source: 140 mm

Helium pressure: 13 mbar

Etch rate: ~400 nm/min

Time: 8-10 min for etching 2 um PECVD SiO₂ completely (run 4-min process, and repeat)

5.4. ZnO DRIE

Equipment: Adixen AMS-100 Deep Reactive Ion Etcher
Ar: 16 sccm
CH₄: 30 sccm
He: 8 sccm
Power: RF Source 1800 W / SH Biasing 200 W
Substrate temperature: +20 °C
Regulation mode: pressure
Base pressure: 1.3E-2 mBar (may change to position mode)
SH position from the source: 140 mm
Helium pressure: 10 mbar
Etch rate: ~100-120 nm/min
Time: 6 min for etching 500 nm of ZnO completely

5.5. Diamond DRIE (optional for diamond device)

Equipment: Adixen AMS-100 Deep Relative Ion Etcher
O₂: 50 sccm
Power: RF Source 2800 W / SH Biasing 200 W
Substrate temperature: +20 °C
Regulation mode: pressure
Base pressure: 1.2E-2 mBar
SH position from the source: 140 mm
Helium pressure: 10 mbar
Etch rate: ~330 nm/min
Time: 30-40 min for etching 10um of diamond completely (run 10-min process, and repeat)

6. Dry Release

6.1. SF₆ Dry Etch

Equipment: Adixen AMS-100 Deep Reactive Ion Etcher
SF₆: 300 sccm,
Power: RF Source 2000 W / SH Biasing 0 W
Pulsed power: 10 ms @ 5 W; 90 ms @ 0 W
Substrate temperature: +20 °C
Regulation mode: pressure
Base pressure: 0.1 mBar
SH position from the source: 160 mm
Helium pressure: 10 mbar
Etch rate: ~4-5 um/min (varies with opening size)

7. Residual SiO₂ Removal (optional for diamond device)

Equipment: Adixen AMS-100 Deep Reactive Ion Etcher
C₄F₈: 17 sccm
He: 150 sccm
CH₄: 13 sccm
Power: RF Source 1800 W / SH Biasing 100 W

Substrate temperature: -20 °C
Regulation mode: "position 100%"
SH position from the source: 140 mm
Helium pressure: 13 mbar
Etch rate: ~300 nm/min
Time: 6-8 min (depends on how long the previous processes run)

8. Residual Photoresist Removal (for silicon device)

DO NOT USE SOLUTION OR ANY WET CHEMICAL!!!

Use DRIE O₂ cleaning recipe with minimum biasing power

Or use Equipment: Tegal O2 Plasma Asher

O₂: 60 sccm

RF Power: 4/5 of the max power

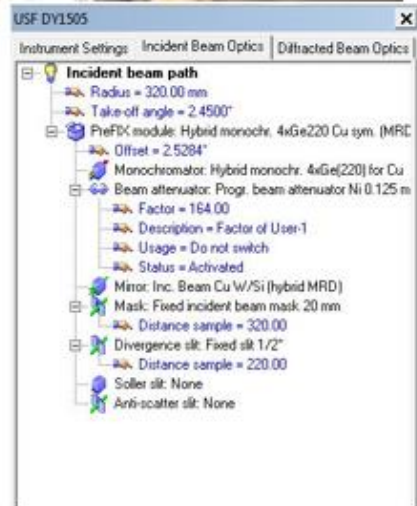
Time: 30 min (can be enough longer)

Appendix C: XRD Omega-axis Rocking Curve Measurement Instructions

Incident Optics Setup



- **Hybrid monochr. 4xGe220 Cu sym**
(make sure the cable is properly connected)
- **Beam attenuator (IMPORTANT!!)**
Usage = **Do not switch**
Status = **Activated**
- **Mask** = Please see user manual for proper size (No mask needed for wafers with diameter over 30mm)
- **Divergence slit: Fixed slit 1/2"**
- **Click "apply" or "ok", then you must open the door and remove the hybrid optic to ensure the attenuation is engaged**



1. Diffraction Optics Setup

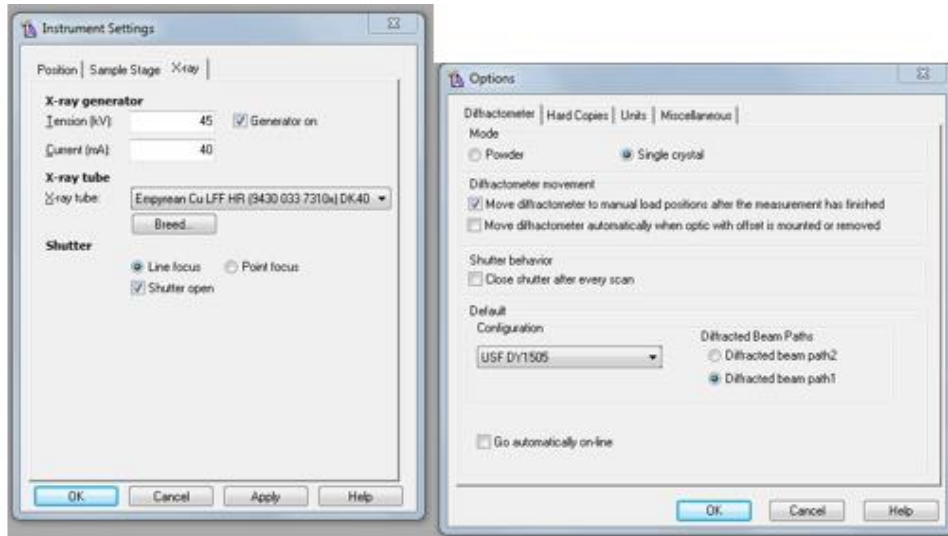


- PREFIX module: **Triple axis (Rocking curve optics double)**
- Receiving Slit: **Fixed slit 1/2"**
- Detector: **Xe [1]**
- Beam attenuator: **None**
- Mask: **None**
- Wavelength: **K-Alpha1=8.05keV**

USF DY1505

Instrument Settings | Incident Beam Optics | Diffracted Beam Optics

- [-] Diffracted beam path2
- [+] Diffracted beam path1
 - [-] Optic number = 1
 - Radius = 320.00 mm
 - Actual radius = 320.00 mm
 - Offset = 0.0000"
 - [-] Wavelength
 - Used wavelength = K-Alpha1 (1.5405980 Å)
 - = 8.05 keV (@ 50% PHD)
 - [-] PREFIX module: Triple axis (Rocking curve optics double)
 - Offset = 6.0000"
 - Receiving slit: Fixed slit 1/2"
 - Beam attenuator: None
 - Mask: None
 - [-] Detector: Proportional detector Xe[1]
 - PHD lower level = 35.0% (5.63 keV)
 - PHD upper level = 80.0% (12.88 keV)
 - Minimum PHD value = 0.0% (0.00 keV)
 - Maximum PHD value = 100.0% (16.10 keV)



2. Mount your Sample properly and increase current to 40Ma with line focus.



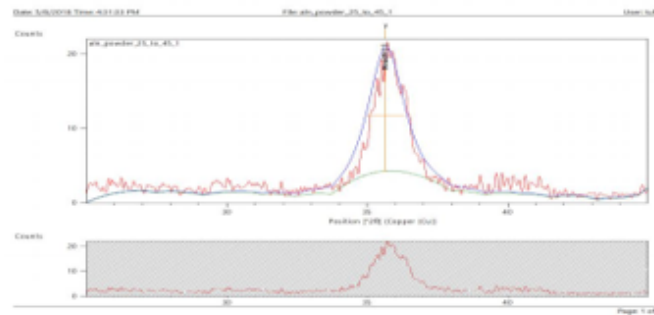
Note that the major flat is positioned parallel to the beam line. Ignore if your sample size is in random shape.

3. Direct Beam Alignment zero position Check

- Check and make sure all sample offset is clear as **0**
- Select the Instrument Settings tab, double click an item, select the Position tab, set 2Theta to **0** degrees, Offset to **0** degrees, Omega to **0** degrees, set Z to **9** mm, set chi and phi to **0** and press **OK**.
- Start with 2Theta manual scan, followed by Z scan and omega scan.
- After each scan is finished, right mouse click on the graph and select Peak Mode. To accept the location of the peak, press the Move To button and then select OK.
- Repeat Z scan and omega scan to make sure the angle reside consistently.
- Once the optimum values are found, click on the Tools menu and select Sample Offsets. Set the set position as new **0**.

4. Located 2Theta angle of the sample

- It is important to know the 2Theta angle you are interested to measure.
- Previously, I used different optic setup for the 2-theta scan of the ALN thin film and measured 35.6421° .
- You may look up the literature or perform the powder diffraction analysis to learn about the peak location.

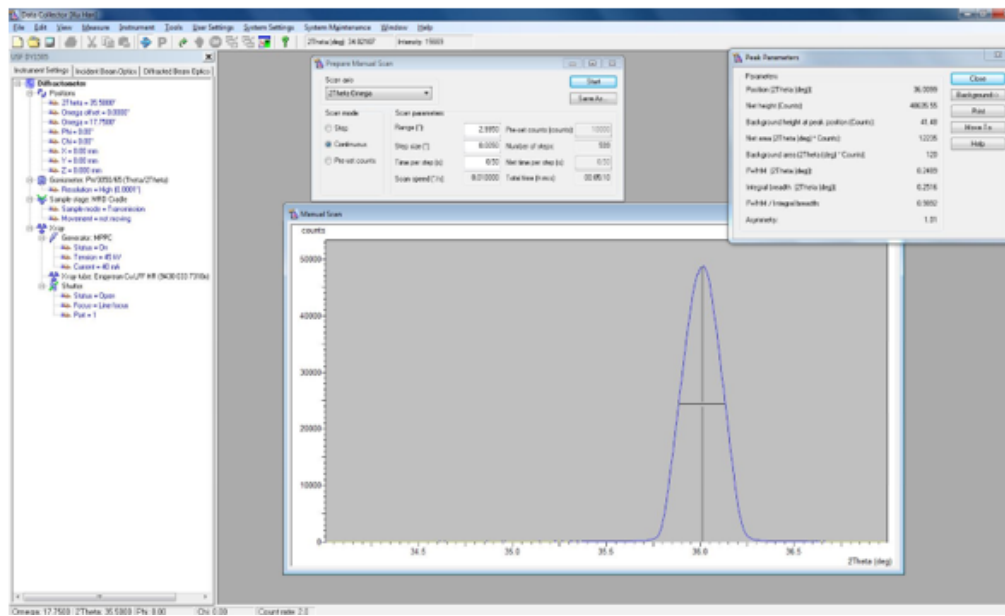


5. Adjusting the Setup for non-direct-beam measurement

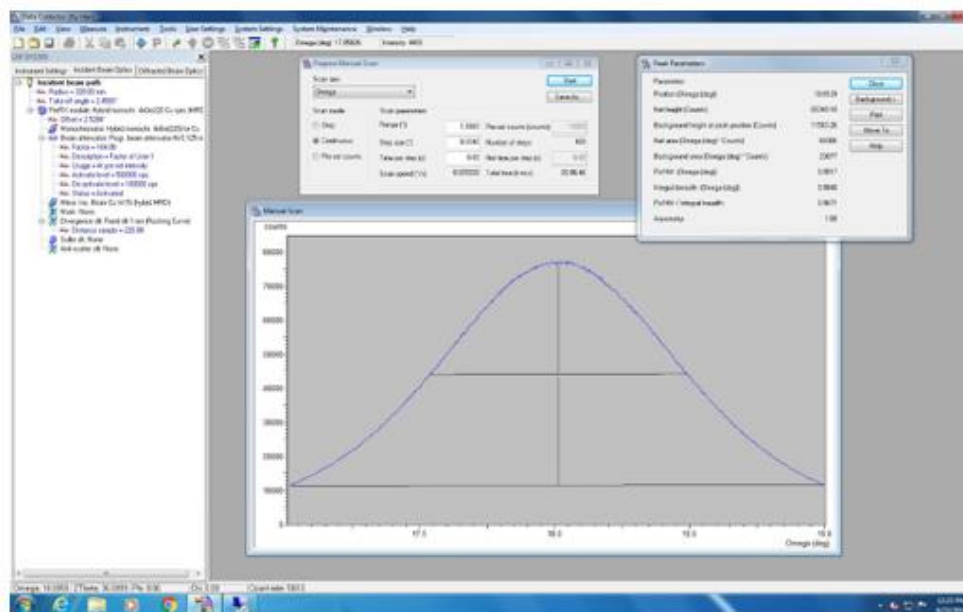
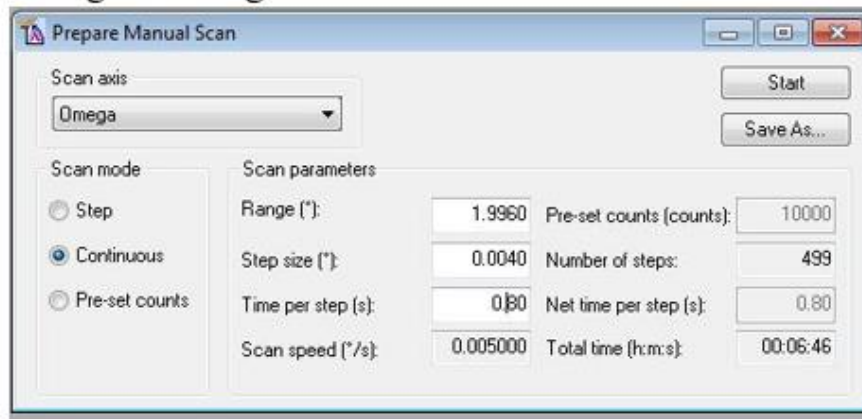
- Replace slits from $\frac{1}{2}$ " to **1 mm (Rocking curve)** for **both sides**.
- Keep incident beam attenuator “**activated**” and “**at pre-set intensity**”
- Activate level = 500000 cps
- De-activate level = 100000 cps

6. 2Theta-Omega scan

- This scan is for finding the 2theta angle more precisely by rotating 2theta with omega angle equaling half of the 2theta angle.
- If your 2theta moves from 34 -38, your omega moves from 17- 19 simultaneously.
- The scan range is set at **3-4 degree**, with step size **0.005**, and time per step **0.5 second**. (A rule of thumb is the total scan time should be around **5-6 minute**)



7. Omega fine alignment



8. Rocking Curve measurement

- Create a program scan as in step 8, you may need to increase the scan time for finer curve.
- A good scan can be as long as 10 minutes with range of 3 degree, step size = 0.004, time per step=0.8

About the Author

Xu Han received his BSEE degree from the University of South Florida in 2014, and prior to that, he was a registered FAA Airframe and Powerplant mechanic. In 2015, he started his Ph.D. program as an undergraduate and joined the RF MEMS Transducer Group at USF. Since 2017, he serves as the lab manager as well as teaching assistants for many RF and MEMS related courses, such as WAMI, MMIC, MEMS I and II. He was the Entrepreneur Lead of one of the groups representing USF participating I-Corps program funded by NSF in 2015. His research area is focusing on high-performance piezoelectric MEMS resonators design and fabrication based on diamond film implementation.

Xu served as one of the conference chairs for the 1st IEEE WAMI Forum in 2019. He was also received honorable mentions for the outstanding undergraduate and department TA award. In 2020 summer, Xu works as an RF filter design engineering Co-op for Skyworks Solutions, Inc. He is now a senior design engineer at Akoustis Technologies.